A projection scheme for an incompressible soft material poromechanics model

Mathieu Barré, Céline Grandmont, Philippe Moireau

A projection scheme for an incompressible soft material poromechanics model

Mathieu Barré[1,2], Céline Grandmont[3,4,5], Philippe Moireau[1,2]

[1] Inria, 1 Rue Honoré d'Estienne d'Orves, 91120 Palaiseau, France
[2] LMS, École Polytechnique, CNRS, Institut Polytechnique de Paris, Route de Saclay, 91120 Palaiseau, France
[3] Inria, 2 Rue Simone Iff, 75012 Paris, France
[4] LJLL, Sorbonne Université, CNRS, 4 Place Jussieu, 75005 Paris, France
[5] Département de Mathématique, Université Libre de Bruxelles, CP 214, Boulevard du Triomphe, 1050 Bruxelles, Belgium

Abstract

In this work, we propose and analyse a new scheme to discretize the linearized version of a rather general poromechanics model adapted to biological tissues perfusion. This model, which is related to – albeit different from – Biot equations, involves unsteady solid and fluid momentum balance equations that are further coupled through an incompressibility constraint, a pore pressure and permeability terms. The key feature of the scheme is to decouple the solid, fluid and pressure unknowns at each time step by means of a projection method, composed of a prediction and a correction step. We perform a complete stability analysis of the scheme depending on the implicit or explicit treatment of friction and pressure in the prediction step. Several boundary conditions are considered, including conditions coupling the solid and fluid phases on the boundary that are imposed at the discrete level using a Robin-Robin method. In the case of Dirichlet boundary conditions, we also provide a fully discrete error estimate as long as a discrete inf-sup condition is satisfied. The scheme properties and robustness with respect to physical parameters are illustrated by numerical experiments. Finally, its computational performance is compared with that of a monolithic approach.

Introduction

Poromechanics aims at describing the mechanical behavior of a deformable medium in which a solid phase and a fluid phase cohabit and are in interaction [Coussy, 2004]. Historically, the field of poromechanics was first developed for geosciences [Biot, 1941; Terzaghi, 1943]. More recently, it was established that porous effects also play a key role in the mechanical response of biological tissues, see the review [Khaled and Vafai, 2003] and references therein. Poromechanics models have hence been used to simulate transport phenomena in many human organs, including the heart [Yang and Taber, 1991; Huyghe et al., 1992; Nash and Hunter, 2000; Chapelle et al., 2010; Michler et al., 2013; Chabiniok et al., 2016; Di Gregorio et al., 2021; Barnafi Wittwer et al., 2022; Chabiniok et al., 2022], the lungs [Wall et al., 2010; Berger et al., 2016; Genet et al., 2020; Patte et al., 2022], the brain [Basser, 1992; Tully and Ventikos, 2011; Vardakis et al., 2016; Guo et al., 2018; Lee et al., 2019; Kedarasetti et al., 2022] or again the eye [Causin et al., 2014; Ruiz-Baier et al., 2022]. Such biomedical applications are associated with different physical regimes than in geosciences, requiring in particular to take into account solid quasi-incompressiblity, potentially strong inertial effects in both solid and fluid phases as well as viscous fluid effects and possible large solid deformations. This led the authors of [Chapelle and Moireau, 2014] to revisit porous media theory in this context, resulting in a rather

general non-linear poromechanics model adapted to soft tissues perfusion while respecting thermodynamics principles and energy balance.

In this paper, we consider its linearized version, which generalizes to some extent Darcy, Brinkman and Biot equations of poroelasticity. The existence of strong and weak solutions to this linearized model was proved in [Barré et al., 2023a] both for a compressible skeleton and in the incompressible limit. The numerical analysis of a monolithic implicit time scheme can be found in [Burtschell et al., 2019; Barnafi et al., 2021] in the compressible case and in [Barré et al., 2023b] in the incompressible case. Since the fluid and solid equations are strongly coupled through the interstitial pressure, this monolithic approach requires to solve a large linear system with a saddle-point structure at each time step. Despite their robustness, these monolithic schemes may have a prohibitive computational cost in the targeted applications. In order to improve the computational efficiency, the main goal of the present study is to propose and analyse a splitting scheme that enables to decouple the solid, fluid and pressure equations at each time step. Our approach is similar to Chorin-Temam projection method [Chorin, 1969; Temam, 1969] but takes into account the specific saddle-point structure of the problem, which involves a divergence constraint on the velocity of the mixture. Moreover, it includes the case of total stress boundary conditions which are physiologically relevant boundary conditions coupling the solid and fluid phases on the porous domain boundary.

Projection methods, also known as fractional-step methods, were originally introduced for the study of incompressible fluid problems. These methods are prediction-correction schemes, in which a tentative velocity is computed without taking into account the incompressibility constraint, and then corrected by projecting it on a divergence-free space. First proposed in [Chorin, 1969; Temam, 1969], these schemes were improved in [Goda, 1979] and [Van Kan, 1986], their convergence analysis was performed in [Heywood and Rannacher, 1990; Rannacher, 1992; Shen, 1995; Guermond, 1996; Guermond and Quartapelle, 1998; Badia and Codina, 2007] and general boundary conditions were considered in [Maria Denaro, 2003; Guermond et al., 2005], see the review [Guermond et al., 2006]. Projection schemes were also used in fluid-structure interaction problems [Fernández et al., 2007; Guidoboni et al., 2009; Astorino and Grandmont, 2010]. In order to obtain stable explicit schemes with respect to added-mass effects occuring in such problems, they were combined with Nitsche's method [Burman and Fernández, 2009], Robin coupling derived from Nitsche's method [Astorino et al., 2010] or again Robin-Robin coupling [Burman et al., 2022a]. Similarly, projection methods were used in fluid-porous structure interaction problems [Caiazzo et al., 2011; Bukač et al., 2015].

For Biot-type systems, the most popular splitting procedures are the undrained split and fixed-stress split algorithms [Zienkiewicz et al., 1988; Settari and Mourits, 1998], for which time convergence and space-time convergence were respectively established in [Mikelić and Wheeler, 2013] and [Girault et al., 2019]. These algorithms were applied to the quasi-static Biot equations, but also to the multiple-network poroelasticity equations [Hong et al., 2020]. For the fixed-stress split, variants and numerical optimizations were described in [Both et al., 2017; Storvik et al., 2019; Both et al., 2019a]. Following this approach, [Both et al., 2022] proposes an alternating minimization splitting scheme for the linearized poromechanics model considered in the present work, and the scheme is shown to be convergent by adapting the method from [Both et al., 2019b]. However, when the bulk modulus becomes large, this scheme requires a large number of iterations before convergence is reached. In addition, total stress boundary conditions are not considered.

Less attention has been paid to projection methods for unsteady Biot-type problems. For the unsteady Biot equations, [Zienkiewicz et al., 1993] developed a staggered time stepping algorithm that was further improved in [Huang et al., 2001] and [Li et al., 2003]. In [Markert et al., 2009], a fractional-step method is studied for the incompressible poroacoustic equations, which is similar to the poromechanics model considered here. In these studies, equal-order finite elements for the velocities and the pressure are employed, which results in a condition on the time step for the scheme to be stable. Lastly, let us mention that Chorin-Temam-like methods were also used to deal with mixture divergence constraints appearing in biofilms growth modeling, see [Clarelli et al., 2013] and [Polizzi et al., 2017].

Concerning the non-linear poromechanical model introduced in [Chapelle and Moireau, 2014], following [Astorino et al., 2010] a partitioned method adapted from fluid-structure interaction is proposed in [Burtschell et al., 2017]. A Newmark scheme is used for the solid part together with a projection scheme for the fluid part, the authors propose a splitting scheme in which the fluid viscous sub-step is treated explicitly and

that tackles the case of total stress boundary conditions. Yet, the fluid projection sub-step is still coupled implicitly with the solid sub-step through the interstitial pressure.

Here, our strategy first consists in computing tentative fluid and solid velocities that do not verify the incompressibility constraint of the mixture, but take into account the fluid viscous effects, the solid deformation and the friction between the two phases. Then, the pressure is obtained by solving a Poisson-like problem with an homogenized density coefficient and the end-of-step velocities are built from the tentative ones in order to satisfy the mixture divergence constraint. The proposed scheme is related to the one designed in [Markert et al., 2009], for which no stability analysis has been carried out to our knowledge. In this work, we provide a complete stability analysis of the scheme depending on the treatment of permeability and of the various boundary conditions under consideration, and show the convergence of the method provided that the discrete inf-sup condition is satisfied. Note that the present analysis may be extended to the quasi-incompressible case, the Poisson projection step being replaced by solving a heat-like step (see Remark 2.3).

This paper is organized as follows. First, Section 1 briefly recalls the model under study and presents the different types of boundary conditions. Then, Section 2 is devoted to the description of the method and its variants, and the stability analysis is performed with a particular attention made on the friction term. In Section 2.4, we show how to extend the projection scheme to Neumann and total stress boundary conditions while keeping its stability properties. Coming back to the simple case of Dirichlet boundary conditions, an error estimate is provided in Section 3. Finally, the theoretical findings are illustrated by numerical results in Section 4 and the efficiency of the resulting solver is compared with that of a monolithic approach.

1 Problem setting

Let Ω be a bounded domain of $\mathbb{R}^d$ with $d = 2, 3$. We consider the following model, which describes the mechanical behavior of a porous medium by its solid displacement u_s, fluid velocity v_f and interstitial pressure p:

$$\begin{cases} \rho_s(1-\phi)\,\partial_{tt}^2 u_s - \operatorname{div}\big(\sigma_s(u_s)\big) - \operatorname{div}\big(\sigma_s^{\mathrm{vis}}(\partial_t u_s)\big) \\ \qquad - \phi^2\, k_f^{-1}(v_f - \partial_t u_s) + (\alpha-\phi)\,\nabla p = \rho_s(1-\phi)\, f, & \text{in } \Omega\times(0,T), \quad (1a) \\ \rho_f\phi\,\partial_t v_f - \operatorname{div}\big(\phi\,\sigma_f(v_f)\big) \\ \qquad + \phi^2\, k_f^{-1}(v_f - \partial_t u_s) - \theta\, v_f + \phi\,\nabla p = \rho_f\phi\, f, & \text{in } \Omega\times(0,T), \quad (1b) \\ \dfrac{\alpha-\phi}{\kappa_s}\,\partial_t p + \operatorname{div}\big((\alpha-\phi)\,\partial_t u_s + \phi\, v_f\big) = \dfrac{\theta}{\rho_f}, & \text{in } \Omega\times(0,T), \quad (1c) \end{cases}$$

This model, first introduced in [Burtschell et al., 2019] as the linearization of the non-linear poromechanics model from [Chapelle and Moireau, 2014] and further studied in [Barnafi et al., 2021; Both et al., 2022; Barré et al., 2023a,b], is composed of a solid momentum balance equation (1a), a fluid momentum balance equation (1b) and a mass conservation equation (1c). The fluid is assumed to be incompressible so that its density ρ_f is constant. The porosity, denoted by ϕ and possibly depending on space, corresponds to the proportion of fluid phase at each point of the domain, so that $1-\phi$ corresponds to the proportion of solid phase. This parameter is assumed to be given, and to satisfy

$$0 < \phi_{\min} \le \phi(x) \le \phi_{\max} < 1, \quad \forall x \in \Omega,$$

for some constants $\phi_{\min}$ and $\phi_{\max}$. The hydraulic conductivity tensor, defined as the ratio between the permeability tensor and the fluid viscosity, is denoted by k_f and quantifies the friction forces between the two phases. We assume that there exists $k_{\min}^{-1} > 0$ and $k_{\max}^{-1} > 0$ such that

$$k_{\min}^{-1}|v|^2 \le k_f^{-1} v\cdot v \le k_{\max}^{-1}|v|^2, \quad \forall v \in \mathbb{R}^d. \tag{2}$$

Problem (1) includes inertial effects for both phases, scaled by the solid density ρ_s and fluid density ρ_f. Moreover, for any $v \in \mathbb{R}^d$, it takes into account viscous effects by means of the viscous tensors

$$\sigma_s^{\text{vis}}(v) = 2\nu_s\,\varepsilon(v),$$

with the strain tensor $\varepsilon(v) = \frac{1}{2}(\nabla v + \nabla v^T)$, and

$$\sigma_f(v) = \lambda_f \text{div}\, v\, \mathbb{I} + 2\mu_f\,\varepsilon(v),$$

where $\nu_s \geq 0$ and $\mu_f > 0$ stands respectively for the solid and fluid viscosities. Similarly we assume that the structure stress tensor is given by

$$\sigma_s(v) = \lambda_s \text{div}\, v\, \mathbb{I} + 2\mu_s\,\varepsilon(v),$$

where $\lambda_s \geq 0$ and $\mu_s > 0$. The Biot-Willis coefficient and the solid bulk modulus are respectively denoted by α and κ_s. Finally, the porous medium is subject to a prescribed body force f and to an additional fluid mass input θ. As shown in [Barré et al., 2023a] using an appropriate change of variable, Problem (1) is closely related to Biot equations. Indeed, if the fluid viscous effects are neglected, namely if $\mu_f = 0$, it is equivalent to Biot poroacoustic equations derived in [Biot, 1956].

In the sequel, we focus on the case where the structure is non-viscous and incompressible, for which $\nu_s = 0$, $\alpha = 1$ and $\kappa_s = +\infty$. This case is the most difficult from the theoretical and numerical point of view since it combines an hyperbolic – parabolic coupling between the solid and fluid equations with an incompressibility constraint. It is also the most relevant in the perpective of biomedical applications since most of human tissues can be considered as quasi-incompressible and to be stable in the incompressible limit is crucial. Moreover, we assume here for the sake of simplicity that there is no fluid mass input in the porous medium, namely that $\theta = 0$ and we refer to our previous work [Barré et al., 2023b] for more details about the numerical treatment of the case $\theta \neq 0$. Written as a first-order evolution equation, the porous problem under study hence reads: find u_s, v_s, v_f and p such that

$$\begin{cases} \partial_t u_s - v_s = 0, & \text{(3a)} \\ \rho_s(1-\phi)\,\partial_t v_s - \text{div}\left(\sigma_s(u_s)\right) - \phi^2\, k_f^{-1}(v_f - v_s) + (1-\phi)\,\nabla p = \rho_s(1-\phi)\, f, & \text{(3b)} \\ \rho_f \phi\,\partial_t v_f - \text{div}\left(\phi\,\sigma_f(v_f)\right) + \phi^2\, k_f^{-1}(v_f - v_s) + \phi\,\nabla p = \rho_f \phi\, f, & \text{(3c)} \\ \text{div}\left((1-\phi)\, v_s + \phi\, v_f\right) = 0, & \text{(3d)} \end{cases}$$

where we have introduced the solid velocity unknown $v_s = \partial_t u_s$. A key feature of the incompressible poromechanics model (3) is that it satisfies an energy balance that writes, when considering homogeneous Dirichlet boundary conditions for both phases,

$$\begin{aligned} &\frac{1}{2}\frac{\text{d}}{\text{d}t}\int_\Omega \rho_s(1-\phi)\,|v_s|^2\,\text{d}x + \frac{1}{2}\frac{\text{d}}{\text{d}t}\int_\Omega \rho_f\phi|v_f|^2\,\text{d}x + \frac{1}{2}\frac{\text{d}}{\text{d}t}\int_\Omega \sigma_s(u_s) : \varepsilon(u_s)\,\text{d}x \\ &\qquad + \int_\Omega \phi\,\sigma_f(v_f) : \varepsilon(v_f)\,\text{d}x + \int_\Omega \phi^2 k_f^{-1}(v_f - v_s)^2\,\text{d}x = \int_\Omega \rho_s(1-\phi) f v_s\,\text{d}x + \int_\Omega \rho_f \phi f \cdot v_f\,\text{d}x, \end{aligned} \quad (4)$$

where we used the shortcut notation $k_f^{-1}(v_f - v_s)^2$ for $k_f^{-1}(v_f - v_s)\cdot(v_f - v_s)$. This energy identity will be an important tool for the stability analysis of the schemes proposed in the present study.

To be well-posed, Problem (3) has to be complemented with initial conditions for the solid displacement, solid velocity and fluid velocity, and with boundary conditions. Let us denote by Γ_D, Γ_N and Γ_T three subsets (possibly empty) of $\partial\Omega$, such that $\partial\Omega = \overline{\Gamma_D} \cup \overline{\Gamma_N} \cup \overline{\Gamma_T}$. In this work, we consider three types of boundary conditions. First, Dirichlet boundary conditions, either homogeneous, namely

$$\begin{aligned} u_s &= 0, \quad \text{on } \Gamma_D, \\ v_s &= 0, \quad \text{on } \Gamma_D, \\ v_f &= 0, \quad \text{on } \Gamma_D, \end{aligned} \quad (5)$$

or non-homogeneous, namely

$$\begin{aligned} u_s &= u_{s,bc}, \quad \text{on } \Gamma_D, \\ v_s &= v_{s,bc}, \quad \text{on } \Gamma_D, \\ v_f &= v_{f,bc}, \quad \text{on } \Gamma_D, \end{aligned} \tag{6}$$

where $u_{s,bc}$, $v_{s,bc}$ and $v_{f,bc}$ belong to $[\mathrm{L}^2(\Gamma_D)]^d$ and verify the compatibility condition

$$\int_{\Gamma_D} \big((1-\phi)v_{s,bc} + \phi\, v_{f,bc}\big) \cdot n \,\mathrm{d}S = 0. \tag{7}$$

Second, Neumann boundary conditions, for which an exterior traction force $b \in [\mathrm{L}^2(\Gamma_N)]^d$ acting on a part of the boundary is distributed between the solid and fluid stresses in the following way:

$$\begin{aligned} \sigma_s(u_s)n - (1-\phi)\, pn &= (1-\phi)\, b, \quad \text{on } \Gamma_N, \\ \phi\, \sigma_f(v_f)n - \phi\, pn &= \phi\, b, \quad \text{on } \Gamma_N, \end{aligned} \tag{8}$$

with n the exterior normal of $\partial\Omega$. Third, a total stress boundary condition, which is close to transmission boundary conditions encountered in fluid-structure interaction through the fluid-structure interface. In this case, the repartition of the boundary traction b between the fluid and solid stresses is not precised but the solid and fluid velocities are assumed to match at the interface, namely

$$\begin{aligned} v_f &= v_s, \quad \text{on } \Gamma_T, \\ \sigma^{\mathrm{tot}} n &= b, \quad \text{on } \Gamma_T, \end{aligned} \tag{9}$$

where

$$\sigma^{\mathrm{tot}} = \sigma_s(u_s) + \phi\, \sigma_f(v_f) - p\mathbb{I},$$

denotes the total stress tensor of the porous medium. This last kind of boundary conditions were considered for Problem (3) in [Burtschell et al., 2017] and [Burtschell et al., 2019], where it is discretized using a Nitsche's method inspired from [Astorino et al., 2010]. Similar boundary conditions have been largely studied in fluid-structure interaction problems, see for instance [Gerbeau and Vidrascu, 2003; Causin et al., 2005; Fernández et al., 2007; Guidoboni et al., 2009]. In fluid-structure interaction, they occur on the fluid-solid interface between a fluid domain Ω_f and a solid domain Ω_s. The major difference here is that the fluid and the solid phases cohabit in the same domain Ω, so that (9) is written on a part of the porous boundary and with the same exterior normal n for the fluid and the solid. Moreover, in fluid-structure interaction problems, the fluid incompressibility is known to cause an *added-mass effect* inducing possible numerical instabilities when treated in an explicit way [Causin et al., 2005]. A similar issue may happen for the considered porous model due to the incompressibility constraint on the mixture velocity (3d).

Problem (3) is a strongly coupled system in which the fluid and solid parts are coupled through the friction term, the interstitial pressure and the incompressibility constraint. Let $\Delta t = \frac{T}{n_T}$, $n_T \in \mathbb{N}^*$ be the time step, and let us denote by u^n the approximation of $u(t^n)$, where $t^n = n\Delta t$ and $n \in \{0, ..., n_T + 1\}$. Problem (3) can be discretized in time by the following monolithic scheme:

$$\begin{cases} \dfrac{u_s^{n+1} - u_s^n}{\Delta t} - v_s^{n+\frac{1}{2}} = 0, \\ \rho_s(1-\phi)\, \dfrac{v_s^{n+1} - v_s^n}{\Delta t} - \mathrm{div}\left(\sigma_s(u_s^{n+\frac{1}{2}})\right) \\ \qquad\qquad - \phi^2\, k_f^{-1}(v_f^{n+1} - v_s^{n+\frac{1}{2}}) + (1-\phi)\, \nabla p^{n+1} = \rho_s(1-\phi)\, f^{n+\frac{1}{2}}, \\ \rho_f \phi\, \dfrac{v_f^{n+1} - v_f^n}{\Delta t} - \mathrm{div}\left(\phi\, \sigma_f(v_f^{n+1})\right) \\ \qquad\qquad + \phi^2\, k_f^{-1}(v_f^{n+1} - v_s^{n+\frac{1}{2}}) - \theta\, v_f^{n+1} + \phi\, \nabla p^{n+1} = \rho_f \phi\, f^{n+\frac{1}{2}}, \\ \mathrm{div}\left((1-\phi)\, v_s^{n+\frac{1}{2}} + \phi\, v_f^{n+1}\right) = 0. \end{cases} \tag{10}$$

Provided that a Stokes-like discrete inf-sup condition for the mixture is satisfied, this scheme has been shown to circumvent pressure oscillations occuring in the incompressible limit and to be robust with respect to porosity and permeability [Barré et al., 2023b]. Yet, it is a strongly coupled scheme with a high computational cost that may be prohibitive in the targeted applications. Let us now present our splitting strategy to decouple the different equations of (3) and solve the fluid, solid and pressure separately at each time step.

2 Time discretization: decoupling strategies

In this section, homogeneous Dirichlet boundary conditions (5) are considered, namely $\Gamma_N = \emptyset$ and $\Gamma_T = \emptyset$. The cases of Neumann boundary conditions (8) and total stress boundary conditions (9) are treated at the next section.

2.1 The fully decoupled projection scheme

The proposed projection scheme is detailed in Scheme 1 below. The first step is a prediction step in which we compute solid and fluid tentative velocities $\widetilde{v}_s^{n+1}$ and $\widetilde{v}_f^{n+1}$ without taking into account the incompressibility constraint and the pressure gradient terms, but only the solid deformation, the fluid viscous effects and the friction between the two phases. Then, these velocities are corrected by reincorporating the pressure gradient term in (13a) and (13b). This is a *projection step*: to obtain the end-of-step velocities v_s^{n+1} and v_f^{n+1}, the tentative velocities $\widetilde{v}_s^{n+1}$ and $\widetilde{v}_f^{n+1}$ are projected on the mixture divergence-free space

$$H_\phi = \big\{(v_s, v_f) \in [\mathrm{L}^2(\Omega)]^d \times [\mathrm{L}^2(\Omega)]^d \,:\, \mathrm{div}\,\big((1-\phi)\,v_s + \phi\,v_f\big) = 0 \quad \text{in}\,\mathcal{D}'(\Omega) \\ \text{and}\ \big((1-\phi)\,v_s + \phi\,v_f\big)\cdot n = 0 \quad \text{on}\,\Gamma_D\big\},$$

which was studied in [Barré et al., 2023a, Proposition 3.4]. Lastly, the solid displacement u_s^{n+1} is computed directly in the structure prediction sub-step, and thus is not corrected corrected.

Scheme 1 Explicit treatment of permeability (non-incremental version)

Step 1: `(prediction step)`

– **Step 1.1**: `(structure prediction sub-step)`
Find u_s^{n+1} and $\widetilde{v}_s^{n+1}$ such that $u_s^{n+1}|_{\Gamma_D} = 0$, $\widetilde{v}_s^{n+1}|_{\Gamma_D} = 0$ and

$$\begin{cases} \rho_s(1-\phi)\dfrac{\widetilde{v}_s^{n+1} - v_s^n}{\Delta t} - \mathrm{div}\left(\sigma_s\Big(\dfrac{u_s^{n+1}+u_s^n}{2}\Big)\right) \\ \qquad\qquad - \phi^2 k_f^{-1}\Big(v_f^n - \dfrac{\widetilde{v}_s^{n+1}+v_s^n}{2}\Big) = \rho_s(1-\phi) f^{n+\frac{1}{2}}, & \text{(11a)} \\ \dfrac{u_s^{n+1}-u_s^n}{\Delta t} = \dfrac{\widetilde{v}_s^{n+1}+v_s^n}{2}. & \text{(11b)} \end{cases}$$

– **Step 1.2**: `(fluid prediction sub-step)`
Find $\widetilde{v}_f^{n+1}$ such that $\widetilde{v}_f^{n+1}|_{\Gamma_D} = 0$ and

$$\rho_f\phi\frac{\widetilde{v}_f^{n+1} - v_f^n}{\Delta t} - \mathrm{div}\left(\phi\,\sigma_f(\widetilde{v}_f^{n+1})\right) + \phi^2 k_f^{-1}\Big(\widetilde{v}_f^{n+1} - \frac{\widetilde{v}_s^{n+1}+v_s^n}{2}\Big) = \rho_f\phi\, f^{n+\frac{1}{2}}. \qquad (12)$$

Step 2: `(correction step)`
Find v_s^{n+1}, v_f^{n+1} and p^{n+1} such that $\int_\Omega p^{n+1}\,\mathrm{d}x = 0$ and

$$\begin{cases} \rho_s(1-\phi)\dfrac{v_s^{n+1}-\widetilde{v}_s^{n+1}}{\Delta t} + (1-\phi)\,\nabla p^{n+1} = 0, & \text{(13a)} \\ \rho_f\phi\dfrac{v_f^{n+1}-\widetilde{v}_f^{n+1}}{\Delta t} + \phi\,\nabla p^{n+1} = 0, & \text{(13b)} \\ \operatorname{div}\left((1-\phi)v_s^{n+1} + \phi\, v_f^{n+1}\right) = 0, & \text{(13c)} \\ \left((1-\phi)v_s^{n+1} + \phi\, v_f^{n+1}\right)\cdot n|_{\Gamma_D} = 0. & \text{(13d)} \end{cases}$$

Note that in the prediction step, we choose to start by advancing the structure before the fluid and thus compute the structure friction term from the fluid velocity at the previous time step and then use the predicted structure velocity in the friction term in the fluid prediction step. This is motivated by the fact that the friction term has a greater impact on the fluid than on the structure, which is more rigid. As a consequence, it is better to treat the friction term explicitly in the solid sub-step, see the term v_f^n appearing in (11a), which allows to treat it implicitly in the fluid sub-step (12). Note moreover that as in [Burtschell et al., 2019] and [Barré et al., 2023b], the solid part is discretized using a Newmark scheme while the fluid part is discretized with a backward Euler scheme.

From a numerical point of view, the main advantage of this scheme is that in the prediction step, the solid and fluid degrees of freedom are decoupled, which was not the case in the monolithic approach from [Barré et al., 2023b] that requires to solve a saddle-point problem at each time step. In the projection step, the solid, fluid and pressure degrees of freedom seem coupled at first sight, but this is only because system (13) corresponds to the Darcy-formulation of the projection step. In practice, it is more convenient to first solve the pressure with a Poisson-like equation, and then correct the velocities accordingly. As a matter of fact, under suitable regularity assumptions, dividing (13a) by ρ_s, (13b) by ρ_f, summing and taking the divergence, we have

$$\frac{1}{\Delta t}(\operatorname{div} v_m^{n+1} - \operatorname{div}\widetilde{v}_m^{n+1}) + \operatorname{div}\left(\left(\frac{1-\phi}{\rho_s} + \frac{\phi}{\rho_f}\right)\nabla p^{n+1}\right) = 0,$$

where $\widetilde{v}_m^{n+1}$ and v_m^{n+1} denote respectively the tentative and end-of-step mixture velocities, namely

$$\widetilde{v}_m^{n+1} = (1-\phi)\widetilde{v}_s^{n+1} + \phi\,\widetilde{v}_f^{n+1} \quad \text{and} \quad v_m^{n+1} = (1-\phi)v_s^{n+1} + \phi\, v_f^{n+1}.$$

From (13c), we know that $\operatorname{div} v_m^{n+1} = 0$. Thus, denoting $\rho_{\text{eff}} = \left(\frac{1-\phi}{\rho_s} + \frac{\phi}{\rho_f}\right)^{-1}$, we obtain

$$-\operatorname{div}\left(\rho_{\text{eff}}^{-1}\nabla p^{n+1}\right) = -(\Delta t)^{-1}\operatorname{div}\widetilde{v}_m^{n+1}.$$

Similarly, by dividing (13a) by ρ_s, (13b) by ρ_f, summing, taking the normal trace on Γ_D and using that $v_m^{n+1}\cdot n|_{\Gamma_D} = 0$ in virtue of (13d), we get $\rho_{\text{eff}}^{-1}\nabla p^{n+1}\cdot n|_{\Gamma_D} = 0$. Hence, the Poisson formulation of the correction step reads: find p^{n+1} such that

$$\begin{cases} -\operatorname{div}\left(\rho_{\text{eff}}^{-1}\nabla p^{n+1}\right) = -(\Delta t)^{-1}\operatorname{div}\widetilde{v}_m^{n+1}, & \text{in } \Omega, \\ \rho_{\text{eff}}^{-1}\nabla p^{n+1}\cdot n = 0, & \text{on } \Gamma_D. \end{cases} \tag{14}$$

After solving (14), the end-of-step velocities v_s^n and v_f^n can then be directly computed from (13a) and (13b), without having to couple the solid and fluid degrees of freedom. Note that in Chorin-Temam scheme for Stokes or Navier-Stokes equations, the Poisson correction step involves only Δp^{n+1}. Here, (14) involves a

space-dependent coefficient ρ_{eff}^{-1} which is closely related to the values taken by the porosity. More precisely, the effective density

$$\rho_{\text{eff}} = \left(\frac{1-\phi}{\rho_s} + \frac{\phi}{\rho_f} \right)^{-1}, \tag{15}$$

corresponds to the harmonic mean of the solid and fluid densities, weighted by the proportions of solid and fluid in the porous medium.

Essentially, Scheme 1 allows to fully decouple the solid, fluid and pressure degrees of freedom. Its main features are that the prediction steps consist in two unconstrained problems, the pressure step can be solved using an efficient Poisson solver, and the solid and fluid correction steps are numerically costless. Finally, let us check its consistency with respect to the initial problem. By summing the prediction and correction steps, we get

$$\begin{cases} \dfrac{u_s^{n+1}-u_s^n}{\Delta t} = \dfrac{\widetilde{v}_s^{n+1}+v_s^n}{2}, \\ \rho_s(1-\phi)\dfrac{v_s^{n+1}-v_s^n}{\Delta t} - \operatorname{div}\left(\sigma_s\Big(\dfrac{u_s^{n+1}+u_s^n}{2}\Big)\right) \\ \qquad -\phi^2 k_f^{-1}\Big(v_f^n - \dfrac{\widetilde{v}_s^{n+1}+v_s^n}{2}\Big) + (1-\phi)\nabla p^{n+1} = \rho_s(1-\phi) f^{n+\frac{1}{2}}, \\ \rho_f\phi\dfrac{v_f^{n+1}-v_f^n}{\Delta t} - \operatorname{div}\left(\phi\,\sigma_f(\widetilde{v}_f^{n+1})\right) + \phi^2 k_f^{-1}\Big(\widetilde{v}_f^{n+1} - \dfrac{\widetilde{v}_s^{n+1}+v_s^n}{2}\Big) + \phi\,\nabla p^{n+1} = \rho_f\phi\, f^{n+\frac{1}{2}}, \\ \operatorname{div}\left((1-\phi)v_s^{n+1} + \phi\, v_f^{n+1}\right) = 0, \end{cases} \tag{16}$$

which shows the consistency of the scheme with respect to Problem (3). Moreover, we see that (16) is very close to the backward Euler monolithic scheme analyzed in [Barré et al., 2023b]. In particular, the solid midpoint discretization allows to preserve the discrete mechanical energy, as it will be detailed in the stability analysis of the next subsection. The main difference is the explicit treatment of the fluid velocity in the permeability term, that comes from the decoupling of the solid and fluid prediction steps. However, when it comes to boundary conditions, the solid displacement and the tentative velocities satisfy exactly the Dirichlet boundary conditions (5), whereas *a priori* the end-of-step velocities only satisfy

$$\left((1-\phi)v_s^{n+1} + \phi\, v_f^{n+1}\right)\cdot n|_{\Gamma_D} = 0.$$

This is one of the standard drawbacks of the projection method when Dirichlet boundary conditions are imposed, which was also pointed in projection methods for fluid problems [Rannacher, 1992].

Remark 2.1. *For non-homogeneous boundary conditions (6), the only difference is that we have to impose* $u_s^{n+1}|_{\Gamma_D} = u_{s,bc}(t^{n+1})$, $\widetilde{v}_s^{n+1}|_{\Gamma_D} = v_{s,bc}(t^{n+1})$ *and* $\widetilde{v}_f^{n+1}|_{\Gamma_D} = v_{f,bc}(t^{n+1})$ *in the prediction step, with* $u_{s,bc}$, $v_{s,bc}$ *and* $v_{f,bc}$ *satisfying the compatibility condition (7). Moreover, the Poisson formulation of the correction step becomes: find* p^{n+1} *such that* $\int_\Omega p^{n+1}\,\mathrm{d}x = 0$ *and*

$$\begin{cases} -\operatorname{div}\left(\rho_{\text{eff}}^{-1}\nabla p^{n+1}\right) = -(\Delta t)^{-1}\operatorname{div}\widetilde{v}_m(t^{n+1}), & \text{in } \Omega, \\ \rho_{\text{eff}}^{-1}\nabla p^{n+1}\cdot n = (\Delta t)^{-1} v_{m,bc}^{n+1}\cdot n, & \text{on } \partial\Omega, \end{cases}$$

where $v_{m,bc}(t^{n+1}) = (1-\phi)\, v_{s,bc}(t^{n+1}) + \phi\, v_{f,bc}(t^{n+1})$.

Remark 2.2. *If we add solid viscosity in the model, namely if we consider Problem (1) with* $\nu_s > 0$, *the scheme can be modified by simply adding a term* $-\operatorname{div}\left(\sigma_s^{vis}\Big(\frac{\widetilde{v}_s^{n+1}+v_s^n}{2}\Big)\right)$ *in the solid prediction step (11a).*

Remark 2.3. *If we consider the compressible or nearly-incompressible case* $\kappa_s < +\infty$ *and* $\alpha < 1$, *the prediction step remains the same but one has to change the correction step as follows: find* v_s^{n+1}, v_f^{n+1} *and*

p^{n+1} *such that*

$$\begin{cases} \rho_s(1-\phi)\dfrac{v_s^{n+1}-\widetilde{v}_s^{n+1}}{\Delta t} + (\alpha-\phi)\,\nabla p^{n+1} = 0, \\ \rho_f\phi\dfrac{v_f^{n+1}-\widetilde{v}_f^{n+1}}{\Delta t} + \phi\,\nabla p^{n+1} = 0, \\ \dfrac{\alpha-\phi}{\kappa_s}\dfrac{p^{n+1}-p^n}{\Delta t} + \operatorname{div}\left((\alpha-\phi)v_s^{n+1} + \phi\, v_f^{n+1}\right) = 0. \end{cases}$$

From the Darcy-formulation above we can easily verify as before that p^{n+1} *solves*

$$(\Delta t)^{-1}\frac{\alpha-\phi}{\kappa_s}\frac{p^{n+1}-p^n}{\Delta t} - \operatorname{div}\left(\left(\frac{\alpha-\phi}{\rho_s}+\frac{\phi}{\rho_f}\right)\nabla p^{n+1}\right) = -(\Delta t)^{-1}\operatorname{div}\widetilde{v}_m^{n+1},$$

and that has to be complemented with the boundary conditions imposed on the pressure. This formulation is close to (14)*, but involves the pressure discrete derivative and an effective density* $\rho_{\text{eff}}^{\kappa_s} = \left(\frac{\alpha-\phi}{\rho_s}+\frac{\phi}{\rho_f}\right)^{-1}$ *that depends on the Biot coefficient* α*.*

Remark 2.4. *Note that in the structure prediction step* (11)*, we used a first-order formulation between the solid displacement and the tentative solid velocity. Such a weak formulation is convenient for the sake of the analysis. However, in practice, the solid displacement does not need to be computed as a primary unknown. Using* (11b)*, it can be eliminated from the prediction step by replacing* $u_s^{n+\frac{1}{2}}$ *by* $u_s^n + \frac{\Delta t}{2}\widetilde{v}_s^{n+\frac{1}{2}\sharp}$ *in* (11a)*, and then post-processed thanks to the relation* $u_s^{n+1} = u_s^n + \Delta t\,\widetilde{v}_s^{n+\frac{1}{2}\sharp}$*.*

For incompressible fluid problems, there exists two versions of projection schemes: the *non-incremental* one, which corresponds to the original scheme introduced by Chorin and Temam [Chorin, 1969; Temam, 1969], and the *incremental* one first proposed by [Goda, 1979], which is known to improve the convergence rate in time of the pressure. Assuming that the interstitial pressure is regular enough, we can propose such an incremental variant of Scheme 1. To do so, the key idea is to take into account the pressure gradients from the previous time step during the prediction step, and to modify the correction step accordingly. This improves the approximation of the tentative velocities by being as close as possible to (3b) and (3c), and hence the pressure approximation. The corresponding algorithm is presented in Scheme 2.

Scheme 2 Explicit treatment of permeability (incremental version)

Step 1: `(prediction step)`

– **Step 1.1**: `(structure prediction sub-step)`
Find u_s^{n+1} and $\widetilde{v}_s^{n+1}$ such that $u_s^{n+1}|_{\Gamma_D} = 0$, $\widetilde{v}_s^{n+1}|_{\Gamma_D} = 0$ and

$$\begin{cases} \rho_s(1-\phi)\dfrac{\widetilde{v}_s^{n+1}-v_s^n}{\Delta t} - \operatorname{div}\left(\sigma_s\left(\dfrac{u_s^{n+1}+u_s^n}{2}\right)\right) \\ \qquad -\phi^2 k_f^{-1}(v_f^n - \widetilde{v}_s^{n+1}) + (1-\phi)\nabla p^n = \rho_s(1-\phi)f^{n+\frac{1}{2}}, & \text{(17a)} \\ \dfrac{u_s^{n+1}-u_s^n}{\Delta t} = \widetilde{v}_s^{n+1}. & \text{(17b)} \end{cases}$$

– **Step 1.2**: `(fluid prediction sub-step)`
Find $\widetilde{v}_f^{n+1}$ such that $\widetilde{v}_f^{n+1}|_{\Gamma_D} = 0$ and

$$\begin{cases} \rho_f\phi\dfrac{\widetilde{v}_f^{n+1}-v_f^n}{\Delta t} - \operatorname{div}\left(\phi\,\sigma_f(\widetilde{v}_f^{n+1})\right) \\ \qquad +\phi^2 k_f^{-1}(\widetilde{v}_f^{n+1} - \widetilde{v}_s^{n+1}) + \phi\,\nabla p^n = \rho_f\phi\, f^{n+\frac{1}{2}}. \end{cases} \quad (18)$$

Step 2: `(correction step)`
Find v_s^{n+1}, v_f^{n+1} and p^{n+1} such that $\int_\Omega p^{n+1}\,\mathrm{d}x = 0$ and

$$\begin{cases} \rho_s(1-\phi)\dfrac{v_s^{n+1}-\widetilde{v}_s^{n+1}}{\Delta t} + (1-\phi)\,\nabla(p^{n+1}-p^n) = 0, & \text{(19a)}\\ \rho_f\phi\dfrac{v_f^{n+1}-\widetilde{v}_f^{n+1}}{\Delta t} + \phi\,\nabla(p^{n+1}-p^n) = 0, & \text{(19b)}\\ \mathrm{div}\,\big((1-\phi)v_s^{n+1}+\phi\,v_f^{n+1}\big) = 0, & \text{(19c)}\\ \big((1-\phi)v_s^{n+1}+\phi\,v_f^{n+1}\big)\cdot n|_{\Gamma_D} = 0. & \text{(19d)} \end{cases}$$

Here again, the correction step (19) can be reformulated as a Poisson problem, by simply replacing p^{n+1} by the pressure increment $p^{n+1}-p^n$ in (14). Note that for stability reasons that will be made clearer in the next subsection, the midpoint velocity $\frac{\widetilde{v}_s^{n+1}+v_s^n}{2}$ has been replaced by $\widetilde{v}_s^{n+1}$ in the prediction step.

Scheme 2 is very close to the one proposed in [Markert et al., 2009]. Indeed, the only differences are that in [Markert et al., 2009], the fluid viscous effects considered in (18) are neglected following a magnitude argument given in [Markert, 2007] and that the solid displacement is treated explicitly in (17a), leading to a CFL condition. However, strictly speaking, [Markert et al., 2009] does not include a theoretical stability analysis of the scheme, which we are now going to carry out.

2.2 Stability analysis

We start with the non-incremental version of the scheme. Let us introduce the notation

$$u_s^{n+\frac{1}{2}} = \frac{u_s^{n+1}+u_s^n}{2},$$

for the solid displacement midpoint velocity, and

$$\widetilde{v}_s^{n+\frac{1}{2}\sharp} = \frac{\widetilde{v}_s^{n+1}+v_s^n}{2}, \tag{20}$$

to denote the specific midpoint velocity appearing in the prediction steps. Moreover, we introduce the following subspace of $\mathrm{H}^1(\Omega)$

$$\mathrm{H}^1(\Omega)/\mathbb{R} = \left\{ p\in\mathrm{H}^1(\Omega)\,,\ \int_\Omega p\,\mathrm{d}x = 0 \right\}.$$

For the sake of simplicity we assume that no external body force is applied to the porous medium, namely $f=0$. Yet the stability analysis can be easily generalized. The weak formulation associated with Scheme 1 then reads

Step 1: `(prediction step)`

– **Step 1.1**: `(structure prediction sub-step)`
Find $u_s^{n+1}\in[\mathrm{H}_0^1(\Omega)]^d$ and $\widetilde{v}_s^{n+1}\in[\mathrm{H}_0^1(\Omega)]^d$ such that, for any $w_s\in[\mathrm{H}_0^1(\Omega)]^d$ and $d_s\in[\mathrm{H}_0^1(\Omega)]^d$,

$$\begin{aligned}\int_\Omega \rho_s(1-\phi)\frac{\widetilde{v}_s^{n+1}-v_s^n}{\Delta t}\cdot w_s\,\mathrm{d}x + \int_\Omega \sigma_s\Big(\frac{u_s^{n+1}-u_s^n}{\Delta t}\Big):\varepsilon(d_s)\,\mathrm{d}x \\ - \int_\Omega \sigma_s(\widetilde{v}_s^{n+\frac{1}{2}\sharp}):\varepsilon(d_s)\,\mathrm{d}x + \int_\Omega \sigma_s(u_s^{n+\frac{1}{2}}):\varepsilon(w_s)\,\mathrm{d}x \\ - \int_\Omega \phi^2 k_f^{-1}(v_f^n-\widetilde{v}_s^{n+\frac{1}{2}\sharp})\cdot w_s\,\mathrm{d}x = 0. \end{aligned} \tag{21}$$

– **Step 1.2**: `(fluid prediction sub-step)`
Find $\widetilde{v}_f^{n+1} \in [\mathrm{H}_0^1(\Omega)]^d$ such that, for any $w_f \in [\mathrm{H}_0^1(\Omega)]^d$,

$$\int_\Omega \rho_f \phi \frac{\widetilde{v}_f^{n+1} - v_f^n}{\Delta t} \cdot w_f \,\mathrm{d}x + \int_\Omega \phi\, \sigma_f(\widetilde{v}_f^{n+1}) : \varepsilon(w_f)\,\mathrm{d}x + \int_\Omega \phi^2 k_f^{-1}(\widetilde{v}_f^{n+1} - \widetilde{v}_s^{n+\frac{1}{2}\sharp}) \cdot w_f \,\mathrm{d}x = 0. \quad (22)$$

Step 2: `(correction step)`
Find $v_s^{n+1} \in [\mathrm{L}^2(\Omega)]^d$, $v_f^{n+1} \in [\mathrm{L}^2(\Omega)]^d$ and $p^{n+1} \in \mathrm{H}^1(\Omega)/\mathbb{R}$ such that, for any $w_s \in [\mathrm{L}^2(\Omega)]^d$, $w_f \in [\mathrm{L}^2(\Omega)]^d$ and $q \in \mathrm{H}^1(\Omega)/\mathbb{R}$,

$$\int_\Omega \rho_s(1-\phi)\frac{v_s^{n+1} - \widetilde{v}_s^{n+1}}{\Delta t} \cdot w_s \,\mathrm{d}x + \int_\Omega \rho_f \phi \frac{v_f^{n+1} - \widetilde{v}_f^{n+1}}{\Delta t} \cdot w_f \,\mathrm{d}x + \int_\Omega (1-\phi)\nabla p^{n+1} \cdot w_s \,\mathrm{d}x + \int_\Omega \phi\, \nabla p^{n+1} \cdot w_f \,\mathrm{d}x - \int_\Omega (1-\phi) v_s^{n+1} \cdot \nabla q \,\mathrm{d}x - \int_\Omega \phi\, v_f^{n+1} \cdot \nabla q \,\mathrm{d}x = 0. \quad (23)$$

Remark 2.5. *An alternative way of formulating weakly the correction step is to use a mixed formulation in the space H_ϕ.*

Remark 2.6. *Note that in (21), the weak formulation associated to (11b) used the scalar product $\int_\Omega \sigma_s(\cdot) : \varepsilon(\cdot)\,\mathrm{d}x$, which is a scalar product in $H_0^1(\Omega)$.*

The stability analysis is based on a discrete energy balance for each step of the algorithm. Let us define the discrete kinetic and mechanical energies by

$$\mathcal{E}_c^n = \frac{1}{2}\int_\Omega \rho_s(1-\phi)\,|v_s^n|^2 \,\mathrm{d}x + \frac{1}{2}\int_\Omega \rho_f \phi\,\left|v_f^n\right|^2 \mathrm{d}x \quad \text{and} \quad \mathcal{E}_m^n = \frac{1}{2}\int_\Omega \sigma_s(u_s^n) : \varepsilon(u_s^n)\,\mathrm{d}x.$$

Moreover, we introduce the kinetic energy associated with the prediction velocities, namely

$$\widetilde{\mathcal{E}}_c^{n+1} = \frac{1}{2}\int_\Omega \rho_s(1-\phi)\,\left|\widetilde{v}_s^{n+1}\right|^2 \mathrm{d}x + \frac{1}{2}\int_\Omega \rho_f \phi\,\left|\widetilde{v}_f^{n+1}\right|^2 \mathrm{d}x.$$

In what follows, we will use the algebraic identity

$$\big(a^{n+1} - a^n\big)a^{n+1} = \frac{1}{2}\big(a^{n+1}\big)^2 - \frac{1}{2}\big(a^n\big)^2 + \frac{\big(a^{n+1} - a^n\big)^2}{2}. \quad (24)$$

For the prediction step, we choose $w_s = \Delta t\, \widetilde{v}_s^{n+\frac{1}{2}\sharp}$, $d_s = \Delta t\, u_s^{n+\frac{1}{2}}$ and $w_f = \Delta t\, \widetilde{v}_f^{n+1}$ in (21) and (22) to obtain

$$\big(\widetilde{\mathcal{E}}_c^{n+1} - \mathcal{E}_c^n\big) + \big(\mathcal{E}_m^{n+1} - \mathcal{E}_m^n\big) + \frac{1}{2}\int_\Omega \rho_f \phi \left|\widetilde{v}_f^{n+1} - v_f^n\right|^2 \mathrm{d}x + \Delta t \int_\Omega \phi\, \sigma_f(\widetilde{v}_f^{n+1}) : \varepsilon(\widetilde{v}_f^{n+1})\,\mathrm{d}x - \Delta t \int_\Omega \phi^2 k_f^{-1}\Big(v_f^n - \widetilde{v}_s^{n+\frac{1}{2}\sharp}\Big) \cdot \widetilde{v}_s^{n+\frac{1}{2}\sharp}\,\mathrm{d}x + \Delta t \int_\Omega \phi^2 k_f^{-1}\Big(\widetilde{v}_f^{n+1} - \widetilde{v}_s^{n+\frac{1}{2}\sharp}\Big) \cdot \widetilde{v}_f^{n+1}\,\mathrm{d}x = 0.$$

The explicit part of the friction term requires a special treatment. Writing $v_f^n = \widetilde{v}_f^{n+1} + (v_f^n - \widetilde{v}_f^{n+1})$, it can be decomposed as

$$-\phi^2 k_f^{-1}\Big(v_f^n - \widetilde{v}_s^{n+\frac{1}{2}\sharp}\Big) \cdot \widetilde{v}_s^{n+\frac{1}{2}\sharp} + \phi^2 k_f^{-1}\Big(\widetilde{v}_f^{n+1} - \widetilde{v}_s^{n+\frac{1}{2}\sharp}\Big) \cdot \widetilde{v}_f^{n+1} = \phi^2 k_f^{-1}(\widetilde{v}_f^{n+1} - \widetilde{v}_s^{n+\frac{1}{2}\sharp})^2 - \phi^2 k_f^{-1}\big(v_f^n - \widetilde{v}_f^{n+1}\big) \cdot \widetilde{v}_s^{n+\frac{1}{2}\sharp},$$

so that the prediction step energy balance reads

$$\big(\widetilde{\mathcal{E}}_c^{n+1}-\mathcal{E}_c^n\big)+\big(\mathcal{E}_m^{n+1}-\mathcal{E}_m^n\big)+\frac{1}{2}\int_\Omega \rho_f\phi\left|\widetilde{v}_f^{n+1}-v_f^n\right|^2\,\mathrm{d}x+\Delta t\int_\Omega \phi\,\sigma_f(\widetilde{v}_f^{n+1}):\varepsilon(\widetilde{v}_f^{n+1})\,\mathrm{d}x \\ +\Delta t\int_\Omega \phi^2 k_f^{-1}\Big(\widetilde{v}_f^{n+1}-\widetilde{v}_s^{n+\frac{1}{2}\sharp}\Big)^2\,\mathrm{d}x=\Delta t\int_\Omega \phi^2 k_f^{-1}\big(v_f^n-\widetilde{v}_f^{n+1}\big)\cdot\widetilde{v}_s^{n+\frac{1}{2}\sharp}\,\mathrm{d}x, \quad (25)$$

where we recall the shortcut notation $k_f^{-1}\big(\widetilde{v}_f^{n+1}-\widetilde{v}_s^{n+\frac{1}{2}\sharp}\big)^2$ for $k_f^{-1}\big(\widetilde{v}_f^{n+1}-\widetilde{v}_s^{n+\frac{1}{2}\sharp}\big)\cdot\big(\widetilde{v}_f^{n+1}-\widetilde{v}_s^{n+\frac{1}{2}\sharp}\big)$. Now, testing (23) with $w_s=\Delta t\,v_s^{n+1}$, $w_f=\Delta t\,v_f^{n+1}$ and $q=\Delta t\,p^{n+1}$, we get the correction step energy balance

$$\big(\mathcal{E}_c^{n+1}-\widetilde{\mathcal{E}}_c^{n+1}\big)+\frac{1}{2}\int_\Omega \rho_s(1-\phi)\left|v_s^{n+1}-\widetilde{v}_s^{n+1}\right|^2\,\mathrm{d}x+\frac{1}{2}\int_\Omega \rho_f\phi\left|v_f^{n+1}-\widetilde{v}_f^{n+1}\right|^2\,\mathrm{d}x=0. \quad (26)$$

Summing up the prediction and correction steps contributions (25) and (26), the tentative kinetic energy $\widetilde{\mathcal{E}}_c^{n+1}$ simplifies and we end up with

$$\big(\mathcal{E}^{n+1}-\mathcal{E}^n\big)+\frac{1}{2}\int_\Omega \rho_f\phi\left|\widetilde{v}_f^{n+1}-v_f^n\right|^2\,\mathrm{d}x+\frac{1}{2}\int_\Omega \rho_s(1-\phi)\left|v_s^{n+1}-\widetilde{v}_s^{n+1}\right|^2\,\mathrm{d}x \\ +\frac{1}{2}\int_\Omega \rho_f\phi\left|v_f^{n+1}-\widetilde{v}_f^{n+1}\right|^2\,\mathrm{d}x+\Delta t\int_\Omega \phi\,\sigma_f(\widetilde{v}_f^{n+1}):\varepsilon(\widetilde{v}_f^{n+1})\,\mathrm{d}x \\ +\Delta t\int_\Omega \phi^2 k_f^{-1}\Big(\widetilde{v}_f^{n+1}-\widetilde{v}_s^{n+\frac{1}{2}\sharp}\Big)^2\,\mathrm{d}x=\Delta t\int_\Omega \phi^2 k_f^{-1}\big(v_f^n-\widetilde{v}_f^{n+1}\big)\cdot\widetilde{v}_s^{n+\frac{1}{2}\sharp}\,\mathrm{d}x, \quad (27)$$

where $\mathcal{E}^n$ corresponds to the total energy of the system, namely

$$\mathcal{E}^n=\mathcal{E}_c^n+\mathcal{E}_m^n=\frac{1}{2}\int_\Omega \rho_s(1-\phi)\,|v_s^n|^2\,\mathrm{d}x+\frac{1}{2}\int_\Omega \rho_f\phi\,\left|v_f^n\right|^2\,\mathrm{d}x+\frac{1}{2}\int_\Omega \sigma_s(u_s^n):\varepsilon(u_s^n)\,\mathrm{d}x.$$

The identity (27) corresponds to the discrete counterpart of the continuous energy balance (4), with additional terms associated with numerical dissipation and a different right-hand side coming from the explicit treatment of the permeability in the structure prediction step.

Remark 2.7. *Because of the midpoint discretization chosen for the solid, no numerical dissipation appears in the prediction step for the structure part. However, (27) includes a solid numerical dissipation term* $\frac{1}{2}\int_\Omega \rho_s(1-\phi)\left|\widetilde{v}_s^{n+1}-v_s^{n+1}\right|^2\,\mathrm{d}x$ *that comes from the correction step. It is possible to get rid of this term by changing the mixture divergence constraint (13c) into*

$$\operatorname{div}\Big((1-\phi)\frac{v_s^{n+1}+\widetilde{v}_s^{n+1}}{2}+\phi\,v_f^{n+1}\Big)=0,$$

and by testing (23) with $w_s=\frac{v_s^{n+1}+\widetilde{v}_s^{n+1}}{2}$ *instead of* $w_s=v_s^{n+1}$*. Nonetheless, we will see in the proof of Theorem 2.8 below that this solid numerical dissipation term is useful to control unsigned terms coming from the explicit treatment of the permeability.*

With the discrete energy balance (27) in hand, we are now ready to establish the following stability result.

Theorem 2.8. *Let* u_s^n*,* v_s^n*,* v_f^n*,* p^n*,* $\widetilde{v}_s^n$ *and* $\widetilde{v}_f^n$ *satisfy Scheme 1 with* $f=0$*. If the time step verifies*

$$\Delta t^2<\frac{\rho_f\rho_s(1-\phi_{\max})}{2\phi_{\max}^3(k_{\max}^{-1})^2}, \quad (28)$$

then for any $0 \leq N \leq n_T$*, it holds*

$$\mathcal{E}^N + \frac{3}{8}\sum_{n=0}^{N-1}\int_\Omega \rho_s(1-\phi)\left|\widetilde{v}_s^{n+1} - v_s^{n+1}\right|^2 \mathrm{d}x + \frac{1}{2}\sum_{n=0}^{N-1}\int_\Omega \rho_f\phi\left|\widetilde{v}_f^{n+1} - v_f^{n+1}\right|^2 \mathrm{d}x$$
$$+ \Delta t\sum_{n=0}^{N-1}\int_\Omega \phi\,\sigma_f(\widetilde{v}_f^{n+1}) : \varepsilon(\widetilde{v}_f^{n+1})\,\mathrm{d}x + \Delta t\sum_{n=0}^{N-1}\int_\Omega \phi^2 k_f^{-1}\left(\widetilde{v}_f^{n+1} - \widetilde{v}_s^{n+\frac{1}{2}\sharp}\right)^2 \mathrm{d}x \leq C_T\mathcal{E}^0, \quad (29)$$

with $C_T = \exp(\frac{T}{1-2C\Delta t^2})$.

Proof. The idea is to control the right-hand side of (27) thanks to the solid and fluid numerical dissipation. To do so, recalling (20), we decompose it as

$$\Delta t\int_\Omega \phi^2 k_f^{-1}\left(v_f^n - \widetilde{v}_f^{n+1}\right)\cdot\frac{1}{2}\left[\left(\widetilde{v}_s^{n+1} - v_s^{n+1}\right) + \left(v_s^{n+1} + v_s^n\right)\right]\mathrm{d}x. \quad (30)$$

Then, we use Young inequality on each part of the above decomposition to obtain

$$\begin{aligned}
&\Delta t\int_\Omega \phi^2 k_f^{-1}\left(v_f^n - \widetilde{v}_f^{n+1}\right)\cdot\left(\widetilde{v}_s^{n+1} - v_s^{n+1}\right)\mathrm{d}x\\
&\quad\leq \frac{1}{2}\int_\Omega \rho_f\phi\left|v_f^n - \widetilde{v}_f^{n+1}\right|^2 \mathrm{d}x + \frac{1}{2}\int_\Omega \frac{\Delta t^2\phi^4}{\rho_f\phi\rho_s(1-\phi)}\rho_s(1-\phi)k_f^{-2}\left(\widetilde{v}_s^{n+1} - v_s^{n+1}\right)^2\mathrm{d}x\\
&\quad\leq \frac{1}{2}\int_\Omega \rho_f\phi\left|v_f^n - \widetilde{v}_f^{n+1}\right|^2 \mathrm{d}x + \frac{1}{2}\int_\Omega \Delta t^2\frac{\phi_{\max}^3\left(k_{\max}^{-1}\right)^2}{\rho_f\rho_s(1-\phi_{\max})}\rho_s(1-\phi)\left|\widetilde{v}_s^{n+1} - v_s^{n+1}\right|^2\mathrm{d}x, \quad (31)
\end{aligned}$$

where we used the assumption (2) made on the permeability tensor. Likewise, we have

$$\begin{aligned}
&\Delta t\int_\Omega \phi^2 k_f^{-1}\left(v_f^n - \widetilde{v}_f^{n+1}\right)\cdot\left(v_s^{n+1} + v_s^n\right)\mathrm{d}x\\
&\qquad\leq \frac{1}{2}\int_\Omega \rho_f\phi\left|v_f^n - \widetilde{v}_f^{n+1}\right|^2 \mathrm{d}x + \frac{1}{2}\int_\Omega \Delta t^2\frac{\phi_{\max}^3(k_{\max}^{-1})^2}{\rho_f\rho_s(1-\phi_{\max})}\rho_s(1-\phi)\left|v_s^{n+1} + v_s^n\right|^2\mathrm{d}x. \quad (32)
\end{aligned}$$

Taking the half-sum of (31) and (32) and using that $\left|v_s^{n+1} + v_s^n\right|^2 \leq 2\left(\left|v_s^{n+1}\right|^2 + |v_s^n|^2\right)$, it follows that

$$\begin{aligned}
\Delta t\int_\Omega \phi^2 k_f^{-1}\left(v_f^n - \widetilde{v}_f^{n+1}\right)\cdot\widetilde{v}_s^{n+\frac{1}{2}\sharp}\,\mathrm{d}x &\leq \frac{1}{2}\int_\Omega \rho_f\phi\left|v_f^n - \widetilde{v}_f^{n+1}\right|^2\mathrm{d}x\\
&+ \frac{1}{4}\int_\Omega \Delta t^2\frac{\phi_{\max}^3\left(k_{\max}^{-1}\right)^2}{\rho_f\rho_s(1-\phi_{\max})}\rho_s(1-\phi)\left|\widetilde{v}_s^{n+1} - v_s^{n+1}\right|^2\mathrm{d}x\\
&+ \frac{1}{2}\int_\Omega \Delta t^2\frac{\phi_{\max}^3(k_{\max}^{-1})^2}{\rho_f\rho_s(1-\phi_{\max})}\rho_s(1-\phi)\left(\left|v_s^{n+1}\right|^2 + |v_s^n|^2\right)\mathrm{d}x. \quad (33)
\end{aligned}$$

Setting

$$C = \frac{\phi_{\max}^3(k_{\max}^{-1})^2}{\rho_f\rho_s(1-\phi_{\max})}, \quad (34)$$

the time step restriction (28) is equivalent to $C\Delta t^2 < 1/2$. Therefore, we observe

$$\begin{aligned}
\frac{1}{4}\int_\Omega \Delta t^2\frac{\phi_{\max}^3\left(k_{\max}^{-1}\right)^2}{\rho_f\rho_s(1-\phi_{\max})}\rho_s(1-\phi)\left|\widetilde{v}_s^{n+1} - v_s^{n+1}\right|^2\mathrm{d}x &= \frac{C\Delta t^2}{4}\int_\Omega \rho_s(1-\phi)\left|\widetilde{v}_s^{n+1} - v_s^{n+1}\right|^2\mathrm{d}x\\
&\leq \frac{1}{8}\int_\Omega \rho_s(1-\phi)\left|\widetilde{v}_s^{n+1} - v_s^{n+1}\right|^2\mathrm{d}x.
\end{aligned}$$

Consequently, plugging (33) into the discrete energy balance (27) yields

$$\begin{aligned}(\mathcal{E}^{n+1}-\mathcal{E}^n)+\frac{3}{8}\int_\Omega \rho_s(1-\phi)\left|\widetilde{v}_s^{n+1}-v_s^{n+1}\right|^2\,\mathrm{d}x+\frac{1}{2}\int_\Omega \rho_f\phi\left|\widetilde{v}_f^{n+1}-v_f^{n+1}\right|^2\,\mathrm{d}x\\ +\Delta t\int_\Omega \phi\,\sigma_f(\widetilde{v}_f^{n+1}):\varepsilon(\widetilde{v}_f^{n+1})\,\mathrm{d}x+\Delta t\int_\Omega \phi^2 k_f^{-1}\left(\widetilde{v}_f^{n+1}-\widetilde{v}_s^{n+\frac{1}{2}\sharp}\right)^2\mathrm{d}x\\ \leq\frac{1}{2}\int_\Omega \Delta t^2\frac{\phi_{\max}^3(k_{\max}^{-1})^2}{\rho_f\rho_s(1-\phi_{\max})}\rho_s(1-\phi)\left(\left|v_s^{n+1}\right|^2+|v_s^n|^2\right)\mathrm{d}x=C\Delta t^2\left(\mathcal{E}^{n+1}+\mathcal{E}^n\right).\end{aligned}$$

Summing this estimate between 0 and $N-1$, we deduce

$$\begin{aligned}\mathcal{E}^N+\frac{3}{8}\sum_{n=0}^{N-1}\int_\Omega \rho_s(1-\phi)\left|\widetilde{v}_s^{n+1}-v_s^{n+1}\right|^2\,\mathrm{d}x+\frac{1}{2}\sum_{n=0}^{N-1}\int_\Omega \rho_f\phi\left|\widetilde{v}_f^{n+1}-v_f^{n+1}\right|^2\,\mathrm{d}x\\ +\Delta t\sum_{n=0}^{N-1}\int_\Omega \phi\,\sigma_f(\widetilde{v}_f^{n+1}):\varepsilon(\widetilde{v}_f^{n+1})\,\mathrm{d}x+\Delta t\sum_{n=0}^{N-1}\int_\Omega \phi^2 k_f^{-1}\left(\widetilde{v}_f^{n+1}-\widetilde{v}_s^{n+\frac{1}{2}\sharp}\right)^2\mathrm{d}x\\ \leq\mathcal{E}^0+C\Delta t^2\sum_{n=0}^{N-1}\left(\mathcal{E}^{n+1}+\mathcal{E}^n\right)\leq\mathcal{E}^0+2C\Delta t^2\sum_{n=0}^{N}\mathcal{E}^n.\end{aligned}\tag{35}$$

The conclusion then follows from the following discrete version of Grönwall inequality, whose proof can for instance be found in [Heywood and Rannacher, 1990, Lemma 5.1].

Lemma 2.9. *Let $C>0$ and $\delta>0$. Let (a_n), (b_n) and (γ_n) be sequences of positive numbers such that*

$$a_N+\delta\sum_{n=0}^{N}b_n\leq C+\delta\sum_{n=0}^{N}\gamma_n a_n.$$

Assume that $\delta\gamma_n<1$ for any n, and set $\sigma_n=(1-\delta\gamma_n)^{-1}$. Then, for any $N\geq 0$, it holds that

$$a_N+\delta\sum_{n=0}^{N}b_n\leq C\exp\left(\delta\sum_{n=0}^{N}\sigma_n\gamma_n\right).$$

Indeed, the assumption (28) made on the time step is equivalent to $2C\Delta t^2<1$, so applying Lemma 2.9 to (35) directly implies (29). □

Remark 2.10. *In the viscous case $\nu_s>0$, an extra term*

$$\Delta t\int_\Omega \sigma_s^{vis}\left(\widetilde{v}_s^{n+\frac{1}{2}\sharp}\right):\varepsilon\left(\widetilde{v}_s^{n+\frac{1}{2}\sharp}\right)\mathrm{d}x,$$

appears in the left-hand side of (27). This viscous term can then be used to control the unsigned permeability term $\Delta t\int_\Omega \phi^2 k_f^{-1}\left(v_f^n-\widetilde{v}_f^{n+1}\right)\cdot\widetilde{v}_s^{n+\frac{1}{2}\sharp}\,\mathrm{d}x$ without using decomposition (30).

A similar result can be obtained for the incremental version of the scheme, whose weak form in absence of external body forces reads

Step 1: `(prediction step)`

– **Step 1.1**: (structure prediction sub-step)
Find $u_s^{n+1} \in [\mathrm{H}_0^1(\Omega)]^d$ and $\widetilde{v}_s^{n+1} \in [\mathrm{H}_0^1(\Omega)]^d$ such that, for any $(w_s, d_s) \in [\mathrm{H}_0^1(\Omega)]^d \times [\mathrm{H}_0^1(\Omega)]^d$,

$$\begin{aligned}\int_\Omega \rho_s(1-\phi)\frac{\widetilde{v}_s^{n+1}-v_s^n}{\Delta t}\cdot w_s\,\mathrm{d}x + \int_\Omega \sigma_s\Big(\frac{u_s^{n+1}-u_s^n}{\Delta t}\Big) : \varepsilon(d_s)\,\mathrm{d}x \\ - \int_\Omega \sigma_s(\widetilde{v}_s^{n+1}) : \varepsilon(d_s)\,\mathrm{d}x + \int_\Omega \sigma_s(u_s^{n+\frac{1}{2}}) : \varepsilon(w_s)\,\mathrm{d}x \\ - \int_\Omega \phi^2 k_f^{-1}(v_f^n - \widetilde{v}_s^{n+1})\cdot w_s\,\mathrm{d}x + \int_\Omega (1-\phi)\nabla p^n \cdot w_s\,\mathrm{d}x = 0. \quad (36)\end{aligned}$$

– **Step 1.2**: (fluid prediction sub-step)
Find $\widetilde{v}_f^{n+1} \in [\mathrm{H}_0^1(\Omega)]^d$ such that, for any $w_f \in [\mathrm{H}_0^1(\Omega)]^d$,

$$\begin{aligned}\int_\Omega \rho_f\phi\frac{\widetilde{v}_f^{n+1}-v_f^n}{\Delta t}\cdot w_f\,\mathrm{d}x + \int_\Omega \phi\,\sigma_f(\widetilde{v}_f^{n+1}) : \varepsilon(w_f)\,\mathrm{d}x \\ + \int_\Omega \phi^2 k_f^{-1}(\widetilde{v}_f^{n+1} - \widetilde{v}_s^{n+1})\cdot w_f\,\mathrm{d}x + \int_\Omega \phi\,\nabla p^n \cdot w_f\,\mathrm{d}x = 0. \quad (37)\end{aligned}$$

Step 2: (correction step)
Find $v_s^{n+1} \in [\mathrm{L}^2(\Omega)]^d$, $v_f^{n+1} \in [\mathrm{L}^2(\Omega)]^d$ and $p^{n+1} \in \mathrm{H}^1(\Omega)/\mathbb{R}$ such that, for any $w_s \in [\mathrm{L}^2(\Omega)]^d$, $w_f \in [\mathrm{L}^2(\Omega)]^d$ and $q \in \mathrm{H}^1(\Omega)/\mathbb{R}$,

$$\begin{aligned}\int_\Omega \rho_s(1-\phi)\frac{v_s^{n+1}-\widetilde{v}_s^{n+1}}{\Delta t}\cdot w_s\,\mathrm{d}x + \int_\Omega \rho_f\phi\frac{v_f^{n+1}-\widetilde{v}_f^{n+1}}{\Delta t}\cdot w_f\,\mathrm{d}x \\ + \int_\Omega (1-\phi)\nabla(p^{n+1}-p^n)\cdot w_s\,\mathrm{d}x + \int_\Omega \phi\,\nabla(p^{n+1}-p^n)\cdot w_f\,\mathrm{d}x \\ - \int_\Omega (1-\phi)v_s^{n+1}\cdot\nabla q\,\mathrm{d}x - \int_\Omega \phi\,v_f^{n+1}\cdot\nabla q\,\mathrm{d}x = 0. \quad (38)\end{aligned}$$

Theorem 2.11. *Let u_s^n, v_s^n, v_f^n, p^n, $\widetilde{v}_s^n$ and $\widetilde{v}_f^n$ satisfy Scheme 2, and assume that $p^0 \in \mathrm{H}^1(\Omega)/\mathbb{R}$. If the time step verifies (28), then for any $0 \le N \le n_T$, it holds*

$$\begin{aligned}\mathcal{E}^N + \frac{\Delta t^2}{2}\int_\Omega \rho_{\mathrm{eff}}^{-1}\left|\nabla p^N\right|^2\,\mathrm{d}x + \Delta t\sum_{n=0}^{N-1}\int_\Omega \phi\,\sigma_f(\widetilde{v}_f^{n+1}) : \varepsilon(\widetilde{v}_f^{n+1})\,\mathrm{d}x \\ + \Delta t\sum_{n=0}^{N-1}\int_\Omega \phi^2 k_f^{-1}\big(\widetilde{v}_f^{n+1}-\widetilde{v}_s^{n+1}\big)^2\,\mathrm{d}x \le C_T\Big(\mathcal{E}^0 + \frac{\Delta t^2}{2}\int_\Omega \rho_{\mathrm{eff}}^{-1}\left|\nabla p^0\right|^2\,\mathrm{d}x\Big), \quad (39)\end{aligned}$$

with $C_T = \exp(\frac{T}{1-2C\Delta t^2})$.

Proof. Choosing $d_s = \Delta t\, u_s^{n+\frac{1}{2}}$, $w_s = \Delta t\,\widetilde{v}_s^{n+1}$ and $w_f = \Delta t\,\widetilde{v}_f^{n+1}$ in (36) and (37), we have

$$\begin{aligned}\big(\widetilde{\mathcal{E}}_c^{n+1} - \mathcal{E}_c^n\big) + \big(\mathcal{E}_m^{n+1} - \mathcal{E}_m^n\big) + \frac{1}{2}\int_\Omega \rho_s(1-\phi)\left|\widetilde{v}_s^{n+1}-v_s^n\right|^2\,\mathrm{d}x + \frac{1}{2}\int_\Omega \rho_f\phi\left|\widetilde{v}_f^{n+1}-v_f^n\right|^2\,\mathrm{d}x \\ + \Delta t\int_\Omega \phi\,\sigma_f(\widetilde{v}_f^{n+1}) : \varepsilon(\widetilde{v}_f^{n+1})\,\mathrm{d}x + \Delta t\int_\Omega \phi^2 k_f^{-1}\big(\widetilde{v}_f^{n+1}-\widetilde{v}_s^{n+1}\big)^2\,\mathrm{d}x \\ + \Delta t\int_\Omega (1-\phi)\nabla p^n\cdot\widetilde{v}_s^{n+1}\,\mathrm{d}x + \Delta t\int_\Omega \phi\,\nabla p^n\cdot\widetilde{v}_f^{n+1}\,\mathrm{d}x \\ = \Delta t\int_\Omega \phi^2 k_f^{-1}\big(v_f^n-\widetilde{v}_f^{n+1}\big)\cdot\widetilde{v}_s^{n+1}\,\mathrm{d}x. \quad (40)\end{aligned}$$

Choosing $w_s = \Delta t\, v_s^{n+1}$, $w_f = \Delta t\, v_f^{n+1}$ and $q = \Delta t\, p^{n+1}$ as test functions in the correction step (38), the terms of the form $\Delta t \int_\Omega (1-\phi)\nabla p^{n+1}\cdot v_s^{n+1}\,\mathrm{d}x$ and $\Delta t\int_\Omega \phi\,\nabla p^{n+1}\cdot v_f^{n+1}\,\mathrm{d}x$ cancel out, so we obtain

$$\begin{aligned}\left(\mathcal{E}_c^{n+1} - \widetilde{\mathcal{E}}_c^{n+1}\right) + \frac{1}{2}\int_\Omega \rho_s(1-\phi)\left|v_s^{n+1} - \widetilde{v}_s^{n+1}\right|^2 \mathrm{d}x + \frac{1}{2}\int_\Omega \rho_f\phi\left|v_f^{n+1} - \widetilde{v}_f^{n+1}\right|^2 \mathrm{d}x \\ - \Delta t\int_\Omega (1-\phi)\nabla p^n\cdot v_s^{n+1}\,\mathrm{d}x - \Delta t\int_\Omega \phi\,\nabla p^n\cdot v_f^{n+1}\,\mathrm{d}x = 0. \quad (41)\end{aligned}$$

Summing (40) and (41), we infer

$$\begin{aligned}\left(\mathcal{E}^{n+1} - \mathcal{E}^n\right) + \frac{1}{2}\int_\Omega \rho_s(1-\phi)\left|\widetilde{v}_s^{n+1} - v_s^n\right|^2 \mathrm{d}x + \frac{1}{2}\int_\Omega \rho_f\phi\left|\widetilde{v}_f^{n+1} - v_f^n\right|^2 \mathrm{d}x \\ + \frac{1}{2}\int_\Omega \rho_s(1-\phi)\left|v_s^{n+1} - \widetilde{v}_s^{n+1}\right|^2 \mathrm{d}x + \frac{1}{2}\int_\Omega \rho_f\phi\left|v_f^{n+1} - \widetilde{v}_f^{n+1}\right|^2 \mathrm{d}x \\ + \Delta t\int_\Omega \phi\,\sigma_f(\widetilde{v}_f^{n+1}) : \varepsilon(\widetilde{v}_f^{n+1})\,\mathrm{d}x + \Delta t\int_\Omega \phi^2 k_f^{-1}\left(\widetilde{v}_f^{n+1} - \widetilde{v}_s^{n+1}\right)^2 \mathrm{d}x \\ + \Delta t\int_\Omega (1-\phi)\nabla p^n\cdot(\widetilde{v}_s^{n+1} - v_s^{n+1})\,\mathrm{d}x + \Delta t\int_\Omega \phi\,\nabla p^n\cdot(\widetilde{v}_f^{n+1} - v_f^{n+1})\,\mathrm{d}x \\ = \Delta t\int_\Omega \phi^2 k_f^{-1}\left(v_f^n - \widetilde{v}_f^{n+1}\right)\cdot\widetilde{v}_s^{n+1}\,\mathrm{d}x. \quad (42)\end{aligned}$$

The major difference between (42) and the energy balance of the non-incremental scheme (27) is the extra pressure terms coming from the explicit treatment of pressure, and the additional solid numerical dissipation term coming from using $\widetilde{v}_s^{n+\frac{1}{2}\sharp}$ instead of $\widetilde{v}_s^{n+1}$ in the prediction step.

To control the pressure terms, we choose $w_s = \frac{\Delta t^2}{\rho_s}\nabla p^n$, $w_f = \frac{\Delta t^2}{\rho_f}\nabla p^n$ and $q = 0$ as test functions in (38), to retrieve

$$\begin{aligned}\Delta t\int_\Omega (1-\phi)(v_s^{n+1} - \widetilde{v}_s^{n+1})\cdot\nabla p^n\,\mathrm{d}x + \Delta t\int_\Omega \phi\,(v_f^{n+1} - \widetilde{v}_f^{n+1})\cdot\nabla p^n\,\mathrm{d}x \\ + \Delta t^2\int_\Omega\left(\frac{1-\phi}{\rho_s} + \frac{\phi}{\rho_f}\right)\nabla(p^{n+1} - p^n)\cdot\nabla p^n\,\mathrm{d}x = 0.\end{aligned}$$

Since $\nabla(p^{n+1} - p^n)\cdot\nabla p^n = \frac{1}{2}\left(\left|\nabla p^{n+1}\right|^2 - |\nabla p^n|^2 - \left|\nabla(p^{n+1} - p^n)\right|^2\right)$, it follows that

$$\begin{aligned}\Delta t\int_\Omega (1-\phi)\nabla p^n\cdot(\widetilde{v}_s^{n+1} - v_s^{n+1})\,\mathrm{d}x + \Delta t\int_\Omega \phi\,\nabla p^n\cdot(\widetilde{v}_f^{n+1} - v_f^{n+1})\,\mathrm{d}x \\ \frac{\Delta t^2}{2}\int_\Omega\left(\frac{1-\phi}{\rho_s} + \frac{\phi}{\rho_f}\right)\left|\nabla p^{n+1}\right|^2\mathrm{d}x = \frac{\Delta t^2}{2}\int_\Omega\left(\frac{1-\phi}{\rho_s} + \frac{\phi}{\rho_f}\right)|\nabla p^n|^2\,\mathrm{d}x \\ + \frac{\Delta t^2}{2}\int_\Omega \frac{1-\phi}{\rho_s}\left|\nabla(p^{n+1} - p^n)\right|^2\mathrm{d}x + \frac{\Delta t^2}{2}\int_\Omega \frac{\phi}{\rho_f}\left|\nabla(p^{n+1} - p^n)\right|^2\mathrm{d}x.\end{aligned}$$

But from (19a), we know

$$\frac{\Delta t^2}{2}\left\|\sqrt{\frac{1-\phi}{\rho_s}}\nabla(p^{n+1} - p^n)\right\|^2 = \frac{\Delta t^2}{2}\left\|\sqrt{\rho_s(1-\phi)}\frac{v_s^{n+1} - \widetilde{v}_s^{n+1}}{\Delta t}\right\|^2 = \frac{1}{2}\int_\Omega \rho_s(1-\phi)\left|v_s^{n+1} - \widetilde{v}_s^{n+1}\right|^2\mathrm{d}x,$$

and hence

$$\Delta t \int_\Omega (1-\phi)\nabla p^n \cdot (\widetilde{v}_s^{n+1} - v_s^{n+1})\,\mathrm{d}x$$
$$= \frac{\Delta t^2}{2}\left(\int_\Omega \frac{1-\phi}{\rho_s}\left|\nabla p^{n+1}\right|^2 \mathrm{d}x - \int_\Omega \frac{1-\phi}{\rho_s}\left|\nabla p^n\right|^2 \mathrm{d}x\right) + \frac{1}{2}\int_\Omega \rho_s(1-\phi)\left|v_s^{n+1} - \widetilde{v}_s^{n+1}\right|^2 \mathrm{d}x. \quad (43)$$

Proceeding similarly for the fluid correction step, we find that

$$\Delta t \int_\Omega \phi\,\nabla p^n \cdot (\widetilde{v}_f^{n+1} - v_f^{n+1})\,\mathrm{d}x$$
$$= \frac{\Delta t^2}{2}\left(\int_\Omega \frac{\phi}{\rho_f}\left|\nabla p^{n+1}\right|^2 \mathrm{d}x - \int_\Omega \frac{\phi}{\rho_f}\left|\nabla p^n\right|^2 \mathrm{d}x\right) + \frac{1}{2}\int_\Omega \rho_f\phi\left|v_f^{n+1} - \widetilde{v}_f^{n+1}\right|^2 \mathrm{d}x. \quad (44)$$

Combining (42) with (43) and (44), the numerical dissipation terms from the correction step vanish and we deduce

$$\left(\mathcal{E}^{n+1} - \mathcal{E}^n\right) + \frac{1}{2}\int_\Omega \rho_s(1-\phi)\left|\widetilde{v}_s^{n+1} - v_s^n\right|^2 \mathrm{d}x + \frac{1}{2}\int_\Omega \rho_f\phi\left|\widetilde{v}_f^{n+1} - v_f^n\right|^2 \mathrm{d}x$$
$$+ \Delta t\int_\Omega \phi\,\sigma_f(\widetilde{v}_f^{n+1}) : \varepsilon(\widetilde{v}_f^{n+1})\,\mathrm{d}x + \Delta t\int_\Omega \phi^2 k_f^{-1}\left(\widetilde{v}_f^{n+1} - \widetilde{v}_s^{n+1}\right)^2 \mathrm{d}x$$
$$+ \frac{\Delta t^2}{2}\left(\int_\Omega \rho_{\mathrm{eff}}^{-1}\left|\nabla p^{n+1}\right|^2 \mathrm{d}x - \int_\Omega \rho_{\mathrm{eff}}^{-1}\left|\nabla p^n\right|^2 \mathrm{d}x\right) = \Delta t\int_\Omega \phi^2 k_f^{-1}\left(v_f^n - \widetilde{v}_f^{n+1}\right)\cdot \widetilde{v}_s^{n+1}\,\mathrm{d}x, \quad (45)$$

where we recall that $\rho_{\mathrm{eff}}^{-1} = \frac{1-\phi}{\rho_s} + \frac{\phi}{\rho_f}$ as in the Poisson problem (14).

The end of the proof is similar to that of Theorem 2.8. Defining C as in (34), Young inequality implies that

$$\Delta t \int_\Omega \phi^2 k_f^{-1}\left(v_f^n - \widetilde{v}_f^{n+1}\right)\cdot \widetilde{v}_s^{n+1}\,\mathrm{d}x$$
$$= \Delta t\int_\Omega \phi^2 k_f^{-1}\left(v_f^n - \widetilde{v}_f^{n+1}\right)\cdot (\widetilde{v}_s^{n+1} - v_s^n)\,\mathrm{d}x + \Delta t\int_\Omega \phi^2 k_f^{-1}\left(v_f^n - \widetilde{v}_f^{n+1}\right)\cdot v_s^n\,\mathrm{d}x$$
$$\leq \frac{1}{2}\int_\Omega \rho_f\phi\left|v_f^n - \widetilde{v}_f^{n+1}\right|^2 \mathrm{d}x + C\Delta t^2\int_\Omega \rho_s(1-\phi)\left|\widetilde{v}_s^{n+1} - v_s^n\right|^2 \mathrm{d}x + C\Delta t^2\int_\Omega \rho_s(1-\phi)\left|v_s^n\right|^2 \mathrm{d}x. \quad (46)$$

Plugging this result into (45) and recalling that $C\Delta t^2 < 1/2$, we finally get

$$\left(\mathcal{E}^{n+1} - \mathcal{E}^n\right) + \Delta t\int_\Omega \phi\,\sigma_f(\widetilde{v}_f^{n+1}) : \varepsilon(\widetilde{v}_f^{n+1})\,\mathrm{d}x + \Delta t\int_\Omega \phi^2 k_f^{-1}\left(\widetilde{v}_f^{n+1} - \widetilde{v}_s^{n+1}\right)^2 \mathrm{d}x$$
$$+ \frac{\Delta t^2}{2}\left(\int_\Omega \rho_{\mathrm{eff}}^{-1}\left|\nabla p^{n+1}\right|^2 \mathrm{d}x - \int_\Omega \rho_{\mathrm{eff}}^{-1}\left|\nabla p^n\right|^2 \mathrm{d}x\right) \leq 2C\Delta t^2\mathcal{E}^n,$$

and we conclude by an application of discrete Grönwall's lemma. □

Remark 2.12. *In the estimate (46), we see that we need to control $\int_\Omega \phi^2 k_f^{-1}\left(\widetilde{v}_f^{n+1} - \widetilde{v}_s^n\right)^2$ and thus we need a numerical dissipation term coming from the prediction step. This is the reason why we have chosen to replace the midpoint velocity $\widetilde{v}_s^{n+\frac{1}{2}\sharp}$ by $\widetilde{v}_s^{n+1}$ in Scheme 2. Note that previously the dissipation induced by the correction step was sufficient to control the unsigned residual friction term, nevertheless here this dissipation is completly absorbed by last terms of (43) and (44).*

Remark 2.13. *Note that the stability of the incremental version of the scheme requires more regularity on the pressure than the non-incremental version since (39) requires that $p(0) \in \mathrm{H}^1(\Omega)$.*

Remark 2.14 (Neumann boundary conditions)**.** *We can easily adapt the previous analysis to the case of Neumann boundary conditions* (8) *on a part of the boundary, considering* $\Gamma_T = \emptyset$ *and*

$$\begin{aligned} \sigma_s(u_s)n - (1-\phi)\, pn &= (1-\phi)\, b, \qquad \text{on } \Gamma_N, \\ \phi\, \sigma_f(v_f)n - \phi\, pn &= \phi\, b, \qquad \text{on } \Gamma_N, \end{aligned}$$

with $b \in [\mathrm{L}^2(\Gamma_N)]^d$*. A consistent way to impose* (8) *in Scheme 1, is then to split the boundary traction* b *applied to the porous medium be between the projection and correction steps. To do so, we are going to impose its tangential component in the prediction step, while its normal component will be imposed in the correction step. More precisely, in the solid prediction sub-step* (11)*, we impose weakly*

$$\sigma_s(u_s^{n+\frac{1}{2}})n = (1-\phi)\, \pi_\tau(b^{n+\frac{1}{2}}), \qquad \text{on } \Gamma_N.$$

Similarly, in the fluid prediction sub-step (12)*, we impose weakly*

$$\phi\, \sigma_f(\widetilde{v}_f^{n+1})n = \phi\, \pi_\tau(b^{n+\frac{1}{2}}), \qquad \text{on } \Gamma_N.$$

Then, the normal component of the external traction is imposed in the correction step (13) *as a Dirichlet boundary condition on the pressure, namely*

$$p^{n+1} = -b^{n+\frac{1}{2}} \cdot n, \qquad \text{on } \Gamma_N.$$

To conclude this section, we have proved stability estimates for both the non-incremental and incremental versions of the projection scheme. However, the estimates of Theorems 2.8 and 2.11 are subject to the time step restriction (28), namely

$$\Delta t^2 < \frac{\rho_f \rho_s (1-\phi_{\max})}{2\phi_{\max}^3 (k_{\max}^{-1})^2}.$$

If the permeability tensor is small, *i.e.* if $k_{\max}^{-1}$ is large, this condition can be *very restrictive* in practice. As a matter of fact, in biological applications, k_f typically takes values between 10^{-9} and $10^{-12}\,\mathrm{m^2\,Pa^{-1}\,s^{-1}}$, so that for realistic density values – say $\rho_s = \rho_f = 10^3\,\mathrm{kg\,m^{-3}}$ – the time step condition (28) becomes $\Delta t \lesssim 10^{-6}\,\mathrm{s}$. In order to overcome this time step restriction, we are now going to present two other variants of the scheme.

2.3 Other treatments of permeability

The time step condition (28) comes from the explicit treatment of the fluid velocity in the permeability term during the solid prediction sub-step (11a). It is possible to treat implicitly this term by recoupling the solid and fluid prediction sub-steps, leading to the following scheme. To shorten the presentation the next scheme includes both non-incremental and incremental versions thanks to a parameter $i \in \{0, 1\}$ with the convention

$$i = \begin{cases} 0 & \text{for the non-incremental version of the scheme,} \\ 1 & \text{for the incremental version of the scheme.} \end{cases}$$

Scheme 3 Implicit treatment of permeability

Step 1: `(prediction step)`

Find u_s^{n+1}, $\widetilde{v}_s^{n+1}$ and $\widetilde{v}_f^{n+1}$ such that $u_s^{n+1}|_{\Gamma_D} = \widetilde{v}_s^{n+1}|_{\Gamma_D} = \widetilde{v}_f^{n+1}|_{\Gamma_D} = 0$ and

$$\begin{cases} \rho_s(1-\phi)\dfrac{\widetilde{v}_s^{n+1}-v_s^n}{\Delta t} - \operatorname{div}\big(\sigma_s(u_s^{n+\frac{1}{2}})\big) \\ \qquad\qquad - \phi^2 k_f^{-1}\Big(\widetilde{v}_f^{n+1} - \dfrac{\widetilde{v}_s^{n+1}+v_s^n}{2} + i\dfrac{\widetilde{v}_s^{n+1}-v_s^n}{2}\Big) + (1-\phi)\nabla i p^n = \rho_s(1-\phi) f^{n+\frac{1}{2}}, \\ \rho_f\phi\dfrac{\widetilde{v}_f^{n+1}-v_f^n}{\Delta t} - \operatorname{div}\big(\phi\,\sigma_f(\widetilde{v}_f^{n+1})\big) \\ \qquad\qquad + \phi^2 k_f^{-1}\Big(\widetilde{v}_f^{n+1} - \dfrac{\widetilde{v}_s^{n+1}+v_s^n}{2} + i\dfrac{\widetilde{v}_s^{n+1}-v_s^n}{2}\Big) + \phi\,\nabla i p^n = \rho_f\phi\, f^{n+\frac{1}{2}}, \\ \dfrac{u_s^{n+1}-u_s^n}{\Delta t} = \dfrac{\widetilde{v}_s^{n+1}+v_s^n}{2} + i\dfrac{\widetilde{v}_s^{n+1}-v_s^n}{2}. \end{cases}$$

Step 2: `(correction step)`
Find v_s^{n+1}, v_f^{n+1} and p^{n+1} such that $\int_\Omega p^{n+1}\,\mathrm{d}x = 0$ and

$$\begin{cases} \rho_s(1-\phi)\dfrac{v_s^{n+1}-\widetilde{v}_s^{n+1}}{\Delta t} + (1-\phi)\,\nabla(p^{n+1}-ip^n) = 0, \\ \rho_f\phi\dfrac{v_f^{n+1}-\widetilde{v}_f^{n+1}}{\Delta t} + \phi\,\nabla(p^{n+1}-ip^n) = 0, \\ \operatorname{div}\big((1-\phi)v_s^{n+1} + \phi\, v_f^{n+1}\big) = 0, \\ \big((1-\phi)v_s^{n+1} + \phi\, v_f^{n+1}\big)\cdot n|_{\Gamma_D} = 0. \end{cases}$$

The drawback of this scheme is that it requires to couple the solid and fluid degrees of freedom to solve the prediction step. Its main advantage is to totally get rid of the time step restriction (28). As a matter of fact, assuming that $f = 0$ and reproducing the computations made for the stability analysis of Scheme 1, the discrete energy balance associated in the non-incremental case reads

$$\begin{aligned} \big(\mathcal{E}^{n+1}-\mathcal{E}^n\big) + \frac{1}{2}\int_\Omega \rho_f\phi\left|\widetilde{v}_f^{n+1}-v_f^n\right|^2\mathrm{d}x + \frac{1}{2}\int_\Omega \rho_s(1-\phi)\left|v_s^{n+1}-\widetilde{v}_s^{n+1}\right|^2\mathrm{d}x \\ + \frac{1}{2}\int_\Omega \rho_f\phi\left|v_f^{n+1}-\widetilde{v}_f^{n+1}\right|^2\mathrm{d}x + \Delta t\int_\Omega \phi\,\sigma_f(\widetilde{v}_f^{n+1}) : \varepsilon(\widetilde{v}_f^{n+1})\,\mathrm{d}x \\ + \Delta t\int_\Omega \phi^2 k_f^{-1}\Big(\widetilde{v}_f^{n+1} - \widetilde{v}_s^{n+1\,\sharp}\Big)^2\mathrm{d}x = 0, \end{aligned} \tag{47}$$

whereas for the incremental case, one has

$$\begin{aligned} \big(\mathcal{E}^{n+1}-\mathcal{E}^n\big) + \frac{1}{2}\int_\Omega \rho_s(1-\phi)\left|\widetilde{v}_s^{n+1}-v_s^n\right|^2\mathrm{d}x + \frac{1}{2}\int_\Omega \rho_f\phi\left|\widetilde{v}_f^{n+1}-v_f^n\right|^2\mathrm{d}x \\ + \Delta t\int_\Omega \phi\,\sigma_f(\widetilde{v}_f^{n+1}) : \varepsilon(\widetilde{v}_f^{n+1})\,\mathrm{d}x + \Delta t\int_\Omega \phi^2 k_f^{-1}\big(\widetilde{v}_f^{n+1} - \widetilde{v}_s^{n+1}\big)^2\mathrm{d}x \\ + \frac{\Delta t^2}{2}\left(\int_\Omega \rho_{\mathrm{eff}}^{-1}\left|\nabla p^{n+1}\right|^2\mathrm{d}x - \int_\Omega \rho_{\mathrm{eff}}^{-1}\left|\nabla p^n\right|^2\mathrm{d}x\right) = 0. \end{aligned} \tag{48}$$

This directly proves the unconditional stability of the scheme.

Note finally, if one is attached to decouple the solid and fluid degrees of freedom during the prediction step, an option is to use a fixed-point strategy where we iterate between the solid and fluid prediction sub-steps until a convergence criterion is reached. In particular, approaches based on the Newton-Raphson descent algorithm are known to converge with a limited number of iterations and thus represent a good compromise between the property of unconditional stability and the number of required fixed-point iterations.

2.4 Total stress boundary conditions

In many applications, boundary conditions appear on the solid or fluid stresses, with an additional coupling condition between the fluid and solid velocities, see (9). The goal of this section is to include such more intricate conditions in the projection scheme presented previously. For the sake of conciseness, we will only consider the non-incremental version of the algorithm.

Let us assume that the total stress boundary condition (9) holds on Γ_T, and $\Gamma_N = \emptyset$. As mentioned previously, this kind of boundary conditions is very close to the transmission conditions encountered in fluid-structure interaction. Moreover, as in fluid-structure interaction problems, the incompressibility constraint (3d) may cause an added-mass effect responsible of numerical unstabilities.

A first option is to treat explicitly the fluid stress part of this condition. This consists in imposing weakly

$$\sigma_s(u_s^{n+\frac{1}{2}})n = \pi_\tau(b^{n+\frac{1}{2}}) - \phi\,\sigma_f(v_f^n)n, \quad \text{on } \Gamma_T, \tag{49}$$

in the structure prediction sub-step. Then, knowing $\widetilde{v}_s^{n+1}$, the fluid and solid velocities equality is imposed strongly by setting

$$\widetilde{v}_f^{n+1} = \widetilde{v}_s^{n+1}, \quad \text{on } \Gamma_T, \tag{50}$$

in the fluid prediction sub-step. Finally, as for Neumann boundary conditions, the external traction normal component is taken into account by imposing strongly

$$p^{n+1} = -b^{n+\frac{1}{2}} \cdot n, \quad \text{on } \Gamma_T, \tag{51}$$

in the correction step. This strategy leads to a consistent formulation. Yet, when performing the stability analysis of the solid prediction step, it introduces an additional term of the form $\int_{\Gamma_T} \phi\,\sigma_f(v_f^n)n \cdot \widetilde{v}_s^{n+\frac{1}{2}\sharp}\,\mathrm{d}S$ on the boundary that cannot be controlled irrespectively of the mesh size and hence may imposes a CFL condition and may cause numerical instabilities, see Section 4.4. As it will be confirmed in Section 4.4 this is not an added mass effect since here the porous model is considered as a single media and the correction step corrects the velocity of the mixture. Moreover the explicit steps appears in the prediction step that consists mainly in an heat/wave coupling.

To get read of a possible CFL condition, we are going instead to use a Robin-Robin coupling approach that was introduced in the context of fluid-structure interaction problems in [Burman et al., 2022b,a], but also proposed and analyzed for general parabolic/parabolic and hyperbolic/parabolic problems [Burman et al., 2021]. These studies generalize the Robin method developed in [Burman and Fernández, 2014] and improve the uniformity of the time splitting error with respect to the mesh size h, which is often of order $\mathcal{O}(\Delta t/h)$ in Nitsche's methods [Hansbo et al., 2004; Burman and Fernández, 2009]. Here, we are going to adapt the Robin-based algorithm from [Burman et al., 2022b,a] in the prediction step, and show that the correction step can then be handled as in the case of Neumann boundary conditions, here again *without any destabilizing added-mass effect*. Let us denote by $\alpha > 0$ the Robin coefficient of the method. In our context the Robin-Robin splitting approach associated to the boundary conditions (9) consists on imposing weakly

$$\sigma_s(u_s^{n+\frac{1}{2}})n + \alpha\widetilde{v}_s^{n+\frac{1}{2}\sharp} = (1-\phi)\pi_\tau(b^{n+\frac{1}{2}}) + \alpha\widetilde{v}_f^n - \phi\,\sigma_f(\widetilde{v}_f^n)n, \quad \text{on } \Gamma_T, \tag{52}$$

in the solid prediction sub-step (11a), and imposing weakly

$$\phi\,\sigma_f(\widetilde{v}_f^{n+1})n + \alpha\widetilde{v}_f^{n+1} = \phi\,\pi_\tau(b^{n+\frac{1}{2}}) + \alpha\widetilde{v}_s^{n+\frac{1}{2}\sharp} + \phi\,\sigma_f(\widetilde{v}_f^n)n \quad \text{on } \Gamma_T, \tag{53}$$

in the fluid prediction sub-step. Then, as for Neumann boundary conditions, we impose strongly

$$p^{n+1} = -b^{n+\frac{1}{2}} \cdot n, \quad \text{on } \Gamma_T,$$

in the correction step. Introducing the notation

$$\widetilde{\lambda}^n = \phi\,\sigma_f(\widetilde{v}_f^n)n,$$

for the tentative fluid traction, we respectively get from (52) and (53) that, $\forall w_s \in [\mathrm{H}^1(\Omega)]^d$,

$$-\int_{\Gamma_T} \sigma_s(u_s^{n+\frac{1}{2}})n \cdot w_s \,\mathrm{d}S = \alpha \int_{\Gamma_T} (\widetilde{v}_s^{n+\frac{1}{2}\sharp} - \widetilde{v}_f^n) \cdot w_s \,\mathrm{d}S + \int_{\Gamma_T} \widetilde{\lambda}^n \cdot w_s \,\mathrm{d}S - \int_{\Gamma_T} (1-\phi)\pi_\tau(b^{n+\frac{1}{2}}) \cdot w_s \,\mathrm{d}S,$$

and, $\forall w_f \in [\mathrm{H}^1(\Omega)]^d$,

$$-\int_{\Gamma_T} \phi\, \sigma_f(\widetilde{v}_f^{n+1})n \cdot w_f \,\mathrm{d}S = \alpha \int_{\Gamma_T} (\widetilde{v}_f^{n+1} - \widetilde{v}_s^{n+\frac{1}{2}\sharp}) \cdot w_f \,\mathrm{d}S - \int_{\Gamma_T} \widetilde{\lambda}^n \cdot w_f - \int_{\Gamma_T} \phi\, \pi_\tau(b^{n+\frac{1}{2}}) \cdot w_f \,\mathrm{d}S,$$

which results in the following weak formulation.

Scheme 4 Robin-Robin coupling for total stress boundary conditions

---

Step 1: `(prediction step)`

– **Step 1.1**: `(structure prediction sub-step)`
Find $u_s^{n+1} \in [\mathrm{H}^1_{0,\Gamma_D}(\Omega)]^d$ and $\widetilde{v}_s^{n+1} \in [\mathrm{H}^1_{0,\Gamma_D}(\Omega)]^d$ such that, for any $w_s \in [\mathrm{H}^1_{0,\Gamma_D}(\Omega)]^d$ and $d_s \in [\mathrm{H}^1_{0,\Gamma_D}(\Omega)]^d$,

$$\begin{aligned}
&\int_\Omega \rho_s(1-\phi)\frac{\widetilde{v}_s^{n+1} - v_s^n}{\Delta t} \cdot w_s \,\mathrm{d}x + \int_\Omega \sigma_s\Big(\frac{u_s^{n+1} - u_s^n}{\Delta t}\Big) : \varepsilon(d_s)\,\mathrm{d}x \\
&\quad - \int_\Omega \sigma_s(\widetilde{v}_s^{n+\frac{1}{2}\sharp}) : \varepsilon(d_s)\,\mathrm{d}x + \int_\Omega \sigma_s(u_s^{n+\frac{1}{2}}) : \varepsilon(w_s)\,\mathrm{d}x - \int_\Omega \phi^2 k_f^{-1}(v_f^n - \widetilde{v}_s^{n+\frac{1}{2}\sharp}) \cdot w_s \,\mathrm{d}x \\
&\qquad + \alpha \int_{\Gamma_T} (\widetilde{v}_s^{n+\frac{1}{2}\sharp} - \widetilde{v}_f^n) \cdot w_s \,\mathrm{d}S + \int_{\Gamma_T} \widetilde{\lambda}^n \cdot w_s \,\mathrm{d}S \\
&\qquad = \int_\Omega \rho_s(1-\phi) f^{n+\frac{1}{2}} \cdot w_s \,\mathrm{d}x + \int_{\Gamma_T} (1-\phi)\,\pi_\tau(b^{n+\frac{1}{2}}) \cdot w_s \,\mathrm{d}S. \quad (54)
\end{aligned}$$

– **Step 1.2**: `(fluid prediction sub-step)`
Find $\widetilde{v}_f^{n+1} \in [\mathrm{H}^1_{0,\Gamma_D}(\Omega)]^d$ such that, for any $w_f \in [\mathrm{H}^1_{0,\Gamma_D}(\Omega)]^d$,

$$\begin{aligned}
&\int_\Omega \rho_f \phi \frac{\widetilde{v}_f^{n+1} - v_f^n}{\Delta t} \cdot w_f \,\mathrm{d}x + \int_\Omega \phi\, \sigma_f(\widetilde{v}_f^{n+1}) : \varepsilon(w_f)\,\mathrm{d}x \\
&\quad + \int_\Omega \phi^2 k_f^{-1}(\widetilde{v}_f^{n+1} - \widetilde{v}_s^{n+\frac{1}{2}\sharp}) \cdot w_f \,\mathrm{d}x + \alpha \int_{\Gamma_T} (\widetilde{v}_f^{n+1} - \widetilde{v}_s^{n+\frac{1}{2}\sharp}) \cdot w_f \,\mathrm{d}S - \int_{\Gamma_T} \widetilde{\lambda}^n \cdot w_f \\
&\qquad = \int_\Omega \rho_f \phi\, f^{n+\frac{1}{2}} \cdot w_f \,\mathrm{d}x + \int_{\Gamma_T} \phi\, \pi_\tau(b^{n+\frac{1}{2}}) \cdot w_f \,\mathrm{d}S, \quad (55)
\end{aligned}$$

Step 2: `(correction step)`
Find $v_s^{n+1} \in [\mathrm{L}^2(\Omega)]^d$, $v_f^{n+1} \in [\mathrm{L}^2(\Omega)]^d$ and $p^{n+1} \in \mathrm{H}^1(\Omega)$ with $p^{n+1}|_{\Gamma_N} = -b^{n+\frac{1}{2}} \cdot n$ such that, for any $w_s \in [\mathrm{L}^2(\Omega)]^d$, $w_f \in [\mathrm{L}^2(\Omega)]^d$ and $q \in \mathrm{H}^1(\Omega)$,

$$\begin{aligned}
&\int_\Omega \rho_s(1-\phi)\frac{v_s^{n+1} - \widetilde{v}_s^{n+1}}{\Delta t} \cdot w_s \,\mathrm{d}x + \int_\Omega \rho_f \phi \frac{v_f^{n+1} - \widetilde{v}_f^{n+1}}{\Delta t} \cdot w_f \,\mathrm{d}x \\
&\qquad + \int_\Omega (1-\phi)\nabla p^{n+1} \cdot w_s \,\mathrm{d}x + \int_\Omega \phi\, \nabla p^{n+1} \cdot w_f \,\mathrm{d}x \\
&\qquad - \int_\Omega (1-\phi) v_s^{n+1} \cdot \nabla q \,\mathrm{d}x - \int_\Omega \phi\, v_f^{n+1} \cdot \nabla q \,\mathrm{d}x = 0, \quad (56)
\end{aligned}$$

Note that from (53), we infer

$$\widetilde{\lambda}^{n+1} = \widetilde{\lambda}^{n} + \alpha\big(\widetilde{v}_s^{n+\frac{1}{2}\sharp} - \widetilde{v}_f^{n+1}\big) + \phi\,\pi_\tau(b^{n+\frac{1}{2}}), \quad \text{on } \Gamma_T. \tag{57}$$

This relation can be used to update the field $\widetilde{\lambda}^{n+1}$ after the fluid prediction sub-step, so that the unknown $\widetilde{\lambda}^{n}$ does not need to be solved like an additional one. Moreover, (57) will be crucial for the stability analysis that we are now going to carry out.

Theorem 2.15. *Let u_s^n, v_s^n, v_f^n, p^n, $\widetilde{v}_s^n$ and $\widetilde{v}_f^n$ satisfy Scheme 4 with $f = 0$ and $b = 0$. If the time step verifies the smallness condition (28), then for any $0 \le N \le n_T$, it holds*

$$\begin{aligned}
\mathcal{E}^N + \frac{\Delta t}{2\alpha}\int_{\Gamma_T}\left|\widetilde{\lambda}^N\right|^2 \mathrm{d}S + \frac{\alpha\Delta t}{2}\int_{\Gamma_T}\left|\widetilde{v}_f^N\right|^2 \mathrm{d}S + \frac{\alpha\Delta t}{2}\sum_{n=0}^{N-1}\int_{\Gamma_T}\left|\widetilde{v}_s^{n+\frac{1}{2}\sharp} - \widetilde{v}_f^n\right|^2 \mathrm{d}S \\
+ \frac{3}{8}\sum_{n=0}^{N-1}\int_\Omega \rho_s(1-\phi)\left|\widetilde{v}_s^{n+1} - v_s^{n+1}\right|^2 \mathrm{d}x + \frac{1}{2}\sum_{n=0}^{N-1}\int_\Omega \rho_f\phi\left|\widetilde{v}_f^{n+1} - v_f^{n+1}\right|^2 \mathrm{d}x \\
+ \Delta t\sum_{n=0}^{N-1}\int_\Omega \phi\,\sigma_f(\widetilde{v}_f^{n+1}) : \varepsilon(\widetilde{v}_f^{n+1})\,\mathrm{d}x + \Delta t\sum_{n=0}^{N-1}\int_\Omega \phi^2 k_f^{-1}\left(\widetilde{v}_f^{n+1} - \widetilde{v}_s^{n+\frac{1}{2}\sharp}\right)^2 \mathrm{d}x \\
\le C_T\left(\mathcal{E}^0 + \frac{\Delta t}{2\alpha}\int_{\Gamma_T}\left|\widetilde{\lambda}^0\right|^2 \mathrm{d}S + \frac{\alpha\Delta t}{2}\int_{\Gamma_T}\left|\widetilde{v}_f^0\right|^2 \mathrm{d}S\right),
\end{aligned} \tag{58}$$

with $C_T > 0$.

Proof. To obtain the discrete energy balance of Scheme 4, we proceed as for Scheme 1. Testing (54) with $w_s = \Delta t\,\widetilde{v}_s^{n+\frac{1}{2}\sharp}$ and $d_s = \Delta t\,u_s^{n+\frac{1}{2}}$, (55) with $w_f = \Delta t\,\widetilde{v}_f^{n+1}$ and (56) with $w_s = \Delta t\,\widetilde{v}_s^{n+1}$, $w_f = \Delta t\,\widetilde{v}_f^{n+1}$ and $q = \Delta t\,p^{n+1}$, and summing the prediction and correction contributions, we get

$$\begin{aligned}
&(\mathcal{E}^{n+1} - \mathcal{E}^n) + \frac{1}{2}\int_\Omega \rho_f\phi\left|\widetilde{v}_f^{n+1} - v_f^n\right|^2 \mathrm{d}x + \frac{1}{2}\int_\Omega \rho_s(1-\phi)\left|v_s^{n+1} - \widetilde{v}_s^{n+1}\right|^2 \mathrm{d}x \\
&\quad + \frac{1}{2}\int_\Omega \rho_f\phi\left|v_f^{n+1} - \widetilde{v}_f^{n+1}\right|^2 \mathrm{d}x + \Delta t\int_\Omega \phi\,\sigma_f(\widetilde{v}_f^{n+1}) : \varepsilon(\widetilde{v}_f^{n+1})\,\mathrm{d}x + \Delta t\int_\Omega \phi^2 k_f^{-1}\left(\widetilde{v}_f^{n+1} - \widetilde{v}_s^{n+\frac{1}{2}\sharp}\right)^2 \mathrm{d}x \\
&+ \alpha\Delta t\int_{\Gamma_T}(\widetilde{v}_s^{n+\frac{1}{2}\sharp} - \widetilde{v}_f^n)\cdot\widetilde{v}_s^{n+\frac{1}{2}\sharp}\,\mathrm{d}S + \Delta t\int_{\Gamma_T}\widetilde{\lambda}^n\cdot(\widetilde{v}_s^{n+\frac{1}{2}\sharp} - \widetilde{v}_f^{n+1})\,\mathrm{d}S + \alpha\Delta t\int_{\Gamma_T}(\widetilde{v}_f^{n+1} - \widetilde{v}_s^{n+\frac{1}{2}\sharp})\cdot\widetilde{v}_f^{n+1}\,\mathrm{d}S \\
&\qquad = \Delta t\int_\Omega \phi^2 k_f^{-1}(v_f^n - \widetilde{v}_f^{n+1})\cdot\widetilde{v}_s^{n+\frac{1}{2}\sharp}\,\mathrm{d}x,
\end{aligned} \tag{59}$$

The energy balance (59) is almost the same than (27). The only terms that needs a special attention are the ones on the boundary, namely

$$\begin{aligned}
\mathcal{T}_{\Gamma_T} = \alpha\Delta t\int_{\Gamma_T}(\widetilde{v}_s^{n+\frac{1}{2}\sharp} - \widetilde{v}_f^n)\cdot\widetilde{v}_s^{n+\frac{1}{2}\sharp}\,\mathrm{d}S + \Delta t\int_{\Gamma_T}\widetilde{\lambda}^n\cdot(\widetilde{v}_s^{n+\frac{1}{2}\sharp} - \widetilde{v}_f^{n+1})\,\mathrm{d}S \\
+ \alpha\Delta t\int_{\Gamma_T}(\widetilde{v}_f^{n+1} - \widetilde{v}_s^{n+\frac{1}{2}\sharp})\cdot\widetilde{v}_f^{n+1}\,\mathrm{d}S.
\end{aligned}$$

Splitting $\widetilde{v}_s^{n+\frac{1}{2}\sharp} - \widetilde{v}_f^n$ into $(\widetilde{v}_s^{n+\frac{1}{2}\sharp} - \widetilde{v}_f^{n+1}) + (\widetilde{v}_f^{n+1} - \widetilde{v}_f^n)$, $\mathcal{T}_{\Gamma_T}$ can be recast as

$$\mathcal{T}_{\Gamma_T} = \alpha\Delta t\int_{\Gamma_T}\left|\widetilde{v}_s^{n+\frac{1}{2}\sharp} - \widetilde{v}_f^{n+1}\right|^2 \mathrm{d}S + \alpha\Delta t\int_{\Gamma_T}(\widetilde{v}_f^{n+1} - \widetilde{v}_f^n)\cdot\widetilde{v}_s^{n+\frac{1}{2}\sharp}\,\mathrm{d}S + \Delta t\int_{\Gamma_T}\widetilde{\lambda}^n\cdot(\widetilde{v}_s^{n+\frac{1}{2}\sharp} - \widetilde{v}_f^{n+1})\,\mathrm{d}S$$

Now, since $b = 0$, we know from the key identity (57) that

$$\widetilde{v}_s^{n+\frac{1}{2}\sharp} - \widetilde{v}_f^{n+1} = \frac{1}{\alpha}\big(\widetilde{\lambda}^{n+1} - \widetilde{\lambda}^n\big).$$

Thus

$$\mathcal{T}_{\Gamma_T} = \alpha\Delta t\big\|\widetilde{v}_s^{n+\frac{1}{2}\sharp} - \widetilde{v}_f^{n+1}\big\|_{\Gamma_T}^2 + \alpha\Delta t\int_{\Gamma_T}(\widetilde{v}_f^{n+1} - \widetilde{v}_f^n)\cdot\widetilde{v}_s^{n+\frac{1}{2}\sharp}\,\mathrm{d}S + \frac{\Delta t}{\alpha}\int_{\Gamma_T}\widetilde{\lambda}^n\cdot(\widetilde{\lambda}^{n+1} - \widetilde{\lambda}^n)\,\mathrm{d}S, \tag{60}$$

where we used the notation $\big\|v\big\|_{\Gamma_T}^2 = \int_{\Gamma_T}|v|^2\,\mathrm{d}S$ for the L^2-norm on the boundary. Moreover, we have

$$\frac{\Delta t}{\alpha}\int_{\Gamma_T}\widetilde{\lambda}^n\cdot(\widetilde{\lambda}^{n+1} - \widetilde{\lambda}^n)\,\mathrm{d}S = \frac{\Delta t}{2\alpha}\Big(\big\|\widetilde{\lambda}^{n+1}\big\|_{\Gamma_T}^2 - \big\|\widetilde{\lambda}^n\big\|_{\Gamma_T}^2 - \big\|\widetilde{\lambda}^{n+1} - \widetilde{\lambda}^n\big\|_{\Gamma_T}^2\Big).$$

Using again (57), it follows that

$$\frac{\Delta t}{\alpha}\int_{\Gamma_T}\widetilde{\lambda}^n\cdot(\widetilde{\lambda}^{n+1} - \widetilde{\lambda}^n)\,\mathrm{d}S = \frac{\Delta t}{2\alpha}\Big(\big\|\widetilde{\lambda}^{n+1}\big\|_{\Gamma_T}^2 - \big\|\widetilde{\lambda}^n\big\|_{\Gamma_T}^2\Big) - \frac{\alpha\Delta t}{2}\big\|\widetilde{v}_s^{n+\frac{1}{2}\sharp} - \widetilde{v}_f^{n+1}\big\|_{\Gamma_T}^2. \tag{61}$$

Following [Burman et al., 2022a], to estimate the second term of (60) we use the algebraic identity

$$(a-b)\cdot c = \frac{1}{2}\Big(|a|^2 - |b|^2 - |c-a|^2 + |c-b|^2\Big),$$

which can be seen as a generalization of (24). This identity implies that

$$\alpha\Delta t\int_{\Gamma_T}(\widetilde{v}_f^{n+1} - \widetilde{v}_f^n)\cdot\widetilde{v}_s^{n+\frac{1}{2}\sharp}\,\mathrm{d}S = \frac{\alpha\Delta t}{2}\Big(\big\|\widetilde{v}_f^{n+1}\big\|_{\Gamma_T}^2 - \big\|\widetilde{v}_f^n\big\|_{\Gamma_T}^2 - \big\|\widetilde{v}_s^{n+\frac{1}{2}\sharp} - \widetilde{v}_f^{n+1}\big\|_{\Gamma_T}^2 + \big\|\widetilde{v}_s^{n+\frac{1}{2}\sharp} - \widetilde{v}_f^n\big\|_{\Gamma_T}^2\Big) \tag{62}$$

Collecting (60), (61) and (62), we deduce

$$\begin{aligned}\mathcal{T}_{\Gamma_T} &= \alpha\Delta t\big\|\widetilde{v}_s^{n+\frac{1}{2}\sharp} - \widetilde{v}_f^{n+1}\big\|_{\Gamma_T}^2 + \frac{\Delta t}{2\alpha}\big(\big\|\widetilde{\lambda}^{n+1}\big\|_{\Gamma_T}^2 - \big\|\widetilde{\lambda}^n\big\|_{\Gamma_T}^2\big) - \frac{\alpha\Delta t}{2}\big\|\widetilde{v}_s^{n+\frac{1}{2}\sharp} - \widetilde{v}_f^{n+1}\big\|_{\Gamma_T}^2\\
&\quad + \frac{\alpha\Delta t}{2}\big(\big\|\widetilde{v}_f^{n+1}\big\|_{\Gamma_T}^2 - \big\|\widetilde{v}_f^n\big\|_{\Gamma_T}^2\big) - \frac{\alpha\Delta t}{2}\big\|\widetilde{v}_s^{n+\frac{1}{2}\sharp} - \widetilde{v}_f^{n+1}\big\|_{\Gamma_T}^2 + \frac{\alpha\Delta t}{2}\big\|\widetilde{v}_s^{n+\frac{1}{2}\sharp} - \widetilde{v}_f^n\big\|_{\Gamma_T}^2\\
&= \frac{\Delta t}{2\alpha}\big(\big\|\widetilde{\lambda}^{n+1}\big\|_{\Gamma_T}^2 - \big\|\widetilde{\lambda}^n\big\|_{\Gamma_T}^2\big) + \frac{\alpha\Delta t}{2}\big(\big\|\widetilde{v}_f^{n+1}\big\|_{\Gamma_T}^2 - \big\|\widetilde{v}_f^n\big\|_{\Gamma_T}^2\big) + \frac{\alpha\Delta t}{2}\big\|\widetilde{v}_s^{n+\frac{1}{2}\sharp} - \widetilde{v}_f^n\big\|_{\Gamma_T}^2.\end{aligned}$$

Inserting this expression of $\mathcal{T}_{\Gamma_T}$ in (59) implies

$$\begin{aligned}&(\mathcal{E}^{n+1} - \mathcal{E}^n) + (\mathcal{E}_{\Gamma_T}^{n+1} - \mathcal{E}_{\Gamma_T}^n) + \frac{\alpha\Delta t}{2}\big\|\widetilde{v}_s^{n+\frac{1}{2}\sharp} - \widetilde{v}_f^n\big\|_{\Gamma_T}^2\\
&\quad + \frac{1}{2}\int_\Omega\rho_f\phi\left|\widetilde{v}_f^{n+1} - v_f^n\right|^2\mathrm{d}x + \frac{1}{2}\int_\Omega\rho_s(1-\phi)\left|\widetilde{v}_s^{n+1} - v_s^{n+1}\right|^2\mathrm{d}x + \frac{1}{2}\int_\Omega\rho_f\phi\left|v_f^{n+1} - \widetilde{v}_f^{n+1}\right|^2\mathrm{d}x\\
&\qquad + \Delta t\int_\Omega\phi\,\sigma_f(\widetilde{v}_f^{n+1}) : \varepsilon(\widetilde{v}_f^{n+1})\,\mathrm{d}x + \Delta t\int_\Omega\phi^2 k_f^{-1}\Big(\widetilde{v}_f^{n+1} - \widetilde{v}_s^{n+\frac{1}{2}\sharp}\Big)^2\mathrm{d}x\\
&\qquad\qquad = \Delta t\int_\Omega\phi^2 k_f^{-1}\big(v_f^n - \widetilde{v}_f^{n+1}\big)\cdot\widetilde{v}_s^{n+\frac{1}{2}\sharp}\,\mathrm{d}x,\end{aligned} \tag{63}$$

with

$$\mathcal{E}_{\Gamma_T}^n = \frac{\Delta t}{2\alpha}\big\|\widetilde{\lambda}^n\big\|_{\Gamma_T}^2 + \frac{\alpha\Delta t}{2}\big\|\widetilde{v}_f^n\big\|_{\Gamma_T}^2. \tag{64}$$

The right-hand side of (63) can be bounded as in the proof of Theorem 2.8, and the final estimate (58) follows from discrete Grönwall's lemma after summing (63) between 0 and $N-1$. □

Therefore, the Robin-Robin coupling designed in Scheme 4 furnishes a stable time discretization of the total stress boundary conditions (9). The drawback of the method is that it induces an artificial energy term on the boundary, see (64). To ensure that this additional energy does not pollute the scheme convergence, the Robin coefficient α must be chosen to be large enough, but not too large in view of the term $\frac{\alpha\Delta t}{2}\left\|\widetilde{v}_f^N\right\|_{\Gamma_T}^2$ appearing in the left-hand side of (58). This issue will be explored numerically in Section 4.

Remark 2.16. *In [Burtschell et al., 2017], the authors follow the Robin coupling derived from Nitsche's method in [Astorino et al., 2010]. In our case, such an approach can also be followed however the fluid will be advanced before the solid, contrary to Scheme 4. Following [Astorino et al., 2010], one could show that such Nitsche's approach is stable provided that the time step restriction (28) is fulfilled, that the penalty coefficient γ is large enough – more precisely, $\gamma > 4C_{\text{ie}}$ with C_{ie} a trace-inverse inequality constant – and that $\gamma\mu_f\Delta t = \mathcal{O}(h)$. An advantage of the Robin-Robin coupling presented before compared to a scheme based on Nitsche's method is that it gets rid of the latter condition.*

3 Convergence analysis

In this section, we provide a complete error analysis for the projection scheme proposed previously. To simplify, we will restrict ourselves to the case of homogeneous Dirichlet conditions. Moreover, to avoid the time step condition (28) that happens to be very restrictive for the targeted biomedical applications, we will assume that the permeability is treated implicitly in the prediction step as iin 3. To simplify the analysis and in particular reuse the discrete projector built in [Barré et al., 2023b] thanks to a T-coercivity approach, the solid will be discretized using a backward Euler scheme. The scheme for which we are going to perform the convergence analysis is summarized in Scheme 5 with, again, the convention

$$i = \begin{cases} 0 & \text{for the non-incremental version of the scheme,} \\ 1 & \text{for the incremental version of the scheme.} \end{cases}$$

Scheme 5 is almost similar to 3, the only difference being the discretization of the solid part that induces numerical dissipation.

Scheme 5 Implicit treatment of permeability and full backward Euler approach

---

Step 1: `(prediction step)`
Find u_s^{n+1}, $\widetilde{v}_s^{n+1}$ and $\widetilde{v}_f^{n+1}$ such that $u_s^{n+1}|_{\Gamma_D} = \widetilde{v}_s^{n+1}|_{\Gamma_D} = \widetilde{v}_f^{n+1}|_{\Gamma_D} = 0$ and

$$\begin{cases} \rho_s(1-\phi)\dfrac{\widetilde{v}_s^{n+1} - v_s^n}{\Delta t} - \operatorname{div}\left(\sigma_s(u_s^{n+1})\right) \\ \qquad\qquad - \phi^2 k_f^{-1}\left(\widetilde{v}_f^{n+1} - \widetilde{v}_s^{n+1}\right) + i(1-\phi)\nabla p^n = \rho_s(1-\phi) f^{n+1}, \\ \rho_f\phi\dfrac{\widetilde{v}_f^{n+1} - v_f^n}{\Delta t} - \operatorname{div}\left(\phi\,\sigma_f(\widetilde{v}_f^{n+1})\right) \\ \qquad\qquad + \phi^2 k_f^{-1}\left(\widetilde{v}_f^{n+1} - \widetilde{v}_s^{n+1}\right) + i\phi\,\nabla p^n = \rho_f\phi\, f^{n+1}, \\ \dfrac{u_s^{n+1} - u_s^n}{\Delta t} = \widetilde{v}_s^{n+1}. \end{cases}$$

Step 2: `(correction step)`

Find v_s^{n+1}, v_f^{n+1} and p^{n+1} such that $\int_\Omega p^{n+1}\,\mathrm{d}x = 0$ and

$$\begin{cases} \rho_s(1-\phi)\dfrac{v_s^{n+1}-\widetilde{v}_s^{n+1}}{\Delta t} + (1-\phi)\,\nabla(p^{n+1}-ip^n) = 0, \\ \rho_f\phi\dfrac{v_f^{n+1}-\widetilde{v}_f^{n+1}}{\Delta t} + \phi\,\nabla(p^{n+1}-ip^n) = 0, \\ \operatorname{div}\big((1-\phi)v_s^{n+1} + \phi\, v_f^{n+1}\big) = 0, \\ \big((1-\phi)v_s^{n+1} + \phi\, v_f^{n+1}\big)\cdot n|_{\Gamma_D} = 0. \end{cases}$$

Remark 3.1. *The correction step at time t^n implies the following equalities*

$$\frac{\rho_s(1-\phi)}{\Delta t}v_s^n = \frac{\rho_s(1-\phi)}{\Delta t}\widetilde{v}_s^n - (1-\phi)\,\nabla(p^n - ip^{n-1}) \quad \textit{and} \quad \frac{\rho_f\phi}{\Delta t}v_f^n = \frac{\rho_f\phi}{\Delta t}\widetilde{v}_f^n - \phi\,\nabla(p^n - ip^{n-1}).$$

These relations can be used to totally eliminate the end-of-step velocities v_s^n and v_f^n from the prediction step, leading to

$$\begin{cases} \rho_s(1-\phi)\dfrac{\widetilde{v}_s^{n+1}-\widetilde{v}_s^n}{\Delta t} - \operatorname{div}\big(\sigma_s(u_s^{n+1})\big) \\ \qquad\qquad - \phi^2 k_f^{-1}\big(\widetilde{v}_f^{n+1}-\widetilde{v}_s^{n+1}\big) + (1-\phi)\nabla\big(p^n + i(p^n-p^{n-1})\big) = \rho_s(1-\phi)f^{n+1}, \\ \rho_f\phi\dfrac{\widetilde{v}_f^{n+1}-\widetilde{v}_f^n}{\Delta t} - \operatorname{div}\big(\phi\,\sigma_f(\widetilde{v}_f^{n+1})\big) \\ \qquad\qquad + \phi^2 k_f^{-1}\big(\widetilde{v}_f^{n+1}-\widetilde{v}_s^{n+1}\big) + \phi\,\nabla\big(p^n + i(p^n-p^{n-1})\big) = \rho_f\phi\, f^{n+1}, \\ \dfrac{u_s^{n+1}-u_s^n}{\Delta t} = \widetilde{v}_s^{n+1}. \end{cases} \tag{65}$$

Furthermore, the mixture divergence constraint yields

$$\operatorname{div}\big((1-\phi)\widetilde{v}_s^{n+1} + \phi\,\widetilde{v}_f^{n+1}\big) - \Delta t\operatorname{div}\Big(\rho_{\text{eff}}^{-1}\nabla(p^{n+1}-ip^n)\Big) = 0. \tag{66}$$

From (65) and (66), we see that Scheme 5 can be interpreted as a penalized version of the monolithic scheme, in which the pressure gradient is treated explicitly. At the continuous level, this corresponds to penalizing the incompressibility constraint of Problem (3) as follows:

$$\operatorname{div}\big((1-\phi)v_s + \phi\, v_f\big) - \varepsilon\operatorname{div}\big(\rho_{\text{eff}}^{-1}\nabla p\big) = 0 \quad \textit{if } i=0, \ \textit{with } \varepsilon = \Delta t,$$

and

$$\operatorname{div}\big((1-\phi)v_s + \phi\, v_f\big) - \varepsilon\operatorname{div}\big(\rho_{\text{eff}}^{-1}\nabla\partial_t p\big) = 0 \quad \textit{if } i=1, \ \textit{with } \varepsilon = \Delta t^2.$$

The value of the penalty parameter ε gives us a first intuition of the time convergence order of the scheme in non-incremental and incremental versions, that will be justified theoretically in what follows.

The section is organized as follows. First, we will give the discrete setting associated with the spatial discretization of Scheme 5. Then, we derive the error equations between the continuous solution and the fully discrete solution of the scheme. The error system is established simultaneously for the non-incremental and incremental versions. Lastly, the final error analysis will be presented separately for the case $i = 0$ and $i = 1$.

3.1 Total discretization

As mentioned in (16), the projection scheme is consistent with the monolithic scheme (10) studied in [Barré et al., 2023b]. Consequently, we globally use the same spatial discretization than the one proposed in [Barré et al., 2023b] and we adopt similar notations: we consider conforming approximations X_h and Q_h of the spaces $[\mathrm{H}^1_0(\Omega)]^d$ and $\mathrm{L}^2_0(\Omega)$. Moreover, we assume that the discrete inf-sup condition

$$\exists \beta > 0, \forall p_h \in Q_h, \quad \sup_{v_h \in X_h} \frac{\displaystyle\int_\Omega \operatorname{div} v_h \, p_h \, \mathrm{d}x}{\|v_h\|_{[\mathrm{H}^1_0(\Omega)]^d}} \geq \beta \|p_h\|. \tag{67}$$

is satisfied. Note that one might be tempted to use standard finite elements that do not satisfy the inf-sup condition since Scheme 5 does not require to solve any saddle-point problem, neither in the prediction step nor in the correction step that can be formulated as a Poisson problem, see (14). However, we will numerically illustrate in Section 4 that the inf-sup condition (67) is fundamental to retrieve a correct approximation of the pressure field, as it has been shown in the case of projection schemes for incompressible fluids [Guermond and Quartapelle, 1998]. This condition can be dropped only if the time step is large enough, or by using stabilization techniques as it is done for instance in [Markert et al., 2009].

In order to solve the correction step as a Poisson problem for the pressure, we assume in addition that the discrete pressure space Q_h is a conforming approximation of the space $\mathrm{H}^1(\Omega)$. This is the case for many of the finite elements satisfying (67), such as the Taylor-Hood or MINI elements. Assuming to simplify that $f_h^{n+1} = f(t^{n+1})$, the fully discrete formulation of Scheme 5 then reads

Step 1: `(prediction step)`
Find $u_{s,h}^{n+1} \in X_h$, $\widetilde{v}_{s,h}^{n+1} \in X_h$ and $\widetilde{v}_{f,h}^{n+1} \in X_h$ such that, for any $w_{s,h} \in X_h$, $d_{s,h} \in X_h$ and $w_{f,h} \in X_h$,

$$\begin{aligned}
&\int_\Omega \sigma_s\Big(\frac{u_{s,h}^{n+1} - u_{s,h}^n}{\Delta t}\Big) : \varepsilon(d_{s,h}) \, \mathrm{d}x + \int_\Omega \rho_s(1-\phi) \frac{\widetilde{v}_{s,h}^{n+1} - v_{s,h}^n}{\Delta t} \cdot w_{s,h} \, \mathrm{d}x \\
&\quad + \int_\Omega \rho_f \phi \frac{\widetilde{v}_{f,h}^{n+1} - v_{f,h}^n}{\Delta t} \cdot w_{f,h} \, \mathrm{d}x - \int_\Omega \sigma_s(\widetilde{v}_{s,h}^{n+1}) : \varepsilon(d_{s,h}) \, \mathrm{d}x + \int_\Omega \sigma_s(u_{s,h}^{n+1}) : \varepsilon(w_{s,h}) \, \mathrm{d}x \\
&\quad + \int_\Omega \phi \, \sigma_f(\widetilde{v}_{f,h}^{n+1}) : \varepsilon(w_{f,h}) \, \mathrm{d}x + \int_\Omega \phi^2 k_f^{-1} (\widetilde{v}_{f,h}^{n+1} - \widetilde{v}_{s,h}^{n+1}) \cdot (w_{f,h} - w_{s,h}) \, \mathrm{d}x \\
&\quad + i \int_\Omega (1-\phi) \nabla p_h^n \cdot w_{s,h} \, \mathrm{d}x + i \int_\Omega \phi \, \nabla p_h^n \cdot w_{f,h} \, \mathrm{d}x \\
&\quad = \int_\Omega \rho_s(1-\phi) \, f(t^{n+1}) \cdot w_{s,h} \, \mathrm{d}x + \int_\Omega \rho_f \phi \, f(t^{n+1}) \cdot w_{f,h} \, \mathrm{d}x.
\end{aligned} \tag{68}$$

Step 2: `(correction step)`
Find $v_{s,h}^{n+1} \in Y_{s,h}$, $v_{f,h}^{n+1} \in Y_{f,h}$ and $p_h^{n+1} \in Q_h$ such that, for any $w_{s,h} \in Y_{s,h}$, $w_{f,h} \in Y_{f,h}$ and $q_h \in Q_h$,

$$\begin{aligned}
&\int_\Omega \rho_s(1-\phi) \frac{v_{s,h}^{n+1} - \widetilde{v}_{s,h}^{n+1}}{\Delta t} \cdot w_{s,h} \, \mathrm{d}x + \int_\Omega \rho_f \phi \frac{v_{f,h}^{n+1} - \widetilde{v}_{f,h}^{n+1}}{\Delta t} \cdot w_{f,h} \, \mathrm{d}x \\
&\quad + \int_\Omega (1-\phi) \nabla (p_h^{n+1} - i p_h^n) \cdot w_{s,h} \, \mathrm{d}x + \int_\Omega \phi \, \nabla (p_h^{n+1} - i p_h^n) \cdot w_{f,h} \, \mathrm{d}x \\
&\quad - \int_\Omega (1-\phi) v_{s,h}^{n+1} \cdot \nabla q_h \, \mathrm{d}x - \int_\Omega \phi \, v_{f,h}^{n+1} \cdot \nabla q_h \, \mathrm{d}x = 0,
\end{aligned} \tag{69}$$

where the discrete spaces

$$Y_{s,h} = X_h + (1-\phi)\nabla Q_h \quad \text{and} \quad Y_{f,h} = X_h + \phi \nabla Q_h,$$

are conforming approximations of $[\mathrm{L}^2(\Omega)]^d$ since $Q_h \subset \mathrm{H}^1(\Omega)$.

3.2 Error system

To derive the equations satisfied by the error between the fully discrete solution of (68) – (69) and the continuous solution of (3), we are first going to project the continuous solution on the discrete space $X_h \times X_h \times X_h \times Q_h$. To do so, we use the shifted Riesz projector P_h introduced in [Barré et al., 2023b] for the analysis of the monolithic scheme (10). The main feature of this projector is that it is adapted to the bilinear form involved in the system, so that it generates few residual terms despite the hyperbolic – parabolic coupling and the saddle-point structure of the problem.

Let us denote by $u_{s,h}(t^n)$, $v_{s,h}(t^n)$, $v_{f,h}(t^n)$ and $p_h(t^n)$ the projections on the discrete spaces of the continuous solution at time t^n using this projector, namely $\big(u_{s,h}(t^n), v_{s,h}(t^n), v_{f,h}(t^n), p_h(t^n)\big) = P_h\big(u_s(t^n), v_s(t^n), v_f(t^n), p(t^n)\big)$. Provided that the continuous solution is regular enough, we know from [Barré et al., 2023b, estimates (42) and (43)] that

$$\Big\|\big(u_s(t^n), v_s(t^n), v_f(t^n), p(t^n)\big) - \big(u_{s,h}(t^n), v_{s,h}(t^n), v_{f,h}(t^n), p_h(t^n)\big)\Big\|_Z \leq C(h^\ell + h^r), \tag{70}$$

where the constant $C > 0$ depends on the continuous solution, the convergence orders ℓ and $r \leq \ell$ depend on the choice of the discrete spaces X_h and Q_h, and $Z = [\mathrm{H}^1_0(\Omega)]^d \times [\mathrm{L}^2(\Omega)]^d \times [\mathrm{L}^2(\Omega)]^d \times \mathrm{L}^2(\Omega)$. In particular, (70) implies that it is sufficient to study the error between the projection of the continuous solution and the fully discrete solution since

$$\begin{aligned}
&\Big\|\big(u_s(t^n), v_s(t^n), v_f(t^n), p(t^n)\big) - \big(u^n_{s,h}, v^n_{s,h}, v^n_{f,h}, p^n_h\big)\Big\|_Z \\
&\qquad \leq \Big\|\big(u_s(t^n), v_s(t^n), v_f(t^n), p(t^n)\big) - \big(u_{s,h}(t^n), v_{s,h}(t^n), v_{f,h}(t^n), p_h(t^n)\big)\Big\|_Z \\
&\qquad\qquad + \Big\|\big(u_{s,h}(t^n), v_{s,h}(t^n), v_{f,h}(t^n), p_h(t^n)\big) - \big(u^n_{s,h}, v^n_{s,h}, v^n_{f,h}, p^n_h\big)\Big\|_Z.
\end{aligned}$$

To that end, we introduce the discrete errors

$$\begin{aligned}
e^n_{u,h} &= u_{s,h}(t^n) - u^n_{s,h}, \qquad & \delta^n_h &= p_h(t^n) - p^n_h, \\
\widetilde{e}^n_{s,h} &= v_{s,h}(t^n) - \widetilde{v}^n_{s,h}, \qquad & e^n_{s,h} &= v_{s,h}(t^n) - v^n_{s,h}, \\
\widetilde{e}^n_{f,h} &= v_{f,h}(t^n) - \widetilde{v}^n_{f,h}, \qquad & e^n_{s,h} &= v_{f,h}(t^n) - v^n_{f,h}.
\end{aligned} \tag{71}$$

As in [Barré et al., 2023b, equation (50)], we get that the P_h-projection of the solution satisfies

$$\begin{aligned}
&\int_\Omega \sigma_s\Big(\frac{u_{s,h}(t^{n+1}) - u_{s,h}(t^n)}{\Delta t}\Big) : \varepsilon(d_{s,h})\,\mathrm{d}x \\
&\qquad + \int_\Omega \rho_s(1-\phi)\frac{v_{s,h}(t^{n+1}) - v_{s,h}(t^n)}{\Delta t}\cdot w_{s,h}\,\mathrm{d}x + \int_\Omega \rho_f\phi\frac{v_{f,h}(t^{n+1}) - v_{f,h}(t^n)}{\Delta t}\cdot w_{f,h}\,\mathrm{d}x \\
&\qquad\qquad - \int_\Omega \sigma_s\big(v_{s,h}(t^{n+1})\big) : \varepsilon(d_{s,h})\,\mathrm{d}x + \int_\Omega \sigma_s\big(u_{s,h}(t^{n+1})\big) : \varepsilon(w_{s,h})\,\mathrm{d}x \\
&\qquad + \int_\Omega \phi\,\sigma_f\big(v_{f,h}(t^{n+1})\big) : \varepsilon(w_{f,h})\,\mathrm{d}x + \int_\Omega \phi^2 k_f^{-1}\big(v_{f,h}(t^{n+1}) - v_{s,h}(t^{n+1})\big)\cdot(w_{f,h} - w_{s,h})\,\mathrm{d}x \\
&\qquad\qquad + \int_\Omega (1-\phi)\nabla p_h(t^{n+1})\cdot w_{s,h}\,\mathrm{d}x + \int_\Omega \phi\,\nabla p_h(t^{n+1})\cdot w_{f,h}\,\mathrm{d}x \\
&\qquad\qquad - \int_\Omega (1-\phi)v_{s,h}(t^{n+1})\cdot\nabla q_h\,\mathrm{d}x - \int_\Omega \phi\,v_{f,h}(t^{n+1})\cdot\nabla q_h\,\mathrm{d}x \\
&\qquad = \int_\Omega \sigma_s\big(R^{n+1}_{u,h}\big) : \varepsilon(d_{s,h})\,\mathrm{d}x + \int_\Omega \rho_s(1-\phi)R^{n+1}_{s,h}\cdot w_{s,h}\,\mathrm{d}x + \int_\Omega \rho_f\phi\,R^{n+1}_{f,h}\cdot w_{f,h}\,\mathrm{d}x \\
&\qquad\qquad + \int_\Omega \rho_s(1-\phi)\,f(t^{n+1})\cdot w_{s,h}\,\mathrm{d}x + \int_\Omega \rho_f\phi\,f(t^{n+1})\cdot w_{f,h}\,\mathrm{d}x,
\end{aligned} \tag{72}$$

for any $w_{s,h} \in X_h$, $d_{s,h} \in X_h$, $w_{f,h} \in X_h$ and $q_h \in Q_h$, where $R_{u,h}^{n+1}$, $R_{s,h}^{n+1}$ and $R_{f,h}^{n+1}$ are space and time consistency terms satisfying

$$\int_\Omega \sigma_s\big(R_{u,h}^{n+1}\big) : \varepsilon\big(R_{u,h}^{n+1}\big)\,\mathrm{d}x + \int_\Omega \rho_s(1-\phi)\left|R_{s,h}^{n+1}\right|^2 \mathrm{d}x + \int_\Omega \rho_f\phi\left|R_{f,h}^{n+1}\right|^2 \mathrm{d}x \le C(\Delta t + h^\ell + h^r)^2, \tag{73}$$

see [Barré et al., 2023b, estimates (54), (55) and (56)].

We are now ready to derive the equations satisfied by the errors defined in (71). Substracting the discrete prediction step (68) from (72) with $q_h = 0$, we obtain

$$\begin{aligned}
&\int_\Omega \sigma_s\Big(\frac{e_{u,h}^{n+1} - e_{u,h}^{n}}{\Delta t}\Big) : \varepsilon(d_{s,h})\,\mathrm{d}x \\
&\qquad + \int_\Omega \rho_s(1-\phi)\frac{\widetilde{e}_{s,h}^{n+1} - e_{s,h}^{n}}{\Delta t}\cdot w_{s,h}\,\mathrm{d}x + \int_\Omega \rho_f\phi\frac{\widetilde{e}_{f,h}^{n+1} - e_{f,h}^{n}}{\Delta t}\cdot w_{f,h}\,\mathrm{d}x \\
&\qquad\quad - \int_\Omega \sigma_s\big(\widetilde{e}_{s,h}^{n+1}\big) : \varepsilon(d_{s,h})\,\mathrm{d}x + \int_\Omega \sigma_s\big(e_{u,h}^{n+1}\big) : \varepsilon(w_{s,h})\,\mathrm{d}x \\
&\quad + \int_\Omega \phi\,\sigma_f\big(\widetilde{e}_{f,h}^{n+1}\big) : \varepsilon(w_{f,h})\,\mathrm{d}x + \int_\Omega \phi^2 k_f^{-1}\big(\widetilde{e}_{f,h}^{n+1} - \widetilde{e}_{s,h}^{n+1}\big)\cdot(w_{f,h} - w_{s,h})\,\mathrm{d}x \\
&\quad + \int_\Omega (1-\phi)\nabla\big(p_h(t^{n+1}) - ip_h^n\big)\cdot w_{s,h}\,\mathrm{d}x + \int_\Omega \phi\,\nabla\big(p_h(t^{n+1}) - ip_h^n\big)\cdot w_{f,h}\,\mathrm{d}x \\
&\qquad = \int_\Omega \sigma_s\big(R_{u,h}^{n+1}\big) : \varepsilon(d_{s,h})\,\mathrm{d}x + \int_\Omega \rho_s(1-\phi)R_{s,h}^{n+1}\cdot w_{s,h}\,\mathrm{d}x + \int_\Omega \rho_f\phi\,R_{f,h}^{n+1}\cdot w_{f,h}\,\mathrm{d}x,
\end{aligned} \tag{74}$$

for any $w_{s,h} \in X_h$, $d_{s,h} \in X_h$ and $w_{f,h} \in X_h$. For the correction step, we write

$$v_{s,h}^{n+1} - \widetilde{v}_{s,h}^{n+1} = v_{s,h}^{n+1} - v_{s,h}(t^{n+1}) + v_{s,h}(t^{n+1}) - \widetilde{v}_{s,h}^{n+1} = \widetilde{e}_{s,h}^{n+1} - e_{s,h}^{n+1},$$

and in the same way $v_{f,h}^{n+1} - \widetilde{v}_{f,h}^{n+1} = \widetilde{e}_{f,h}^{n+1} - e_{f,h}^{n+1}$. Moreover, since

$$-\int_\Omega (1-\phi)v_{s,h}(t^{n+1})\cdot\nabla q_h\,\mathrm{d}x - \int_\Omega \phi\,v_{f,h}(t^{n+1})\cdot\nabla q_h\,\mathrm{d}x = 0, \quad \forall q_h \in Q_h,$$

and

$$-\int_\Omega (1-\phi)v_{s,h}^{n+1}\cdot\nabla q_h\,\mathrm{d}x - \int_\Omega \phi\,v_{f,h}^{n+1}\cdot\nabla q_h\,\mathrm{d}x = 0, \quad \forall q_h \in Q_h,$$

we also have

$$-\int_\Omega (1-\phi)e_{s,h}^{n+1}\cdot\nabla q_h\,\mathrm{d}x - \int_\Omega \phi\,e_{f,h}^{n+1}\cdot\nabla q_h\,\mathrm{d}x = 0, \quad \forall q_h \in Q_h.$$

Incorporating these relations into (69), we get

$$\begin{aligned}
&\int_\Omega \rho_s(1-\phi)\frac{e_{s,h}^{n+1} - \widetilde{e}_{s,h}^{n+1}}{\Delta t}\cdot w_{s,h}\,\mathrm{d}x + \int_\Omega \rho_f\phi\frac{e_{f,h}^{n+1} - \widetilde{e}_{f,h}^{n+1}}{\Delta t}\cdot w_{f,h}\,\mathrm{d}x \\
&\qquad + \int_\Omega (1-\phi)\nabla(ip_h^n - p_h^{n+1})\cdot w_{s,h}\,\mathrm{d}x + \int_\Omega \phi\,\nabla(ip_h^n - p_h^{n+1})\cdot w_{f,h}\,\mathrm{d}x \\
&\qquad\qquad - \int_\Omega (1-\phi)e_{s,h}^{n+1}\cdot\nabla q_h\,\mathrm{d}x - \int_\Omega \phi\,e_{f,h}^{n+1}\cdot\nabla q_h\,\mathrm{d}x = 0,
\end{aligned} \tag{75}$$

for any $w_{s,h} \in Y_{s,h}$, $w_{f,h} \in Y_{f,h}$ and $q_h \in Q_h$. The pressure residuals multiplying the test functions $(1-\phi)w_{s,h}$ and $\phi\,w_{f,h}$ in (74) and (75), namely the terms $p_h(t^{n+1}) - ip_h^n$ and $ip_h^n - p_h^{n+1}$, play a key role in the time convergence rate of the scheme, as we will see in the following error analysis.

3.3 Error analysis

The error analysis hinges on the discrete energy balances derived previously. Let us define the energy associated with the errors (71) by

$$E_h^n = \frac{1}{2}\int_\Omega \sigma_s(e_{u,h}^n) : \varepsilon(e_{u,h}^n)\,\mathrm{d}x + \frac{1}{2}\int_\Omega \rho_s(1-\phi)\,\left|e_{s,h}^n\right|^2\,\mathrm{d}x + \frac{1}{2}\int_\Omega \rho_f\phi\,\left|e_{f,h}^n\right|^2\,\mathrm{d}x.$$

The convergence of Scheme 5 in the non-incremental case is stated in Theorem 3.2 below, which is the main result of this section.

Theorem 3.2. *Assume that $i = 0$ and that the solution of Problem (3) is regular enough, in particular that $p \in \mathrm{L}^2(0,T;\mathrm{H}^1(\Omega))$. If $\Delta t < 1$ and if the initialization of Scheme 5 is such that*

$$E_h^0 \le C(h^\ell + h^r)^2, \tag{76}$$

then for any $0 \le N \le n_T$, it holds

$$\begin{aligned}
E_h^N &+ \frac{1}{2}\sum_{n=0}^{N-1}\int_\Omega \sigma_s(e_{u,h}^{n+1}-e_{u,h}^n) : \varepsilon(e_{u,h}^{n+1}-e_{u,h}^n)\,\mathrm{d}x + \frac{1}{4}\sum_{n=0}^{N-1}\int_\Omega \rho_s(1-\phi)\left|\widetilde{e}_{s,h}^{n+1}-e_{s,h}^n\right|^2\mathrm{d}x \\
&+ \frac{1}{2}\sum_{n=0}^{N-1}\int_\Omega \rho_f\phi\left|\widetilde{e}_{f,h}^{n+1}-e_{f,h}^n\right|^2\mathrm{d}x + \frac{1}{4}\sum_{n=0}^{N-1}\int_\Omega \rho_s(1-\phi)\left|e_{s,h}^{n+1}-\widetilde{e}_{s,h}^{n+1}\right|^2\mathrm{d}x \\
&+ \frac{1}{4}\sum_{n=0}^{N-1}\int_\Omega \rho_f\phi\left|e_{f,h}^{n+1}-\widetilde{e}_{f,h}^{n+1}\right|^2\mathrm{d}x + \frac{\Delta t}{2}\sum_{n=0}^{N-1}\int_\Omega \phi\,\sigma_f(\widetilde{e}_{f,h}^{n+1}) : \varepsilon(\widetilde{e}_{f,h}^{n+1})\,\mathrm{d}x \\
&+ \Delta t\sum_{n=0}^{N-1}\int_\Omega \phi^2 k_f^{-1}\left(\widetilde{e}_{f,h}^{n+1}-\widetilde{e}_{s,h}^{n+1}\right)^2\mathrm{d}x \le C(h^\ell+h^r)^2 + C\Delta t,
\end{aligned} \tag{77}$$

with C a constant independent of h that behaves like $\exp(1/(1-\Delta t))$.

Proof. As in the stability analysis – see (47) – we consider the test functions $w_{s,h} = \Delta t\,\widetilde{e}_{s,h}^{n+1}$, $d_{s,h} = \Delta t\,e_{u,h}^{n+1}$, $w_{f,h} = \Delta t\,\widetilde{e}_{f,h}^{n+1}$ in the error prediction step (74), and $w_{s,h} = \Delta t\,e_{s,h}^{n+1}$, $w_{f,h} = \Delta t\,e_{f,h}^{n+1}$, $q_h = \Delta t\,\delta_h^{n+1}$ in the error correction step (75), leading to

$$\begin{aligned}
(E_h^{n+1}-E_h^n) &+ \frac{1}{2}\int_\Omega \sigma_s(e_{u,h}^{n+1}-e_{u,h}^n) : \varepsilon(e_{u,h}^{n+1}-e_{u,h}^n)\,\mathrm{d}x + \frac{1}{2}\int_\Omega \rho_s(1-\phi)\left|\widetilde{e}_{s,h}^{n+1}-e_{s,h}^n\right|^2\mathrm{d}x \\
&+ \frac{1}{2}\int_\Omega \rho_f\phi\left|\widetilde{e}_{f,h}^{n+1}-e_{f,h}^n\right|^2\mathrm{d}x + \frac{1}{2}\int_\Omega \rho_s(1-\phi)\left|e_{s,h}^{n+1}-\widetilde{e}_{s,h}^{n+1}\right|^2\mathrm{d}x + \frac{1}{2}\int_\Omega \rho_f\phi\left|e_{f,h}^{n+1}-\widetilde{e}_{f,h}^{n+1}\right|^2\mathrm{d}x \\
&+ \Delta t\int_\Omega \phi\,\sigma_f(\widetilde{e}_{f,h}^{n+1}) : \varepsilon(\widetilde{e}_{f,h}^{n+1})\,\mathrm{d}x + \Delta t\int_\Omega \phi^2 k_f^{-1}\left(\widetilde{e}_{f,h}^{n+1}-\widetilde{e}_{s,h}^{n+1}\right)^2\mathrm{d}x \\
&= \mathcal{T}_p^{n+1} + \mathcal{T}_u^{n+1} + \mathcal{T}_s^{n+1} + \mathcal{T}_f^{n+1},
\end{aligned} \tag{78}$$

with the residual terms

$$\begin{aligned}
\mathcal{T}_p^{n+1} = &-\Delta t\int_\Omega (1-\phi)\nabla p_h(t^{n+1})\cdot\widetilde{e}_{s,h}^{n+1}\,\mathrm{d}x - \Delta t\int_\Omega \phi\,\nabla p_h(t^{n+1})\cdot\widetilde{e}_{f,h}^{n+1}\,\mathrm{d}x \\
&+ \Delta t\int_\Omega (1-\phi)\nabla p_h^{n+1}\cdot e_{s,h}^{n+1}\,\mathrm{d}x + \Delta t\int_\Omega \phi\,\nabla p_h^{n+1}\cdot e_{f,h}^{n+1}\,\mathrm{d}x \\
&+ \Delta t\int_\Omega (1-\phi)\nabla\delta_h^{n+1}\cdot e_{s,h}^{n+1}\,\mathrm{d}x + \Delta t\int_\Omega \phi\,\nabla\delta_h^{n+1}\cdot e_{f,h}^{n+1}\,\mathrm{d}x,
\end{aligned}$$

and

$$\mathcal{T}_u^{n+1} = \Delta t \int_\Omega \sigma_s\big(R_{u,h}^{n+1}\big) : \varepsilon(e_{u,h}^{n+1})\,\mathrm{d}x,$$
$$\mathcal{T}_s^{n+1} = \Delta t \int_\Omega \rho_s(1-\phi) R_{s,h}^{n+1} \cdot \widetilde{e}_{s,h}^{n+1}\,\mathrm{d}x,$$
$$\mathcal{T}_f^{n+1} = \Delta t \int_\Omega \rho_f \phi\, R_{f,h}^{n+1} \cdot \widetilde{e}_{f,h}^{n+1}\,\mathrm{d}x.$$

Let us start by estimating the pressure residual term $\mathcal{T}_p^{n+1}$. Since $p_h^{n+1} = p_h(t^{n+1}) - \delta_h^{n+1}$, the terms of the form $(1-\phi)\nabla\delta_h^{n+1}\cdot e_{s,h}^{n+1}$ and $\phi\,\nabla\delta_h^{n+1}\cdot e_{f,h}^{n+1}$ cancel out, so that

$$\begin{aligned}\mathcal{T}_p^{n+1} &= \Delta t \int_\Omega p_h(t^{n+1})\,\mathrm{div}\left((1-\phi)\widetilde{e}_{s,h}^{n+1} + \phi\,\widetilde{e}_{f,h}^{n+1}\right)\mathrm{d}x - \Delta t \int_\Omega p_h(t^{n+1})\,\mathrm{div}\left((1-\phi)e_{s,h}^{n+1} + \phi\, e_{f,h}^{n+1}\right)\mathrm{d}x\\ &= -\Delta t \int_\Omega (1-\phi)\nabla p_h(t^{n+1})\cdot(\widetilde{e}_{s,h}^{n+1} - e_{s,h}^{n+1})\,\mathrm{d}x - \Delta t\int_\Omega \phi\,\nabla p_h(t^{n+1})\cdot(\widetilde{e}_{f,h}^{n+1} - e_{f,h}^{n+1})\,\mathrm{d}x.\end{aligned}$$

These two terms can then be controled using the numerical dissipation coming from the correction step. Indeed, Young inequality implies that, $\forall \gamma_1 > 0$,

$$\begin{aligned}-\Delta t \int_\Omega (1-\phi)\nabla p_h(t^{n+1})\cdot(\widetilde{e}_{s,h}^{n+1} - e_{s,h}^{n+1})\,\mathrm{d}x \le \frac{\gamma_1}{2}\int_\Omega \rho_s(1-\phi)\left|\widetilde{e}_{s,h}^{n+1} - e_{s,h}^{n+1}\right|^2\mathrm{d}x\\ + \frac{\Delta t^2}{2\gamma_1\rho_s}\int_\Omega (1-\phi)\left|\nabla p_h(t^{n+1})\right|^2\mathrm{d}x.\end{aligned}$$

Handling the fluid term in the same way, it follows that

$$\mathcal{T}_p^{n+1} \le \frac{\gamma_1}{2}\int_\Omega \rho_s(1-\phi)\left|\widetilde{e}_{s,h}^{n+1} - e_{s,h}^{n+1}\right|^2\mathrm{d}x + \frac{\gamma_2}{2}\int_\Omega \rho_f\phi\left|\widetilde{e}_{f,h}^{n+1} - e_{f,h}^{n+1}\right|^2\mathrm{d}x + C\Delta t^2\left\|\nabla p_h(t^{n+1})\right\|^2, \quad (79)$$

where $\gamma_2 > 0$ and C is a positive constant depending only on γ_1, γ_2, ρ_s, ρ_f and ϕ.

For the displacement residual term $\mathcal{T}_u^{n+1}$, in virtue of the consistency estimate (73), we have

$$\begin{aligned}\mathcal{T}_u^{n+1} &\le \frac{\Delta t}{2}\int_\Omega \sigma_s\big(R_{u,h}^{n+1}\big) : \varepsilon(R_{u,h}^{n+1})\,\mathrm{d}x + \frac{\Delta t}{2}\int_\Omega \sigma_s\big(e_{u,h}^{n+1}\big) : \varepsilon(e_{u,h}^{n+1})\,\mathrm{d}x\\ &\le C\Delta t(\Delta t + h^\ell + h^r)^2 + \Delta t E_h^{n+1}. \quad (80)\end{aligned}$$

Then, the fluid residual term $\mathcal{T}_f^{n+1}$ is controled thanks to the fluid viscous dissipation by using Young inequality together with Korn inequality as follows:

$$\begin{aligned}\mathcal{T}_f^{n+1} &\le \gamma_3\Delta t\int_\Omega \phi\,\sigma_f(\widetilde{e}_{f,h}^{n+1}) : \varepsilon(\widetilde{e}_{f,h}^{n+1})\,\mathrm{d}x + C\Delta t\int_\Omega \rho_f\phi\left|R_{f,h}^{n+1}\right|^2\mathrm{d}x\\ &\le \gamma_3\Delta t\int_\Omega \phi\,\sigma_f(\widetilde{e}_{f,h}^{n+1}) : \varepsilon(\widetilde{e}_{f,h}^{n+1})\,\mathrm{d}x + C\Delta t(\Delta t + h^\ell + h^r)^2, \quad (81)\end{aligned}$$

with $\gamma_3 > 0$ and C a positive constant depending on γ_3, μ_f, ϕ and Ω. Finally, let us consider the solid residual term $\mathcal{T}_s^{n+1}$, which we decompose as

$$\mathcal{T}_s^{n+1} = \Delta t\int_\Omega \rho_s(1-\phi)R_{s,h}^{n+1}\cdot(\widetilde{e}_{s,h}^{n+1} - e_{s,h}^n)\,\mathrm{d}x + \Delta t\int_\Omega \rho_s(1-\phi)R_{s,h}^{n+1}\cdot e_{s,h}^n\,\mathrm{d}x.$$

The first term is controled with the help of the solid numerical dissipation by writing, $\forall\gamma_4 > 0$,

$$\begin{aligned}\Delta t\int_\Omega \rho_s(1-\phi)R_{s,h}^{n+1}\cdot(\widetilde{e}_{s,h}^{n+1} - e_{s,h}^n)\,\mathrm{d}x \le \frac{\gamma_4}{2}\int_\Omega \rho_s(1-\phi)\left|\widetilde{e}_{s,h}^{n+1} - e_{s,h}^n\right|^2\mathrm{d}x\\ + \frac{\Delta t^2}{2\gamma_4}\int_\Omega \rho_s(1-\phi)\left|R_{s,h}^{n+1}\right|^2\mathrm{d}x,\end{aligned}$$

and the second term is controled as in (80), which results in

$$\Delta t \int_\Omega \rho_s(1-\phi) R_{s,h}^{n+1} \cdot e_{s,h}^n \,\mathrm{d}x \le \frac{\Delta t}{2} \int_\Omega \rho_s(1-\phi) \left| R_{s,h}^{n+1} \right|^2 \mathrm{d}x + \Delta t E_h^n.$$

Recalling (73), we deduce

$$\mathcal{T}_s^{n+1} \le \frac{\gamma_4}{2} \int_\Omega \rho_s(1-\phi) \left| \widetilde{e}_{s,h}^{n+1} - e_{s,h}^n \right|^2 \mathrm{d}x + \Delta t E_h^n + C\Delta t(\Delta t + h^\ell + h^r)^2. \tag{82}$$

Now, gathering (79), (80), (81) and (82) into (78) leads to

$$\begin{aligned}
(E_h^{n+1} - E_h^n) + \frac{1}{2} \int_\Omega \sigma_s(e_{u,h}^{n+1} - e_{u,h}^n) : \varepsilon(e_{u,h}^{n+1} - e_{u,h}^n) \,\mathrm{d}x + \frac{1-\gamma_4}{2} \int_\Omega \rho_s(1-\phi) \left| \widetilde{e}_{s,h}^{n+1} - e_{s,h}^n \right|^2 \mathrm{d}x \\
+ \frac{1}{2} \int_\Omega \rho_f \phi \left| \widetilde{e}_{f,h}^{n+1} - e_{f,h}^n \right|^2 \mathrm{d}x + \frac{1-\gamma_1}{2} \int_\Omega \rho_s(1-\phi) \left| e_{s,h}^{n+1} - \widetilde{e}_{s,h}^{n+1} \right|^2 \mathrm{d}x \\
+ \frac{1-\gamma_2}{2} \int_\Omega \rho_f \phi \left| e_{f,h}^{n+1} - \widetilde{e}_{f,h}^{n+1} \right|^2 \mathrm{d}x + (1-\gamma_3)\Delta t \int_\Omega \phi\, \sigma_f(\widetilde{e}_{f,h}^{n+1}) : \varepsilon(\widetilde{e}_{f,h}^{n+1}) \,\mathrm{d}x \\
+ \Delta t \int_\Omega \phi^2 k_f^{-1} \left(\widetilde{e}_{f,h}^{n+1} - \widetilde{e}_{s,h}^{n+1} \right)^2 \mathrm{d}x \le C\Delta t(\Delta t + h^\ell + h^r)^2 \\
+ \Delta t(E_h^{n+1} + E_h^n) + C\Delta t^2 \left\| \nabla p_h(t^{n+1}) \right\|^2.
\end{aligned}$$

Setting $\gamma_1 = \gamma_2 = \gamma_3 = \gamma_4 = \frac{1}{2}$ and summing between 0 and $N-1$ yields

$$\begin{aligned}
E_h^N + \frac{1}{2} \sum_{n=0}^{N-1} \int_\Omega \sigma_s(e_{u,h}^{n+1} - e_{u,h}^n) : \varepsilon(e_{u,h}^{n+1} - e_{u,h}^n) \,\mathrm{d}x + \frac{1}{4} \sum_{n=0}^{N-1} \int_\Omega \rho_s(1-\phi) \left| \widetilde{e}_{s,h}^{n+1} - e_{s,h}^n \right|^2 \mathrm{d}x \\
+ \frac{1}{2} \sum_{n=0}^{N-1} \int_\Omega \rho_f \phi \left| \widetilde{e}_{f,h}^{n+1} - e_{f,h}^n \right|^2 \mathrm{d}x + \frac{1}{4} \sum_{n=0}^{N-1} \int_\Omega \rho_s(1-\phi) \left| e_{s,h}^{n+1} - \widetilde{e}_{s,h}^{n+1} \right|^2 \mathrm{d}x \\
+ \frac{1}{4} \sum_{n=0}^{N-1} \int_\Omega \rho_f \phi \left| e_{f,h}^{n+1} - \widetilde{e}_{f,h}^{n+1} \right|^2 \mathrm{d}x + \frac{\Delta t}{2} \sum_{n=0}^{N-1} \int_\Omega \phi\, \sigma_f(\widetilde{e}_{f,h}^{n+1}) : \varepsilon(\widetilde{e}_{f,h}^{n+1}) \,\mathrm{d}x \\
+ \Delta t \sum_{n=0}^{N-1} \int_\Omega \phi^2 k_f^{-1} \left(\widetilde{e}_{f,h}^{n+1} - \widetilde{e}_{s,h}^{n+1} \right)^2 \mathrm{d}x \le E_h^0 + C(\Delta t + h^\ell + h^r)^2 \\
+ \Delta t \sum_{n=0}^{N-1} (E_h^{n+1} + E_h^n) + C\Delta t^2 \sum_{n=0}^{N-1} \left\| \nabla p_h(t^{n+1}) \right\|^2.
\end{aligned} \tag{83}$$

To conclude, let us focus on the pressure term remaining in the right-hand side of the above estimate, which is responsible for the loss of the scheme's first-order convergence in time. Using Poincaré-Wirtinger inequality together with the regularity assumption made on the solution, we observe that

$$\begin{aligned}
C\Delta t^2 \sum_{n=0}^{N-1} \left\| \nabla p_h(t^{n+1}) \right\|^2 &\le C\Delta t^2 \sum_{n=0}^{N-1} \left\| \nabla p_h(t^{n+1}) - \nabla p(t^{n+1}) \right\|^2 + C\Delta t^2 \sum_{n=0}^{N-1} \left\| \nabla p(t^{n+1}) \right\|^2 \\
&\le C\Delta t^2 \sum_{n=0}^{N-1} \left\| p_h(t^{n+1}) - p(t^{n+1}) \right\|^2 + C\Delta t \cdot \Delta t \sum_{n=0}^{N-1} \left\| \nabla p(t^{n+1}) \right\|^2 \\
&\le C\Delta t(h^\ell + h^r)^2 + C\Delta t \|p\|^2_{\mathrm{L}^2(0,T;\mathrm{H}^1(\Omega))}.
\end{aligned}$$

Since $\Delta t < 1$, estimate (77) then follows from (83), (76) and Lemma 2.9. □

Remark 3.3. *Another possible strategy to control the solid residual term $\mathcal{T}_s^{n+1}$ is to use the decomposition*

$$\mathcal{T}_s^{n+1} = \Delta t \int_\Omega \rho_s(1-\phi) R_{s,h}^{n+1} \cdot (\widetilde{e}_{s,h}^{n+1} - \widetilde{e}_{f,h}^{n+1}) \,\mathrm{d}x + \Delta t \int_\Omega \rho_s(1-\phi) R_{s,h}^{n+1} \cdot \widetilde{e}_{f,h}^{n+1} \,\mathrm{d}x.$$

The first term can be estimated using the friction dissipation term, while the second can be bounded thanks to the viscous fluid dissipation. Nevertheless, this leads to an estimate with a constant C that depends on $k_{\max}^{-1}$, which is often large in practice. Note moreover that in the parabolic/parabolic case $\nu_s > 0$ this difficulty does not appear since $\mathcal{T}_s^{n+1}$ can then be directly controled using the viscous solid dissipation.

Therefore, we have proved that the non-incremental version of Scheme 5 shows a $\mathcal{O}(\sqrt{\Delta t})$ convergence in time. The next theorem establishes that the incremental version of the scheme enhances it by recovering first-order convergence.

Theorem 3.4. *Assume that $i = 1$ and that the solution of Problem (3) is regular enough, in particular that $\partial_t p \in \mathrm{L}^2(0,T;\mathrm{H}^1(\Omega))$ and $p(0) \in \mathrm{H}^1(\Omega)$. If $\Delta t < 1$ and if the initialization of Scheme 5 satisfies (76), then for any $0 \le N \le n_T$, it holds*

$$\begin{aligned} E_h^N + \frac{\Delta t^2}{2} \int_\Omega \rho_{\mathrm{eff}}^{-1} \left|\nabla \delta_h^N\right|^2 \mathrm{d}x + \frac{1}{2} \sum_{n=0}^{N-1} \int_\Omega \sigma_s(e_{u,h}^{n+1} - e_{u,h}^n) : \varepsilon(e_{u,h}^{n+1} - e_{u,h}^n) \,\mathrm{d}x \\ + \frac{1}{4} \sum_{n=0}^{N-1} \int_\Omega \rho_s(1-\phi) \left|\widetilde{e}_{s,h}^{n+1} - e_{s,h}^n\right|^2 \mathrm{d}x + \frac{1}{2} \sum_{n=0}^{N-1} \int_\Omega \rho_f \phi \left|\widetilde{e}_{f,h}^{n+1} - e_{f,h}^n\right|^2 \mathrm{d}x \\ + \frac{\Delta t}{2} \sum_{n=0}^{N-1} \int_\Omega \phi\, \sigma_f(\widetilde{e}_{f,h}^{n+1}) : \varepsilon(\widetilde{e}_{f,h}^{n+1}) \,\mathrm{d}x + \Delta t \sum_{n=0}^{N-1} \int_\Omega \phi^2 k_f^{-1} \left(\widetilde{e}_{f,h}^{n+1} - \widetilde{e}_{s,h}^{n+1}\right)^2 \mathrm{d}x \\ \le C(h^\ell + h^r)^2 + C\Delta t^2, \quad (84) \end{aligned}$$

with $C > 0$ a constant independent of h and that behaves as $\exp(1/(1-\Delta t))$.

Proof. The proof is very close to the proof of Theorem 3.2. Let us denote by

$$\psi_h^n = p_h(t^{n+1}) - p_h^n$$

the pressure term involved in the prediction step (74). Then, the pressure term involved in the correction step error system (75) can be rewritten as

$$p_h^n - p_h^{n+1} = p_h^n - p_h(t^{n+1}) + p_h(t^{n+1}) - p_h^{n+1} = \delta_h^{n+1} - \psi_h^n.$$

Therefore, testing (74) with $(w_{s,h}, d_{s,h}, w_{f,h}) = \Delta t\,(\widetilde{e}_{s,h}^{n+1}, e_{u,h}^{n+1}, \widetilde{e}_{f,h}^{n+1})$ and (75) successively with $(w_{s,h}, w_{f,h}, q_h) = \Delta t\,(e_{s,h}^{n+1}, e_{f,h}^{n+1}, \delta_h^{n+1})$ and $(w_{s,h}, w_{f,h}, q_h) = \left(\rho_s^{-1}\Delta t^2\, \nabla\psi_h^n, \rho_f^{-1}\Delta t^2\, \nabla\psi_h^n, 0\right)$, we obtain, as in (48),

$$\begin{aligned} \left(E_h^{n+1} - E_h^n\right) + \frac{1}{2} \int_\Omega \sigma_s(e_{u,h}^{n+1} - e_{u,h}^n) : \varepsilon(e_{u,h}^{n+1} - e_{u,h}^n) \,\mathrm{d}x + \frac{1}{2} \int_\Omega \rho_s(1-\phi) \left|\widetilde{e}_{s,h}^{n+1} - e_{s,h}^n\right|^2 \mathrm{d}x \\ + \frac{1}{2} \int_\Omega \rho_f \phi \left|\widetilde{e}_{f,h}^{n+1} - e_{f,h}^n\right|^2 \mathrm{d}x + \Delta t \int_\Omega \phi\, \sigma_f(\widetilde{e}_{f,h}^{n+1}) : \varepsilon(\widetilde{e}_{f,h}^{n+1}) \,\mathrm{d}x + \Delta t \int_\Omega \phi^2 k_f^{-1} \left(\widetilde{e}_{f,h}^{n+1} - \widetilde{e}_{s,h}^{n+1}\right)^2 \mathrm{d}x \\ + \frac{\Delta t^2}{2} \left(\int_\Omega \rho_{\mathrm{eff}}^{-1} \left|\nabla \delta_h^{n+1}\right|^2 \mathrm{d}x - \int_\Omega \rho_{\mathrm{eff}}^{-1} \left|\nabla \psi_h^n\right|^2 \mathrm{d}x \right) = \mathcal{T}_u^{n+1} + \mathcal{T}_s^{n+1} + \mathcal{T}_f^{n+1}. \quad (85) \end{aligned}$$

The displacement and velocities residual terms $\mathcal{T}_u^{n+1}$, $\mathcal{T}_s^{n+1}$ and $\mathcal{T}_f^{n+1}$ are estimated exactly as in the proof of Theorem 3.2. The only terms requiring a special attention are the new pressure terms appearing in the left-hand side. They will be treated as in [Guermond and Quartapelle, 1998].

Since

$$\psi_h^n = p_h(t^{n+1}) - p_h(t^n) + p_h(t^n) - p_h^n = p_h(t^{n+1}) - p_h(t^n) + \delta_h^n,$$

the inequality $(a+b)^2 \le (1+\gamma)a^2 + \left(1+\frac{1}{\gamma}\right)b^2$ with $\gamma = \Delta t$ yields

$$\Delta t^2 \left|\nabla \psi_h^n\right|^2 \le \Delta t^2 (1+\Delta t) \left|\delta_h^n\right|^2 + \Delta t (1+\Delta t) \left|\nabla\big(p_h(t^{n+1}) - p_h(t^n)\big)\right|^2.$$

Hence

$$\begin{aligned}\frac{\Delta t^2}{2} \int_\Omega \rho_{\text{eff}}^{-1} \left|\nabla \psi_h^n\right|^2 \,\mathrm{d}x \le \frac{\Delta t^2}{2} \int_\Omega \rho_{\text{eff}}^{-1} \left|\nabla \delta_h^n\right|^2 \,\mathrm{d}x + \frac{\Delta t^3}{2} \int_\Omega \rho_{\text{eff}}^{-1} \left|\nabla \delta_h^n\right|^2 \,\mathrm{d}x \\ + C\Delta t(1+\Delta t) \left\|\nabla\big(p_h(t^{n+1}) - p_h(t^n)\big)\right\|^2,\end{aligned}$$

so that (85) becomes

$$\begin{aligned}&\big(E_h^{n+1} - E_h^n\big) + \frac{1}{2}\int_\Omega \sigma_s(e_{u,h}^{n+1} - e_{u,h}^n) : \varepsilon(e_{u,h}^{n+1} - e_{u,h}^n)\,\mathrm{d}x + \frac{1}{2}\int_\Omega \rho_s(1-\phi)\left|\widetilde{e}_{s,h}^{n+1} - e_{s,h}^n\right|^2 \mathrm{d}x \\ &\quad + \frac{1}{2}\int_\Omega \rho_f \phi \left|\widetilde{e}_{f,h}^{n+1} - e_{f,h}^n\right|^2 \mathrm{d}x + \Delta t \int_\Omega \phi\, \sigma_f(\widetilde{e}_{f,h}^{n+1}) : \varepsilon(\widetilde{e}_{f,h}^{n+1})\,\mathrm{d}x + \Delta t \int_\Omega \phi^2 k_f^{-1}\big(\widetilde{e}_{f,h}^{n+1} - \widetilde{e}_{s,h}^{n+1}\big)^2 \mathrm{d}x \\ &\qquad + \frac{\Delta t^2}{2}\left(\int_\Omega \rho_{\text{eff}}^{-1}\left|\nabla \delta_h^{n+1}\right|^2 \mathrm{d}x - \int_\Omega \rho_{\text{eff}}^{-1}\left|\nabla \delta_h^n\right|^2 \mathrm{d}x\right) \le \mathcal{T}_u^{n+1} + \mathcal{T}_s^{n+1} + \mathcal{T}_f^{n+1} \\ &\qquad\qquad + \frac{\Delta t^3}{2}\int_\Omega \rho_{\text{eff}}^{-1}\left|\nabla \delta_h^n\right|^2 \mathrm{d}x + C\Delta t(1+\Delta t)\left\|\nabla\big(p_h(t^{n+1}) - p_h(t^n)\big)\right\|^2.\end{aligned}$$

Estimating $\mathcal{T}_u^{n+1}$, $\mathcal{T}_s^{n+1}$ and $\mathcal{T}_f^{n+1}$ as in Theorem 3.2 and summing the above estimates for n between 0 and $N-1$, we infer

$$\begin{aligned}&E_h^N + \frac{\Delta t^2}{2}\int_\Omega \rho_{\text{eff}}^{-1}\left|\nabla \delta_h^N\right|^2 \mathrm{d}x + \frac{1}{2}\sum_{n=0}^{N-1}\int_\Omega \sigma_s(e_{u,h}^{n+1} - e_{u,h}^n) : \varepsilon(e_{u,h}^{n+1} - e_{u,h}^n)\,\mathrm{d}x \\ &\qquad + \frac{1}{4}\sum_{n=0}^{N-1}\int_\Omega \rho_s(1-\phi)\left|\widetilde{e}_{s,h}^{n+1} - e_{s,h}^n\right|^2 \mathrm{d}x + \frac{1}{2}\sum_{n=0}^{N-1}\int_\Omega \rho_f\phi\left|\widetilde{e}_{f,h}^{n+1} - e_{f,h}^n\right|^2 \mathrm{d}x \\ &\qquad + \frac{\Delta t}{2}\sum_{n=0}^{N-1}\int_\Omega \phi\,\sigma_f(\widetilde{e}_{f,h}^{n+1}) : \varepsilon(\widetilde{e}_{f,h}^{n+1})\,\mathrm{d}x + \Delta t\sum_{n=0}^{N-1}\int_\Omega \phi^2 k_f^{-1}\Big(\widetilde{e}_{f,h}^{n+1} - \widetilde{e}_{s,h}^{n+1}\Big)^2 \mathrm{d}x \\ &\qquad \le E_h^0 + \frac{\Delta t^2}{2}\int_\Omega \rho_{\text{eff}}^{-1}\left|\nabla \delta_h^0\right|^2 \mathrm{d}x + C(\Delta t + h^\ell + h^r)^2 + \Delta t\sum_{n=0}^{N-1}(E_h^{n+1} + E_h^n) \\ &\qquad\qquad + \Delta t\sum_{n=0}^{N-1}\frac{\Delta t^2}{2}\int_\Omega \rho_{\text{eff}}^{-1}\left|\nabla \delta_h^n\right|^2 \mathrm{d}x + C\Delta t(1+\Delta t)\sum_{n=0}^{N-1}\left\|\nabla\big(p_h(t^{n+1}) - p_h(t^n)\big)\right\|^2.\end{aligned}$$

To retrieve (84), we observe, using (70),

$$\begin{aligned}\sum_{n=0}^{N-1}\left\|\nabla\big(p_h(t^{n+1}) - p_h(t^n)\big)\right\|^2 &= \sum_{n=0}^{N-1}\left\|\nabla\big(p_h(t^{n+1}) - p(t^{n+1}) + p(t^{n+1}) - p(t^n) + p(t^n) - p_h(t^n)\big)\right\|^2 \\ &\le CN(h^\ell + h^r)^2 + C\Delta t\|\partial_t p\|^2_{\mathrm{L}^2(0,T;\mathrm{H}^1(\Omega))}\end{aligned}$$

and thus

$$C\Delta t(1+\Delta t)\sum_{n=0}^{N-1}\left\|\nabla\big(p_h(t^{n+1}) - p_h(t^n)\big)\right\|^2 \le C(h^\ell + h^r)^2 + C\Delta t^2.$$

The final conclusion once again follows from discrete Grönwall's lemma. □

4 Numerical results

In this section, we present simulations to numerically illustrate the properties of the different schemes analyzed previously. In Section 4.1, we show the influence of the explicit treatment of permeability on the scheme stability. If the permeability is treated implicitly, the derived convergence rates are numerically confirmed (see Section 4.2). Then, Section 4.3 compares the precision and efficiency of the projection scheme with respect to the monolithic approach. Finally, total stress boundary conditions are investigated from a numerical point of view in Section 4.4. All simulations were performed with the FEniCS software [Logg et al., 2012; Alnæs et al., 2015] using a direct LU solver.

4.1 The permeability treatment issue

We start by studying the fully decoupled projection scheme in non-incremental or incremental form, namely Schemes 1 and 2. The scheme implementation is validated thanks to the manufactured solution method in the unit square domain $\Omega = (0,1)^2$. To build an analytical solution of Problem (3), we consider the function

$$v^{\mathrm{ref}}(x,y) = \Big(\sin(2\pi y)\big(\cos(2\pi x)-1\big), \sin(2\pi x)\big(1-\cos(2\pi y)\big)\Big),$$

which verifies $\operatorname{div} v^{\mathrm{ref}} = 0$ in Ω and $v^{\mathrm{ref}} = 0$ on $\partial\Omega$. Assuming that the porosity ϕ is constant, we set

$$v_s^{\mathrm{ref}}(x,y,t) = t\phi\, v^{\mathrm{ref}}(x,y) \quad \text{and} \quad v_f^{\mathrm{ref}}(x,y,t) = t(1-\phi)\, v^{\mathrm{ref}}(x,y),$$

so that

$$\operatorname{div}\big((1-\phi)v_s^{\mathrm{ref}} + \phi\, v_f^{\mathrm{ref}}\big) = t\phi(1-\phi)\operatorname{div} v^{\mathrm{ref}} = 0.$$

For the pressure analytical solution, we take $p^{\mathrm{ref}}(x,y,t) = t\sin(2\pi x)\sin(2\pi y)$. In order to satisfy the inf-sup condition (67), the solid and fluid parts are discretized using $[\mathbb{P}^2]^d$ continuous finite elements, and the pressure with $\mathbb{P}^1$ continuous finite elements. The projection scheme is implemented with the Poisson-formulation of the correction step, and the solid displacement unknown is eliminated following Remark 2.4. More precisely, denoting by f_s^{ref} and f_f^{ref} the right-hand side computed from the analytical solution, the weak formulation of Scheme 1 associated with the manufactured solution above reads

Step 1: `(prediction step)`

- **Step 1.1**: `(structure prediction sub-step)`
  Find $\widetilde{v}_{s,h}^{n+1} \in X_h$ such that $\widetilde{v}_{s,h}^{n+1}{}_{|\partial\Omega} = 0$ and, for any $w_{s,h} \in X_h$,

$$\int_\Omega \rho_s(1-\phi)\frac{\widetilde{v}_{s,h}^{n+1} - v_{s,h}^n}{\Delta t}\cdot w_{s,h}\,\mathrm{d}x + \int_\Omega \sigma_s\Big(u_{s,h}^n + \frac{\Delta t}{2}\widetilde{v}_{s,h}^{n+\frac{1}{2}\sharp}\Big) : \varepsilon(w_{s,h})\,\mathrm{d}x$$
$$- \int_\Omega \phi^2 k_f^{-1}(v_{f,h}^n - \widetilde{v}_{s,h}^{n+\frac{1}{2}\sharp})\cdot w_{s,h}\,\mathrm{d}x = \int_\Omega f_s^{\mathrm{ref}}(t^{n+1})\cdot w_{s,h}\,\mathrm{d}x.$$

- **Step 1.2**: `(solid displacement update)`
  Compute

$$u_{s,h}^{n+1} = u_{s,h}^n + \Delta t\, \widetilde{v}_{s,h}^{n+\frac{1}{2}\sharp}.$$

- **Step 1.3**: `(fluid prediction sub-step)`
  Find $\widetilde{v}_{f,h}^{n+1} \in X_h$ such that $\widetilde{v}_{f,h}^{n+1}{}_{|\partial\Omega} = 0$ and, for any $w_{f,h} \in X_h$,

$$\int_\Omega \rho_f\phi\frac{\widetilde{v}_{f,h}^{n+1} - v_{f,h}^n}{\Delta t}\cdot w_{f,h}\,\mathrm{d}x + \int_\Omega \phi\,\sigma_f(\widetilde{v}_{f,h}^{n+1}) : \varepsilon(w_{f,h})\,\mathrm{d}x$$
$$+ \int_\Omega \phi^2 k_f^{-1}(\widetilde{v}_{f,h}^{n+1} - \widetilde{v}_{s,h}^{n+\frac{1}{2}\sharp})\cdot w_{f,h}\,\mathrm{d}x = \int_\Omega f_f^{\mathrm{ref}}(t^{n+1})\cdot w_{f,h}\,\mathrm{d}x.$$

Step 2: `(pressure step)`
Find $p_h^{n+1} \in Q_h$ such that $\int_\Omega p_h^{n+1}\,\mathrm{d}x = 0$ and, for any $q_h \in Q_h$,

$$\int_\Omega \rho_{\text{eff}}^{-1} \nabla p_h^{n+1} \cdot \nabla q_h \,\mathrm{d}x = -\Delta t^{-1} \int_\Omega \operatorname{div}\left((1-\phi)\widetilde{v}_{s,h}^{n+1} + \phi\,\widetilde{v}_{f,h}^{n+1}\right) q_h \,\mathrm{d}x.$$

Step 3: `(correction step)`

- **Step 3.1**: `(solid correction sub-step)`
  Find $v_{s,h}^{n+1} \in Y_{s,h}$ such that, for any $w_{s,h} \in Y_{s,h}$,

$$\int_\Omega \rho_s(1-\phi) v_{s,h}^{n+1} \cdot w_{s,h}\,\mathrm{d}x = \int_\Omega \rho_s(1-\phi)\widetilde{v}_{s,h}^{n+1} \cdot w_{s,h}\,\mathrm{d}x - \Delta t \int_\Omega (1-\phi)\nabla p_h^{n+1} \cdot w_{s,h}.$$

- **Step 3.2**: `(fluid correction sub-step)`
  Find $v_{f,h}^{n+1} \in Y_{f,h}$ such that, for any $w_{f,h} \in Y_{f,h}$,

$$\int_\Omega \rho_f \phi\, v_{f,h}^{n+1} \cdot w_{f,h}\,\mathrm{d}x = \int_\Omega \rho_f \phi\, \widetilde{v}_{f,h}^{n+1} \cdot w_{f,h}\,\mathrm{d}x - \Delta t \int_\Omega \phi\, \nabla p_h^{n+1} \cdot w_{f,h}.$$

The simulation is run with the following parameters: $\phi = 0.5$, $\rho_f = \rho_s = 10^3$, $\mu_f = \lambda_s = \mu_s = 1$ and $k_f = 10^{-6}\mathbb{I}$. From Theorem 2.8, the stability of the scheme is guaranteed as long as the time step condition (28) is fulfilled, namely

$$\Delta t < \left(\frac{\rho_f \rho_s (1-\phi_{\max})}{2\phi_{\max}^3 (k_{\max}^{-1})^2}\right)^{1/2} = 2 \times 10^{-3}.$$

If the time step condition is not satisfied, even if Figure 1b shows no instable behavior, the pressure profile is far from the reference solution.

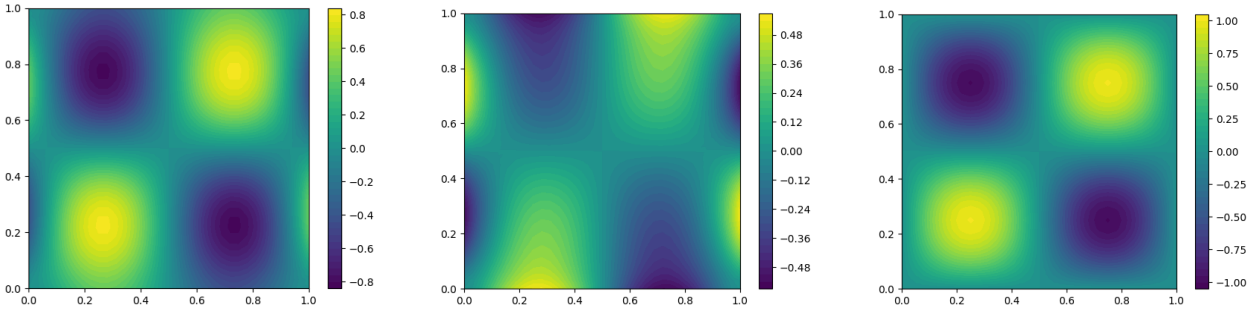

(a) $\Delta t = 10^{-3}$ (b) $\Delta t = 10^{-2}$ (c) Reference solution

Figure 1: Pressure profile at $T = 1$ for different values of time step compared to the analytical solution.

In Figure 1a, the pressure profile is closer to the reference solution, but we note that the pressure is badly approximated on the boundaries. This is confirmed by Figure 2, which plots the difference between the numerical and analytical solutions. The error is smaller for the incremental version of the scheme, see Figure 2b, but still large. In fact, this large error comes from the explicit treatment of the permeability term in the solid prediction sub-step. Indeed, if it is treated implicitly, Figure 3 shows that the error is considerably reduced.

Moreover, we observe on Figure 3 that the error is mainly located in the corners of the domain and in the boundaries. The error occuring at the corners is probably due to the lack of regularity of the domain.

As for the error on the boundaries, it is a consequence of the non-physical pressure boundary condition $\rho_{\text{eff}}^{-1}\nabla p_h^{n+1}\cdot n = 0$, which is known to induce a numerical boundary layer in incompressible fluid problems [Rannacher, 1992]. For fluid problems, this issue has been adressed by developing projection schemes in rotational form [Timmermans et al., 1996; Guermond and Shen, 2003]. Adapting such schemes to the porous problem (3) is a natural perspective of this work.

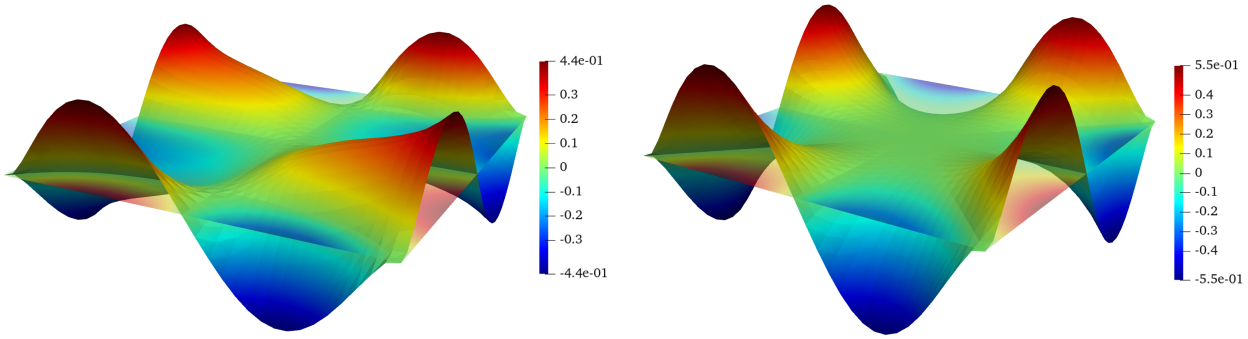

(a) Non-incremental version (b) Incremental version

Figure 2: Pressure error field $p(t^n) - p_h^n$ at $T = 1$ obtained for Schemes 1 and 2.

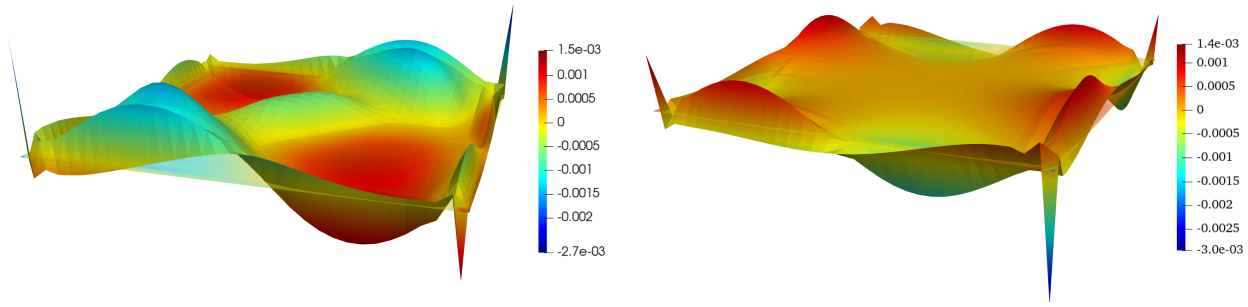

(a) Non-incremental version (b) Incremental version

Figure 3: Pressure error field $p(t^n) - p_h^n$ at $T = 1$ obtained for Scheme 3 (scale factor 100).

As a conclusion, when the time step condition (28) is restrictive, namely when the permeability is low compared to the densities, it is better to treat the permeability implicitly in the prediction step and use Schemes 3 or 5. Such schemes are not subject to any stability condition and are hence very robust with respect to the material parameters, as we will now illustrate.

4.2 Convergence and robustness with implicit treatment of permeability

We now focus on the numerical properties of Scheme 5 in which the permeability is treated implicitly in the prediction step and for which a complete convergence analysis has been carried out in Section 3. In Figure 4, convergence graphs are presented using the same manufactured solution as in the previous section and with the following parameters: $\phi = 0.5$, $\rho_f = \rho_s = \mu_f = \lambda_s = \mu_s = 1$, $k_f = \mathbb{I}$ and $T = 0.25$. Here again, the solid and fluid unknowns are discretized using $[\mathbb{P}^2]^d$ elements and the pressure with $\mathbb{P}^1$ elements, so that the inf-sup condition (67) is satisfied.

Figure 4 confirms that the time convergence is better for the incremental than for the non-incremental version of the projection scheme, as predicted by Theorems 3.2 and 3.4. The error value is indeed considerably reduced in Figure 4b compared to Figure 4a. Moreover, the convergence rates obtained for the

non-incremental version is 0.8, while first-order convergence is recovered with the incremental version. Note that the time convergence rates obtained numerically are slightly better than the one proved in Theorems 3.2 and 3.4, namely 1/2 and 1 for $i = 0$ and $i = 1$ respectively. This probably comes from the regularity of the analytical solution under consideration. Interestingly, we do not find much difference between the convergence rates of velocities and pressures, while for incompressible fluids, thanks to a duality argument, projection methods can be used to show that the time convergence rate of fluid velocity is actually larger than the one of the pressure [Shen, 1992]. Here, such an argument cannot be simply reproduced because of the lack of regularity induced by the hyberpolic-parabolic structure of Problem (3), see [Barré et al., 2023a].

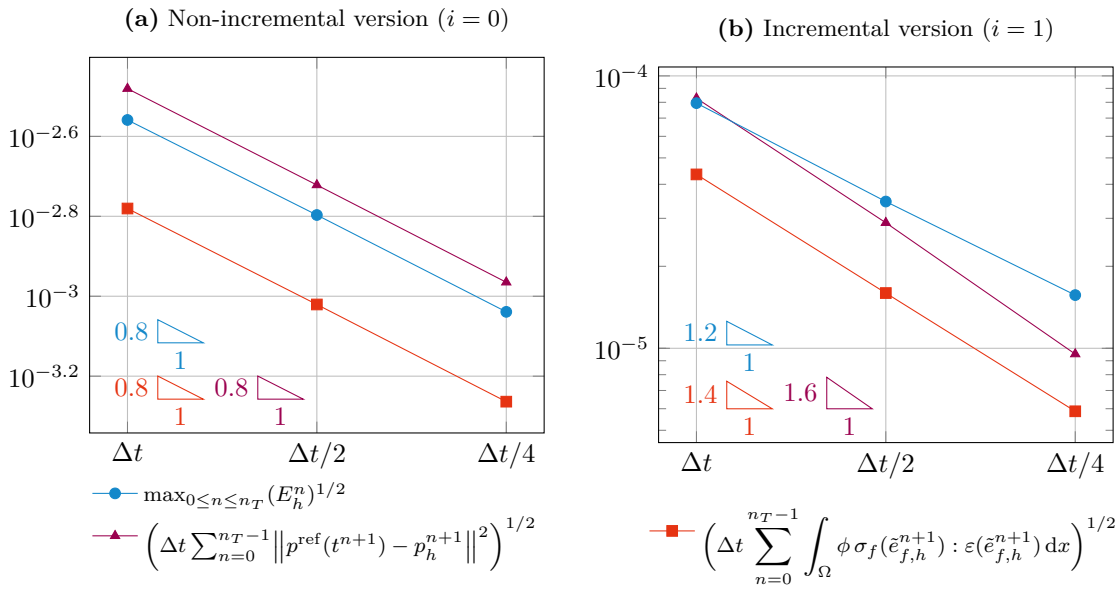

Figure 4: Convergence graphs of Scheme 5 with respect to the time step. Simulation run for a very refined mesh, starting from the time step $\Delta t = 0.001$.

In Figure 5, we study the influence of the key physical parameters on the pressure error. Figure 5 indicates that the time convergence rates of the scheme are not altered when varying porosity or permeability. This comes from the fact that the discrete inf-sup condition (67) does not depend on porosity and that the permeability is treated implicitly in the prediction step. Similar results hold for Scheme 3 and hence illustrate the robustness of these schemes with respect to permeability and porosity.

Finally, Figure 6 emphasizes the importance of the discrete inf-sup condition for the spatial convergence of the scheme. Even if none of the steps of the projection method in Poisson form requires solving a saddle-point problem, we have seen in (16) that the proposed splitting schemes are consistent with the monolithic algorithm, for which the inf-sup condition is essential. As a result, if the inf-sup condition (67) is not satisfied, numerical oscillations appear on the pressure profile of Figure 6a.

4.3 Comparison of the splitting and monolithic approaches

Let us now compare the projection scheme analyzed in this article with the monolithic approach considered in [Burtschell et al., 2019; Barnafi et al., 2021; Barré et al., 2023b]. Figure 7 shows the result of the two approaches for the analytical solution test case with $\phi = 0.5$, $\rho_f = \rho_s = \mu_f = \lambda_s = \mu_s = 1$, $k_f = \mathbb{I}$ and $T = 1$. Since the time step condition (28) is not very restrictive in this case, we can use the fully decoupled scheme together with $\Delta t = 0.01$.

In Figure 7b, we see that the non-incremental version of the scheme yields a poor approximation of the pressure field, while the monolithic and incremental projection scheme results seem to be close to the reference solution. However, when computing the error with respect to the reference solution, Table 1 shows

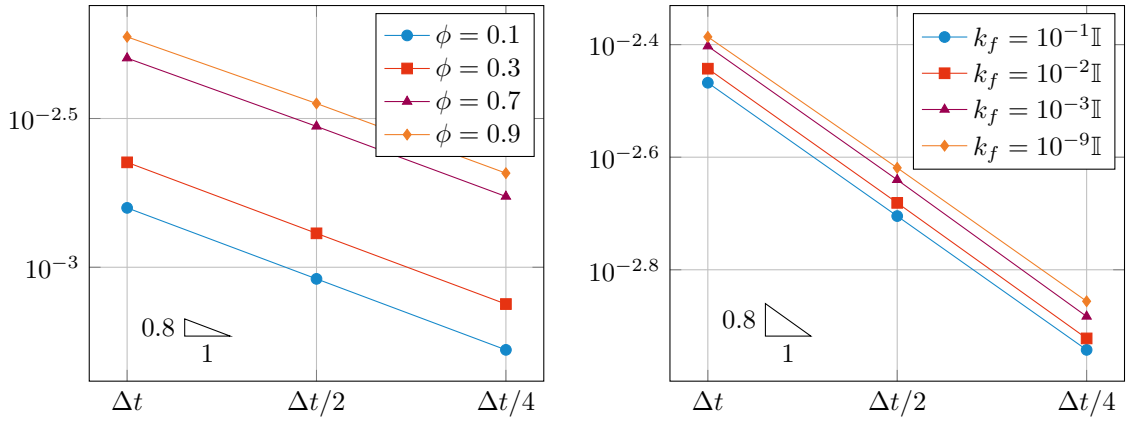

Figure 5: Pressure error sensitivity with respect to porosity and permeability. Simulation of Scheme 5 with $i = 0$ run for a very refined mesh, starting from the time step $\Delta t = 0.001$.

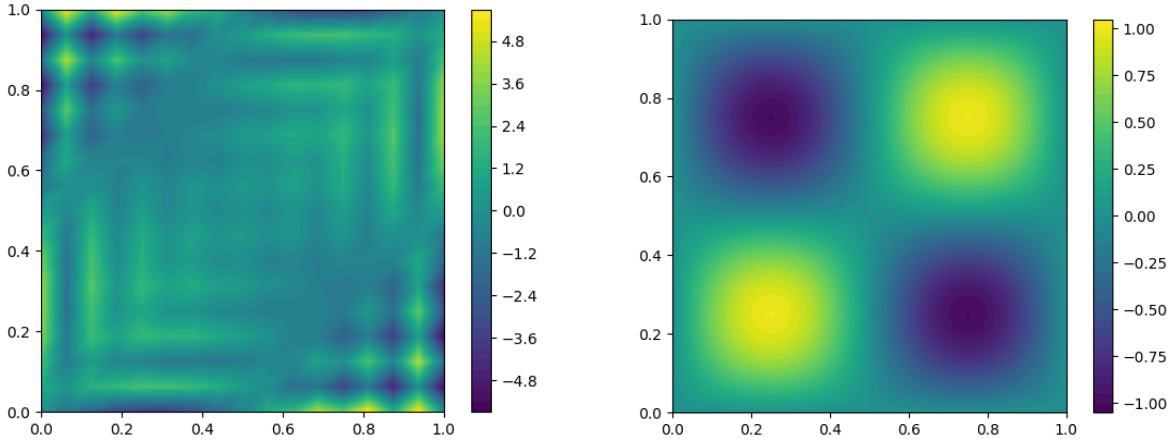

(a) Solid and fluid quantities discretized with $[\mathbb{P}^1]^d$ elements

(b) Solid and fluid quantities discretized with $[\mathbb{P}^2]^d$ elements

Figure 6: Pressure field at $T = 1$ for different choices of discretization for the solid and fluid quantities.

that the monolithic scheme is more precise than the incremental projection scheme. For a smaller time step, namely $\Delta t = 0.001$, the precision of the monolithic and incremental projection schemes are comparable. Moreover, the projection schemes are faster than the monolithic one.

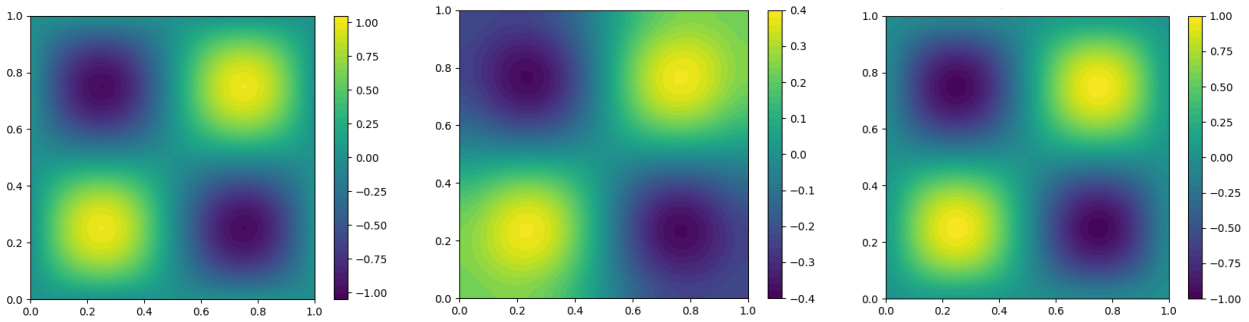

(a) Monolithic approach (scheme resulting from (10))

(b) Non-incremental projection method (Scheme 1)

(c) Incremental projection method (Scheme 2)

Figure 7: Pressure profile obtained at $T = 1$ with the projection and monolithic schemes.

	Monolithic scheme		Scheme 1		Scheme 2	
	$\Delta t = 0.01$	$\Delta t = 0.001$	$\Delta t = 0.01$	$\Delta t = 0.001$	$\Delta t = 0.01$	$\Delta t = 0.001$
Execution time (s)	4.6	45	4.0	41	4.0	39
Energy error	1.6×10^{-3}	5.6×10^{-4}	5.8×10^{-2}	1.7×10^{-2}	5.5×10^{-3}	6.2×10^{-4}
Fluid error	2.4×10^{-2}	2.7×10^{-2}	0.30	0.38	2.9×10^{-2}	2.7×10^{-3}
Pressure error	7.2×10^{-4}	9.5×10^{-4}	2.7	2.0	3.2×10^{-2}	1.1×10^{-3}

Table 1: Execution time and errors for the monolithic and projection schemes. The energy, fluid and pressure errors correspond to the square root of the quantities $\max_{0\leq n\leq n_T} E_h^n$, $\Delta t \sum_{n=0}^{n_T-1} \int_\Omega \phi\, \sigma_f(\tilde{e}_{f,h}^{n+1}) : \varepsilon(\tilde{e}_{f,h}^{n+1})\, \mathrm{d}x$ and $\Delta t \sum_{n=0}^{n_T-1} \left\| p^{\mathrm{ref}}(t^{n+1}) - p_h^{n+1} \right\|^2$ respectively.

To compare the efficiency of the two approaches on a more realistic scenario, we now consider a 3D footing problem [Gaspar et al., 2008; Both et al., 2022]. The computational domain is a porous cube of length 64, namely $\Omega = (0, 64)^3$. We use the same physical parameters than in [Both et al., 2022], namely $\phi = 10^{-3}$, $\rho_f = 1000$, $\rho_s = 500$, $\mu_f = 10^{-3}$, $\lambda_s = \frac{E\nu}{(1+\nu)(1-2\nu)}$, $\mu_s = \frac{E}{2(1+\nu)}$ with $E = 3 \times 10^4$ and $\nu = 0.2$, and $k_f = 1 \times 10^{-7}\mathbb{I}$. The porous medium is not subject to any volume forces, but an increasing traction is applied over a square surface of length 32 at the top of the domain. The bottom boundary is fixed, while the porous medium is free to drain on the rest of the boundary. More precisely, we set

$$u_s = v_s = v_f = 0, \qquad \text{on } \Gamma_{\text{fixed}},$$

and

$$\begin{aligned}
\sigma_s(u_s)n - (1-\phi)\, pn &= -(1-\phi)p_{\text{foot}}n, && \text{on } \Gamma_{\text{foot}},\\
\phi\, \sigma_f(v_f)n - \phi\, pn &= -\phi\, p_{\text{foot}}n, && \text{on } \Gamma_{\text{foot}},\\
\sigma_s(u_s)n - (1-\phi)\, pn &= 0, && \text{on } \Gamma_{\text{drain}},\\
\phi\, \sigma_f(v_f)n - \phi\, pn &= 0, && \text{on } \Gamma_{\text{drain}},
\end{aligned}$$

with $\Gamma_{\text{fixed}} = (0, 64)^2 \times \{0\}$, $\Gamma_{\text{foot}} = (12, 48)^2 \times \{64\}$, $\Gamma_{\text{drain}} = \partial\Omega \setminus \overline{\Gamma_{\text{fixed}} \cup \Gamma_{\text{foot}}}$ and $p_{\text{foot}}(t) = 10^5 t$. In order to fulfill the discrete inf-sup condition (67), we consider $[\mathbb{P}^1_{\text{bul}}]^d$ finite elements for the solid and fluid unknowns together with $\mathbb{P}^1$ finite elements for the pressure. The corresponding simulation is shown on Figure 8, where we see that the solid displacement is mostly located on the surface where a pressure load is applied.

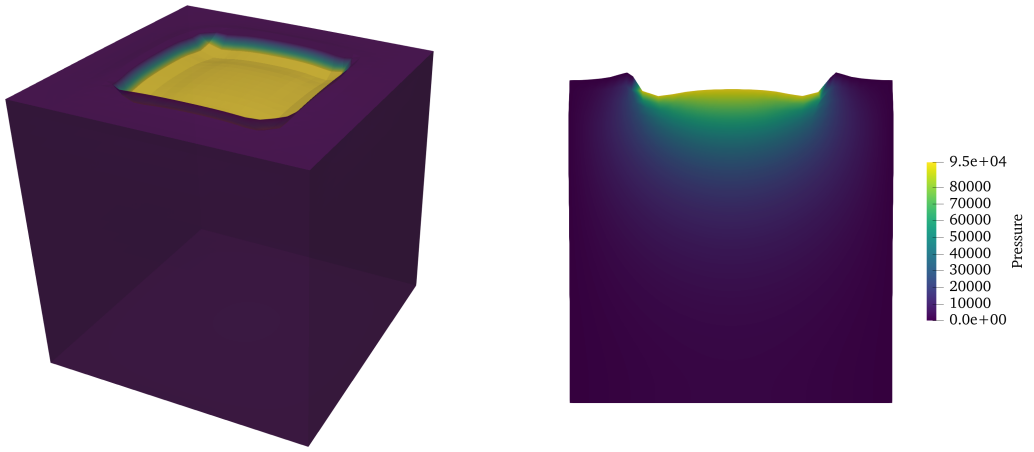

Figure 8: Deformed porous medium and interstitial pressure at $T = 1$ in the footing test case, shown in the whole domain (left) and over a surface cut at the middle of the domain (right). Simulation obtained with a refined mesh (30 elements per side) and $\Delta t = 0.1$ using the non-incremental projection scheme.

In Table 2, we compare the efficiency of the monolithic and splitting approaches by running the simulation with a progressively refined mesh. For large mesh sizes, the computation time of the two approaches is very close, the monolithic scheme being slighlty faster than the projection one. Then, when the mesh becomes finer, the projection scheme performs better and is almost two times faster than the monolithic one when the problem contains approximatively one million of degrees of freedom. For two millions of degrees of freedom, we were not able to run the monolithic scheme on a regular laptop with the considered LU solver, whereas the projection scheme still provides a result in a reasonable amount of time. This confirms the main advantage of the projection scheme that allows to decouple the solid, fluid and pressure degrees and freedom and hence reduce the global size of the matrices to be inverted at each time step.

Elements per side	Number of dofs	Monolithic scheme	Projection scheme	Speed-up
10	45317	0.3	0.4	0.8
15	150172	1.2	1.4	0.9
20	352827	3.4	3.6	0.9
25	685532	9.8	8.2	1.2
30	1180537	31	17	1.8
35	1870092	Memory error	57	–

Table 2: Average computation time per time step for the monolithic and non-incremental projection schemes.

Finally, we end these numerical experiments by investigating the case of total stress boundary conditions.

4.4 Total stress boundary conditions

To test the implementation of total stress boundary conditions, we come back to the manufactured solution method of Section 4.1, with $\Omega = (0,1)^2$, $\phi = 0.5$, $\rho_f = \rho_s = \mu_f = \lambda_s = \mu_s = 1$, $\Delta t = 10^{-3}$ and $T = 1$. In order to prevent any unstability coming from the treatment of permeability, we assume that $k_f = 0$. Note nevertheless that similar results hold for a non-zero permeability. On the left side of the domain, instead of imposing homogeneous Dirichlet boundary conditions, we consider

$$\begin{aligned} v_f &= v_s, \qquad \text{on } \{0\} \times (0,1), \\ \sigma^{\text{tot}} n &= b^{\text{ref}}, \qquad \text{on } \{0\} \times (0,1), \end{aligned} \tag{86}$$

where b^{ref} corresponds to the normal component of the total stress associated with the reference solution. On the other sides of the domain, we enforce homogeneous Dirichlet conditions as before.

To emphasize the difficulty of total stress boundary conditions, we start by imposing (86) following the naive approach from (49) – (51), namely by treating explicitly the fluid traction on the boundary in the solid prediction step and enforcing the Dirichlet boundary condition strongly in the fluid prediction step. The corresponding results are presented in Figure 9, where we see that the numerical solution blowing up at time $t = 0.1$. The numerical instabilities are first concentrated on the left side of the domain where the total stress boundary condition holds and then propagate to the whole domain. Therefore, in this case, this strategy is not appropriate to impose (86).

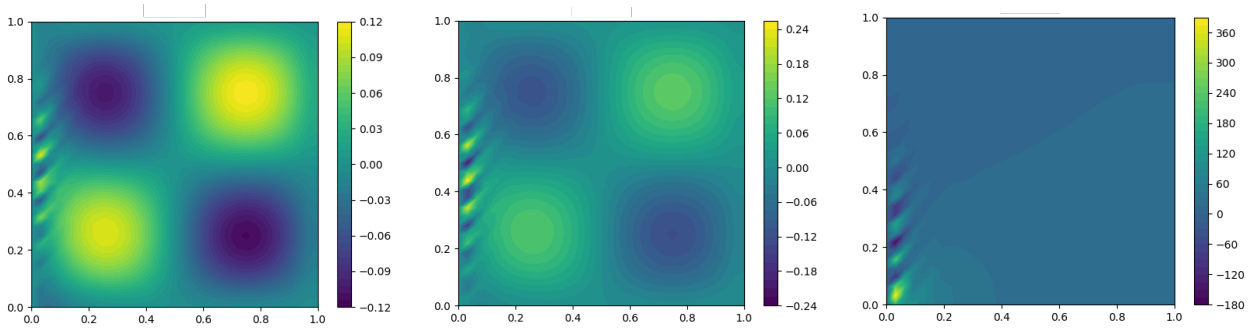

(a) $t = 0.12$ (b) $t = 0.13$ (c) $t = 0.2$

Figure 9: Pressure over time obtained by imposing the total stress boundary condition following (49) – (51).

However, the observed numerical unstabilities cannot be interpreted as an added-mass effect since they can be removed by simply reducing the time step or by augmenting the mesh size, see Figures 10a and 10b. This suggests that they are due to the explicit treatment of the fluid traction on the boundary and that stability could be proved under a CFL condition. As shown in Figure 10c, stability is also recovered by imposing (86) with the Robin-Robin coupling method proposed in Scheme 4. Hence, the advantage of the Robin-Robin coupling approach is that it offers stability irrespectively of time step and mesh size.

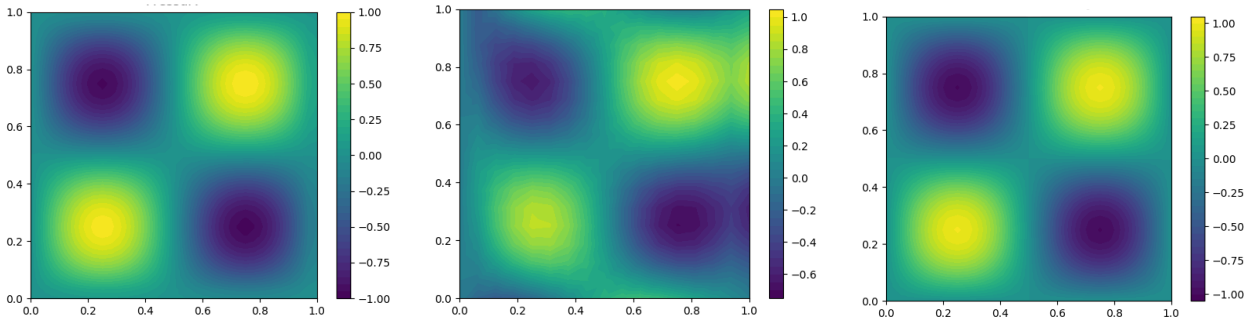

(a) $\Delta t = 0.25 \times 10^{-3}$ (b) Coarser mesh (c) Robin-Robin coupling

Figure 10: Different ways of recovering stability: changing Δt (a) or h (b) in the naive approach (49) – (51) or using Scheme 4 (c), here with the Robin coefficient $\alpha = 100$.

Finally, in Figure 11, we study the influence of the Robin coefficient α on the method accuracy. *A priori*, α must be chosen large in order to impose the equality of solid and fluid velocities on the interface. Moreover, in the discrete energy balance (58), the Robin-Robin coupling induces artificial energy on the boundary, scaling as $\Delta t(\alpha^{-1} + \alpha)$. Therefore, α must be chosen neither too large nor too small, as reported in [Burman et al., 2022a]. This heuristic reasoning is corroborated by Figure 11, which indicates to choose

α between 100 and 200 for the considered test case.

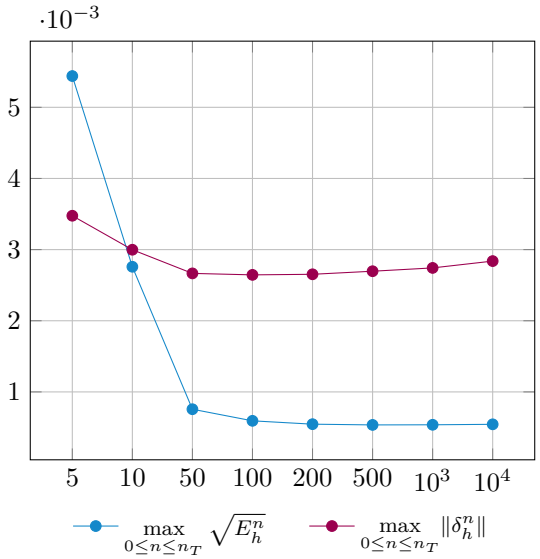

Figure 11: Energy and pressure errors with respect to the Robin coefficient α.

Conclusion

We have proposed and analyzed a projection scheme for a linearized incompressible poromechanics problem. Variants of the scheme were given depending on the treatment of the pressure and permeability terms in the prediction step, and on the boundary conditions considered. Stability analysis were performed for any these variants, in particular in the case of total stress boundary conditions in which a Robin-Robin coupling approach allowed us to obtain stability without the need of a CFL condition. For Dirichlet boundary conditions, a complete convergence analysis was provided and confirmed that the major difference between the incremental and non-incremental versions of the scheme lies in the time convergence rate of the pressure field. The various properties of the proposed schemes were illustrated numerically thanks to the manufactured solution method, and their computational efficiency was compared with that of the monolithic scheme from [Barré et al., 2023b] on a 3D case. Further perspectives include the use of these splitting schemes in other complex scenarios and a computation time comparison with respect to the alternate minimization approach from [Both et al., 2022]. Note that the present analysis may be generalized to the quasi-incompressible case, (see Remarks 2.3) and provide an asymptoticaly stable scheme in the skeleton incompressible limit. Moreover, the strategy shall be extended to the non-linear cases associated with large displacements and deformation configurations to propose efficient alternative to the time-scheme proposed in [Chapelle and Moireau, 2014; Burtschell et al., 2017].

References

Alnæs, M. S., Blechta, J., Hake, J., Johansson, A., Kehlet, B., Logg, A., Richardson, C., Ring, J., Rognes, M. E., and Wells, G. N. (2015). The FEniCS project version 1.5. *Archive of Numerical Software*, 3(100):9–23.

Astorino, M., Chouly, F., and Fernández, M. A. (2010). Robin based semi-implicit coupling in fluid-structure interaction: Stability analysis and numerics. *SIAM Journal on Scientific Computing*, 31(6):4041–4065.

Astorino, M. and Grandmont, C. (2010). Convergence analysis of a projection semi-implicit coupling scheme for fluid–structure interaction problems. *Numerische Mathematik*, 116(4):721–767.

Badia, S. and Codina, R. (2007). Convergence analysis of the FEM approximation of the first order projection method for incompressible flows with and without the inf-sup condition. *Numerische Mathematik*, 107(4):533–557.

Barnafi, N., Zunino, P., Dedè, L., and Quarteroni, A. (2021). Mathematical analysis and numerical approximation of a general linearized poro-hyperelastic model. *Computers & Mathematics with Applications*, 91:202–228.

Barnafi Wittwer, N. A., Gregorio, S. D., Dede', L., Zunino, P., Vergara, C., and Quarteroni, A. (2022). A Multiscale Poromechanics Model Integrating Myocardial Perfusion and the Epicardial Coronary Vessels. *SIAM Journal on Applied Mathematics*, 82(4):1167–1193.

Barré, M., Grandmont, C., and Moireau, P. (2023a). Analysis of a linearized poromechanics model for incompressible and nearly incompressible materials. *Evolution Equations and Control Theory*, 12(3):846–906.

Barré, M., Grandmont, C., and Moireau, P. (2023b). Numerical analysis of an incompressible soft material poromechanics model using T-coercivity. *Comptes Rendus. Mécanique*, 351(S1):1–36.

Basser, P. J. (1992). Interstitial pressure, volume, and flow during infusion into brain tissue. *Microvascular Research*, 44(2):143–165.

Berger, L., Bordas, R., Burrowes, K., Grau, V., Tavener, S., and Kay, D. (2016). A poroelastic model coupled to a fluid network with applications in lung modelling. *International Journal for Numerical Methods in Biomedical Engineering*, 32(1).

Biot, M. A. (1941). General theory of three-dimensional consolidation. *Journal of applied physics*, 12(2):155–164.

Biot, M. A. (1956). Theory of propagation of elastic Waves in a fluid-saturated porous solid. I. Low-frequency range. *The Journal of the Acoustical Society of America*, 28(2):168–178.

Both, J. W., Barnafi, N. A., Radu, F. A., Zunino, P., and Quarteroni, A. (2022). Iterative splitting schemes for a soft material poromechanics model. *Computer Methods in Applied Mechanics and Engineering*, page 29.

Both, J. W., Borregales, M., Nordbotten, J. M., Kumar, K., and Radu, F. A. (2017). Robust fixed stress splitting for Biot's equations in heterogeneous media. *Applied Mathematics Letters*, 68:101–108.

Both, J. W., Kumar, K., Nordbotten, J. M., and Radu, F. A. (2019a). Anderson accelerated fixed-stress splitting schemes for consolidation of unsaturated porous media. *Computers & Mathematics with Applications*, 77(6):1479–1502.

Both, J. W., Kumar, K., Nordbotten, J. M., and Radu, F. A. (2019b). The gradient flow structures of thermo-poro-visco-elastic processes in porous media.

Bukač, M., Yotov, I., and Zunino, P. (2015). An operator splitting approach for the interaction between a fluid and a multilayered poroelastic structure. *Numerical Methods for Partial Differential Equations*, 31(4):1054–1100.

Burman, E., Durst, R., Fernández, M., and Guzmán, J. (2021). Loosely coupled, non-iterative time-splitting scheme based on Robin-Robin coupling: Unified analysis for parabolic/parabolic and parabolic/hyperbolic problems.

Burman, E., Durst, R., Fernández, M. A., and Guzmán, J. (2022a). Fully discrete loosely coupled Robin-Robin scheme for incompressible fluid–structure interaction: Stability and error analysis. *Numerische Mathematik*, 151(4):807–840.

Burman, E., Durst, R., and Guzmán, J. (2022b). Stability and error analysis of a splitting method using Robin–Robin coupling applied to a fluid–structure interaction problem. *Numerical Methods for Partial Differential Equations*, 38(5):1396–1406.

Burman, E. and Fernández, M. A. (2009). Stabilization of explicit coupling in fluid–structure interaction involving fluid incompressibility. *Computer Methods in Applied Mechanics and Engineering*, 198(5-8):766–784.

Burman, E. and Fernández, M. A. (2014). Explicit strategies for incompressible fluid-structure interaction problems: Nitsche type mortaring versus Robin–Robin coupling. *International Journal for Numerical Methods in Engineering*, 97(10):739–758. Publisher: Wiley Online Library.

Burtschell, B., Chapelle, D., and Moireau, P. (2017). Effective and energy-preserving time discretization for a general nonlinear poromechanical formulation. *Computers & Structures*, 182:313–324.

Burtschell, B., Moireau, P., and Chapelle, D. (2019). Numerical analysis for an energy-stable total discretization of a poromechanics model with inf-sup stability. *Acta Mathematicae Applicatae Sinica, English Series*, 35(1):28–53.

Caiazzo, A., Fernández, M. A., Gerbeau, J.-F., and Martin, V. (2011). Projection schemes for fluid flows through a porous interface. *SIAM Journal on Scientific Computing*, 33(2):541–564.

Causin, P., Gerbeau, J., and Nobile, F. (2005). Added-mass effect in the design of partitioned algorithms for fluid–structure problems. *Computer Methods in Applied Mechanics and Engineering*, 194(42-44):4506–4527.

Causin, P., Guidoboni, G., Harris, A., Prada, D., Sacco, R., and Terragni, S. (2014). A poroelastic model for the perfusion of the lamina cribrosa in the optic nerve head. *Mathematical Biosciences*, 257:33–41.

Chabiniok, R., Burtschell, B., Chapelle, D., and Moireau, P. (2022). Dimensional reduction of a poromechanical cardiac model for myocardial perfusion studies. *Applications in Engineering Science*, 12:100121.

Chabiniok, R., Wang, V. Y., Hadjicharalambous, M., Asner, L., Lee, J., Sermesant, M., Kuhl, E., Young, A. A., Moireau, P., Nash, M. P., et al. (2016). Multiphysics and multiscale modelling, data–model fusion and integration of organ physiology in the clinic: ventricular cardiac mechanics. *Interface focus*, 6(2):20150083.

Chapelle, D., Gerbeau, J.-F., Sainte-Marie, J., and Vignon-Clementel, I. (2010). A poroelastic model valid in large strains with applications to perfusion in cardiac modeling. *Computational Mechanics*, 46(1):91–101.

Chapelle, D. and Moireau, P. (2014). General coupling of porous flows and hyperelastic formulations—from thermodynamics principles to energy balance and compatible time schemes. *European Journal of Mechanics-B/Fluids*, 46:82–96.

Chorin, A. J. (1969). On the convergence of discrete approximations to the navier-stokes equations. *Mathematics of computation*, 23(106):341–353.

Clarelli, F., Di Russo, C., Natalini, R., and Ribot, M. (2013). A fluid dynamics model of the growth of phototrophic biofilms. *Journal of Mathematical Biology*, 66(7):1387–1408.

Coussy, O. (2004). *Poromechanics*. John Wiley & Sons.

Di Gregorio, S., Fedele, M., Pontone, G., Corno, A. F., Zunino, P., Vergara, C., and Quarteroni, A. (2021). A computational model applied to myocardial perfusion in the human heart: From large coronaries to microvasculature. *Journal of Computational Physics*, 424:109836.

Fernández, M. A., Gerbeau, J.-F., and Grandmont, C. (2007). A projection semi-implicit scheme for the coupling of an elastic structure with an incompressible fluid. *International Journal for Numerical Methods in Engineering*, 69(4):794–821.

Gaspar, F. J., Gracia, J. L., Lisbona, F. J., and Oosterlee, C. W. (2008). Distributive smoothers in multigrid for problems with dominating grad–div operators. *Numerical linear algebra with applications*, 15(8):661–683.

Genet, M., Patte, C., Fetita, C., Brillet, P.-Y., and Chapelle, D. (2020). Personalized pulmonary poromechanics. *Computer Methods in Biomechanics and Biomedical Engineering*, 23(sup1):S119–S120.

Gerbeau, J.-F. and Vidrascu, M. (2003). A quasi-Newton algorithm based on a reduced model for fluid-structure interaction problems in blood flows. *ESAIM: Mathematical Modelling and Numerical Analysis*, 37(4):631–647.

Girault, V., Wheeler, M. F., Almani, T., and Dana, S. (2019). *A priori* error estimates for a discretized poro-elastic–elastic system solved by a fixed-stress algorithm. *Oil & Gas Science and Technology – Revue d'IFP Energies nouvelles*, 74:24.

Goda, K. (1979). A multistep technique with implicit difference schemes for calculating two- or three-dimensional cavity flows. *Journal of Computational Physics*, 30(1):76–95.

Guermond, J., Minev, P., and Shen, J. (2006). An overview of projection methods for incompressible flows. *Computer Methods in Applied Mechanics and Engineering*, 195(44-47):6011–6045.

Guermond, J.-L. (1996). Some implementations of projection methods for Navier-Stokes equations. *ESAIM: Mathematical Modelling and Numerical Analysis*, 30(5):637–667.

Guermond, J. L., Minev, P., and Shen, J. (2005). Error analysis of pressure-correction Schemes for the time-dependent Stokes Equations with open boundary conditions. *SIAM Journal on Numerical Analysis*, 43(1):239–258.

Guermond, J.-L. and Quartapelle, L. (1998). On stability and convergence of projection methods based on pressure Poisson equation. *International Journal for Numerical Methods in Fluids*, 26(9):1039–1053.

Guermond, J.-L. and Shen, J. (2003). Velocity-correction projection methods for incompressible flows. *SIAM Journal on Numerical Analysis*, 41(1):112–134.

Guidoboni, G., Glowinski, R., Cavallini, N., and Canic, S. (2009). Stable loosely-coupled-type algorithm for fluid–structure interaction in blood flow. *Journal of Computational Physics*, 228(18):6916–6937.

Guo, L., Vardakis, J. C., Lassila, T., Mitolo, M., Ravikumar, N., Chou, D., Lange, M., Sarrami-Foroushani, A., Tully, B. J., Taylor, Z. A., Varma, S., Venneri, A., Frangi, A. F., and Ventikos, Y. (2018). Subject-specific multi-poroelastic model for exploring the risk factors associated with the early stages of Alzheimer's disease. *Interface Focus*, 8(1):20170019.

Hansbo, P., Hermansson, J., and Svedberg, T. (2004). Nitsche's method combined with space–time finite elements for ALE fluid–structure interaction problems. *Computer Methods in Applied Mechanics and Engineering*, 193(39-41):4195–4206.

Heywood, J. G. and Rannacher, R. (1990). Finite-element approximation of the nonstationary navier–stokes problem. part iv: Error analysis for second-order time discretization. *SIAM Journal on Numerical Analysis*, 27(2):353–384.

Hong, Q., Kraus, J., Lymbery, M., and Wheeler, M. F. (2020). Parameter-robust convergence analysis of fixed-stress split iterative method for multiple-permeability poroelasticity systems. *Multiscale Modeling & Simulation*, 18(2):916–941.

Huang, M., Wu, S., and Zienkiewicz, O. C. (2001). Incompressible or nearly incompressible soil dynamic behaviour—a new staggered algorithm to circumvent restrictions of mixed formulation. *Soil Dynamics and Earthquake Engineering*, 21(2):169–179.

Huyghe, J. M., Arts, T., van Campen, D. H., and Reneman, R. S. (1992). Porous medium finite element model of the beating left ventricle. *American Journal of Physiology-Heart and Circulatory Physiology*, 262(4):H1256–H1267.

Kedarasetti, R. T., Drew, P. J., and Costanzo, F. (2022). Arterial vasodilation drives convective fluid flow in the brain: a poroelastic model. *Fluids and Barriers of the CNS*, 19(1):1–24.

Khaled, A.-R. and Vafai, K. (2003). The role of porous media in modeling flow and heat transfer in biological tissues. *International Journal of Heat and Mass Transfer*, 46(26):4989–5003.

Lee, J. J., Piersanti, E., Mardal, K.-A., and Rognes, M. E. (2019). A mixed finite element method for nearly incompressible multiple-network poroelasticity. *SIAM Journal on Scientific Computing*, 41(2):A722–A747.

Li, X., Han, X., and Pastor, M. (2003). An iterative stabilized fractional step algorithm for finite element analysis in saturated soil dynamics. *Computer Methods in Applied Mechanics and Engineering*, 192(35):3845–3859.

Logg, A., Mardal, K.-A., Wells, G. N., et al. (2012). *Automated Solution of Differential Equations by the Finite Element Method*. Springer.

Maria Denaro, F. (2003). On the application of the Helmholtz–Hodge decomposition in projection methods for incompressible flows with general boundary conditions. *International Journal for Numerical Methods in Fluids*, 43(1):43–69.

Markert, B. (2007). A constitutive approach to 3-d nonlinear fluid flow through finite deformable porous continua: With application to a high-porosity polyurethane foam. *Transport in Porous Media*, 70(3):427–450.

Markert, B., Heider, Y., and Ehlers, W. (2009). Comparison of monolithic and splitting solution schemes for dynamic porous media problems. *International Journal for Numerical Methods in Engineering*, 82:1341–1383.

Michler, C., Cookson, A. N., Chabiniok, R., Hyde, E., Lee, J., Sinclair, M., Sochi, T., Goyal, A., Vigueras, G., Nordsletten, D. A., and Smith, N. P. (2013). A computationally efficient framework for the simulation of cardiac perfusion using a multi-compartment Darcy porous-media flow model. *International Journal for Numerical Methods in Biomedical Engineering*, 29(2):217–232.

Mikelić, A. and Wheeler, M. F. (2013). Convergence of iterative coupling for coupled flow and geomechanics. *Computational Geosciences*, 17(3):455–461.

Nash, M. P. and Hunter, P. J. (2000). Computational mechanics of the heart. *Journal of elasticity and the physical science of solids*, 61(1):113–141.

Patte, C., Genet, M., and Chapelle, D. (2022). A quasi-static poromechanical model of the lungs. *Biomechanics and Modeling in Mechanobiology*, 21(2):527–551.

Polizzi, B., Bernard, O., and Ribot, M. (2017). A time-space model for the growth of microalgae biofilms for biofuel production. *Journal of Theoretical Biology*, 432:55–79.

Rannacher, R. (1992). On Chorin's projection method for the incompressible Navier-Stokes equations. In *The Navier-Stokes equations II — Theory and Numerical Methods*, pages 167–183. Springer.

Ruiz-Baier, R., Taffetani, M., Westermeyer, H. D., and Yotov, I. (2022). The Biot–Stokes coupling using total pressure: Formulation, analysis and application to interfacial flow in the eye. *Computer Methods in Applied Mechanics and Engineering*, page 30.

Settari, A. and Mourits, F. (1998). A coupled reservoir and geomechanical simulation system. *SPE Journal*, 3(3):219–226.

Shen, J. (1992). On Error Estimates of Projection Methods for Navier-Stokes Equations: First-Order Schemes. *SIAM Journal on Numerical Analysis*, 29(1):57–77. Publisher: Society for Industrial and Applied Mathematics.

Shen, J. (1995). On error estimates of the penalty method for unsteady Navier–Stokes equations. *SIAM Journal on Numerical Analysis*, 32(2):386–403.

Storvik, E., Both, J. W., Kumar, K., Nordbotten, J. M., and Radu, F. A. (2019). On the optimization of the fixed-stress splitting for Biot's equations. *International Journal for Numerical Methods in Engineering*, 120(2):179–194.

Temam, R. (1969). Sur l'approximation de la solution des équations de Navier-Stokes par la méthode des pas fractionnaires (i). *Archive for Rational Mechanics and Analysis*, 32:135–153.

Terzaghi, K. (1943). *Theoretical soil mechanics*. Wiley, New York.

Timmermans, L. J., Minev, P. D., and Van De Vosse, F. N. (1996). An approximate projection scheme for incompressible flow using spectral elements. *International journal for numerical methods in fluids*, 22(7):673–688.

Tully, B. and Ventikos, Y. (2011). Cerebral water transport using multiple-network poroelastic theory: application to normal pressure hydrocephalus. *Journal of Fluid Mechanics*, 667:188–215.

Van Kan, J. (1986). A second-order accurate pressure-correction scheme for viscous incompressible flow. *SIAM journal on scientific and statistical computing*, 7(3):870–891.

Vardakis, J. C., Chou, D., Tully, B. J., Hung, C. C., Lee, T. H., Tsui, P.-H., and Ventikos, Y. (2016). Investigating cerebral oedema using poroelasticity. *Medical Engineering & Physics*, 38(1):48–57.

Wall, W., Wiechert, L., Comerford, A., and Rausch, S. (2010). Towards a comprehensive computational model for the respiratory system. *International Journal for Numerical Methods in Biomedical Engineering*, 26(7):807–827.

Yang, M. and Taber, L. A. (1991). The possible role of poroelasticity in the apparent viscoelastic behavior of passive cardiac muscle. *Journal of biomechanics*, 24(7):587–597.

Zienkiewicz, O., Huang, M., Wu, J., and Wu, S. (1993). A new algorithm for the coupled soil-pore fluid problem. *Shock and Vibration*, 1(1):3–14.

Zienkiewicz, O. C., Paul, D. K., and Chan, A. H. C. (1988). Unconditionally stable staggered solution procedure for soil-pore fluid interaction problems. *International Journal for Numerical Methods in Engineering*, 26(5):1039–1055.